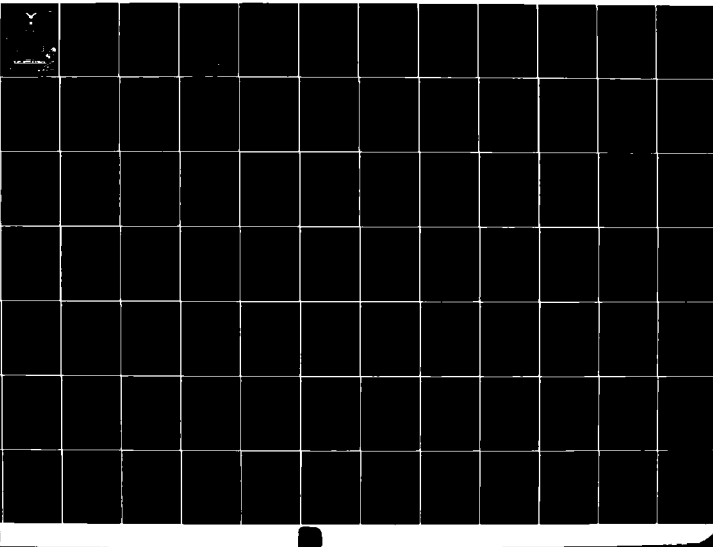
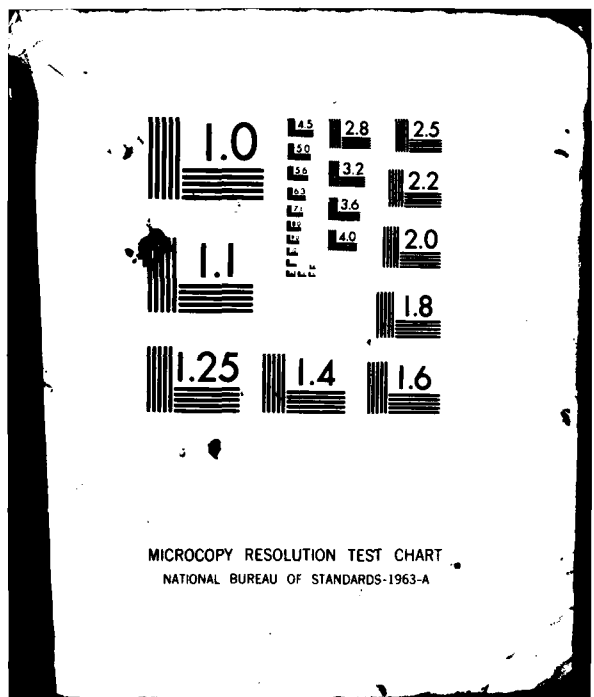


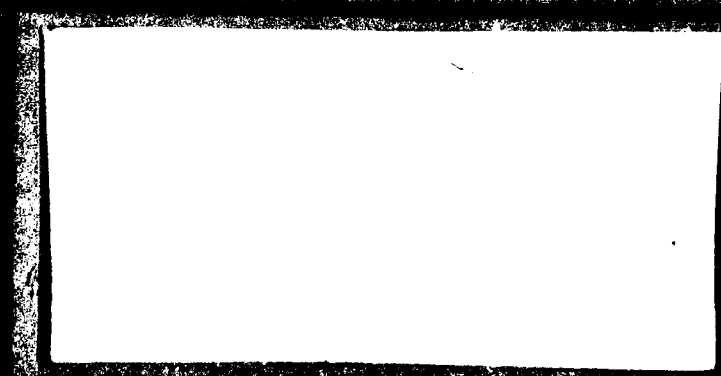
AD-A115 477 AIR FORCE INST OF TECH WRIGHT-PATTERSON AFB OH SCHOOL-ETC F/G 20/6
DESIGN CONSIDERATIONS FOR AN INCOHERENT FIBER OPTIC GYROSCOPE. (U)
DEC 81 R L ICE
UNCLASSIFIED AFIT/GE/EE/81D-29 NL

102
3
AFIT/GE/EE/81D-29





AD A115477



100

①

DESIGN CONSIDERATIONS FOR AN
INCOHERENT FIBER OPTIC GYROSCOPE

THESIS

AFIT/GE/EE/81D-29 RICHARD L. ICE
Captain USAF

DTIC
ELECTRONIC
JUN 14 1982
S H

Approved for public release; distribution unlimited.

AFIT/GE/EE/81D -29

DESIGN CONSIDERATIONS FOR AN
INCOHERENT FIBER OPTIC GYROSCOPE
THESIS

Presented to the Faculty of the School of Engineering
of the Air Force Institute of Technology

Air University

In Partial Fullfillment of the Requirements
of the Degree of Master of Science

by

Richard L. Ice

Capt USAF

Graduate Electrical Engineering

December 1981

Approved for public release; distribution unlimited.

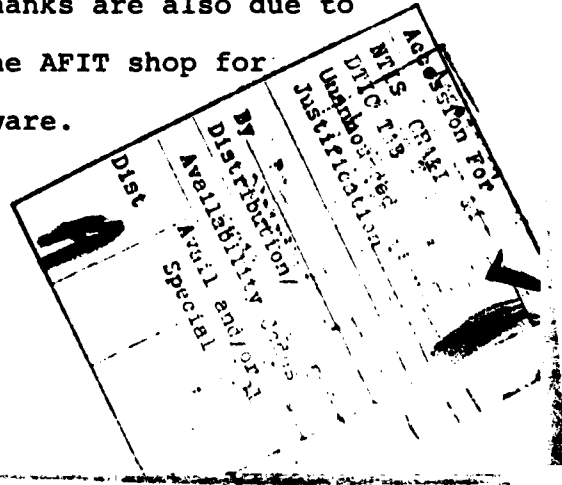
Preface

The purpose of this thesis is to demonstrate the possibility of operating a fiber optic gyroscope in the incoherent mode. The components necessary for the construction of such a gyro are characterized extensively and a knowledge of the problems associated with a particular set of these components is obtained.

The theory of optical fiber rotation sensors is discussed as it is applicable to the incoherent fiber gyro. Significant reductions in the polarization problems and light scattering in a single mode fiber are expected using the proposed methods. The knowledge gained about these components provides a baseline which should allow construction of such a gyro.

Included in the report is a review of optical rotation sensing and the types of sensors demonstrated and predicted to date. Appendices contain background information on the technology associated with fiber optic rotation sensing.

I would like to express my appreciation to my advisor, Major Salvatore Balsamo, for suggesting this topic and providing much background material. Thanks are also due to Mr. Carl Shortt and Mr. Ron Ruley of the AFIT shop for their fabrication of the required hardware.



Special thanks are due to Mrs. Vicki Francis for her most excellent typing of the report. Finally a special appreciation is due to my wife, Marian, for virtually raising our two children on her own during the course of this work. Without her help, there would be no thesis.

Table of Contents

Preface	ii
List of Figures	vi
List of Tables	viii
List of Symbols	ix
Abstract	xiv
I. Introduction	1
Rotation Sensing and the Fiber Gyro	1
Problems with the Fiber Gyro	2
Previous Approaches	3
Present Research Approach	6
II. Design of the Incoherent Fiber Gyro	9
Light Source	9
Two Proposed Gyro Configurations	13
Plan A	14
Plan B	16
III. Theory	19
Rotation Sensing	19
Sagnac Effect	19
Active Ring Laser Gyro	24
Passive Ring Laser Gyro	26
Fiber Optic Gyro	28
Fiber Resonator	29
Sensitivity Analysis	30
Interference Pattern	30
Component Losses	34
Noise	37
Scattering in Fibers	41
Coherence Length	45
IV. Experiment	49
Light Source Selection	49
LED's	50
Laser	62

Collimating and Beamsplitting Optics	68
Acousto-Optics	74
Fibers	79
V. Component Contributions to Error	88
Critical Components	88
Coupling Optics	90
Acousto-Optic Modulator	92
Summary of Major Error Sources	93
VI. Conclusions and Recommendations	94
Bibliography	98
Appendix A: Semiconductor Lasers	103
Appendix B: Fiber Optics	113
Appendix C: Polarization Optics of Fibers	115
Appendix D: Acousto-Optic Efficiency	119
Appendix E: Equipment and Experimental Set-up . . .	122
Appendix F: Detectors	127
Vita	131

List of Figures

<u>Figure</u>		<u>Page</u>
2.1	Sensitivity at Optimum Fiber Length	11
2.2	Plan A Gyro Configuration	15
2.3	Plan B Gyro Configuration	17
3.1	Sagnac Experiment	20
3.2	Simplified Ring	22
3.3	Active Ring Laser Gyro	25
3.4	PRLG Concept	27
3.5	Fiber Interferometer	29
3.6	Fiber Ring Resonator	30
3.7	Fiber Ring for Loss Analysis	35
4.1	LED Test Set-up	51
4.2	LED Intensity Comparison	53
4.3	Improved Set-up	54
4.4	Power Comparison of Two IR LED's	55
4.5	Intensity vs. Distance to Detector for Device #5	56
4.6	Intensity vs. Current, $d = 18$ cm, Device #5	57
4.7	Beam Shape from Device #4	58
4.8	Qualitative Beam Shape using Red LED	59
4.9	Aperturing of Beam	61
4.10	Laser Output Through Collimating Optics	64
4.11	Evolution of Laser Beam Polarization	66
4.12	Degree of Polarization	67
4.13	P_{lsr} Through Two Beamsplitters	72

<u>Figure</u>		<u>Page</u>
4.14	Beamsplitter Transmittance	73
4.15	SOP Through Beamsplitters	75
4.16	Effect of Beamsplitters on DP	76
4.17	Partially Constructed Gyro	81
4.18	Oth and 1st Order Modes Through a Multi-mode Fiber	84
4.19	A/O Efficiency	85
4.20	Oth Order Through Single Mode Fiber	86
5.1	A/O Error Sources	92
A.1(a)	Cross Section of Double Heterojunction Diode	105
A.1(b)	Characteristics of GaAs and InP Alloys	105
A.2(a)	Stripe Contact Heterojunction Laser	108
A.2(b)	Threshold Current Characteristics	108
E.1	Light Sources	123
E.2	Gyro Components	123
E.3	Laser Diode Mount	124
E.4	Experimental Set-up	124
F.1	Detector Amplifier	128

List of Tables

<u>Table</u>		<u>Page</u>
3.1	Summary of Scattering Data for a Typical Fiber	44
4.1	LED Types	52
5.1	Component Characteristics vs. Performance	89
F.1	Detector Gain	129

List of Symbols

A	Area enclosed by a ring
\AA	Angstrom (10^{-10} m)
A/O	Acousto-optic modulator
B	Detection bandwidth
BS	Beamsplitter
B_t	Backward trapping coefficient
c	Speed of light
d	Distance, diameter
dl	coherence length
DP	Degree of polarization
$\Delta\nu$	linewidth (Hz)
$\Delta\lambda$	Linewidth (meters)
E	Young's modulus
$E_{a/o}$	Acousto-optic efficiency
E_c	Coupling efficiency
E_{fc}	Fiber coupling efficiency
E_{ref}	Reflected efficiency
E_{tx}	Transmitted efficiency
e_o	Light induced voltage
F	Forward trapping coefficient
f_o	Fundamental light frequency
f_1	Frequency
FL	Focal length
g	Constant

h	Planck's constant
\tilde{h}	$h/2\pi$
HPBW	Half power beam width
I_{acoustic}	Acoustic beam intensity
I_{diff}	Diffracted light intensity
I_f	LED forward current
I_{incident}	Incident light intensity
I_L	Light intensity
ILD	Injection laser diode
I_{lsr}	Laser current
IR	Infrared
I_{th}	Threshold current
i_s	Light induced current
K	Additional phase shift
k	Integer
k_β	Birefringence
k_c	Circular birefringence
k_x, k_y	Propagation constants
L	Fiber length
LED	Light emitting diode
ℓ	Light/acoustic beam interaction width
m	Number of modes
MHz	Megahertz
M/O	Microscope objective
M_W	Figure of merit for an acousto-optic
N	Number of photons

NA	Numerical aperture
NDF	Neutral density filter
n	Index of refraction
n_{clad}	Cladding index of refraction
n_{core}	Core index of refraction
nm	Nanometer
P	Perimeter of a cavity
P_{lsr}	Laser power
P_0	Initial light power
P_T	Phase shift power
Q	Acousto-optic parameter
q	Electronic charge
R	Radius of a fiber coil
R_{BS}	Beam spread ratio
R_c	Radius of curvature of a bend
R_d	Responsivity of a photodiode
R_o	Fraction of light scattered
r	Radius of fiber (cross-section)
S	Signal current
S_N	Shot noise
S/N	Signal to noise ratio
SOP	State of polarization
T_0	Transmitted Light
t_{cw}	Time for clockwise travel
t_{ccw}	Time for counterclockwise travel
V_o	Output voltage of a detector amplifier

W	Width of an acoustic transducer
W_0	Fiber beam waist
W_1	Focused beam waist
α	Attenuation of a fiber
α_i	Power reflection coefficient
α_s	Scattering coefficient
α_{sr}	Rayleigh scattering coefficient
Δf	Frequency separation
Δf_c	Linewidth of a resonant cavity
Δs	minimum detectable signal
Δt	Time difference
Δz	Fringe shift distance
$\Delta \phi$	Phase shift
δ	Sagnac phase shift
δf	Modulation frequency
$\delta \theta_a$	Acoustic beam divergence
$\delta \theta_o$	Optic beam divergence
$\delta \Omega$	Rotation rate uncertainty
ϵ_x, ϵ_y	Electric permeability
η	Detector quantum efficiency
θ_β	Bragg angle
κ	$1/R_c$
Λ	Acoustic wavelength
λ	Wavelength
μ	Magnetic permeability
μ_m	Micron (10^{-6} m)
μ_w	Microwatt (10^{-9} watt)

v	Period
σ_z	Stress
τ	Integration time
τ_c	Coherence time
τ_o	Group delay
T	Twist rate
ψ	Non-reciprocal phase shift
Ω	Rotation
Ω_{min}	Minimum rotation rate
ω	Radian frequency

Abstract

The components required for the construction of an incoherent fiber optic gyroscope are tested. The instrument uses an incoherent light source such as an LED or diode laser operating below threshold. Five LED's and one laser diode were tested. An acousto-optic modulator is investigated as a signal processing element.

Equations are developed showing the effects of incoherence on the minimum expected rotation rate that can be observed. A review of optical rotation sensing in general, and the related technology is presented. The polarization properties of the source and fiber are discussed as they relate to gyro stability and minimum rotation rate.

Two possible signal processing techniques are presented which promise to further reduce minimum rotation rate and improve system stability.

The requirements on components for the fabrication of an inertial grade gyro are summarized along with a discussion of component contributions to gyro error.

I. Introduction

Rotation Sensing and the Fiber Gyro

The Sagnac ring interferometer has recently become a subject of much interest as an inertial rotation sensor. Advances in fiber optic technology have made the construction of very sensitive devices possible. Of particular interest to military applications is the fiber optic gyro because of its ruggedness, sensitivity, and potential small size and low cost. The fiber gyroscope also does not suffer from lock-in, null shift or mode pulling which plague the active ring laser gyro. These factors make the fiber gyro ideal as an inertial rotation sensor for tactical weapon systems (Ref 40). The required sensitivity and stability has not been achieved to date, however. Problems in overcoming system noises and polarization changes in the single mode fibers limit the performance of actual devices.

This thesis addresses some of the observed problems and offers potential solutions. A discussion of the basic Sagnac effect leads to various types of light rotation sensors which have been demonstrated and postulated to date. Previous approaches to overcoming the fiber gyro's limitations are presented. This is followed by a discussion of the present approach, the incoherent fiber gyro. The

theory of operation of such a device is presented and two designs are proposed. Results of experiments on gyro components are discussed along with possible solutions to the resulting potential problems.

Problems With the Fiber Gyro

Most of the problems in achieving the fiber gyros ultimate performance are related to the single mode optical fibers which are used almost exclusively. Noises due to various scattering mechanisms have limited the minimum rotation rate detectable. The fact that actual single mode fibers do not maintain states of polarization leads to undesired optical path length changes, which effect the device's accuracy and stability. This occurs because a single mode fiber actually supports two orthogonally polarized modes. Non-linear effects on the optical path such as pressure and twisting can allow mixing between the two states to occur. These effects cause a non-reciprocal phase shift of the signals which raises the minimum detectable rotation rate. Theoretical studies have indicated that the gyro should be able to measure rates as low as 10^{-3} degrees of rotation per hour (Ref 25, 47, 48). The above mentioned problems, however, presently limit performance to several orders of magnitude above the predicted limits.

In addition to factors related to the fiber, problems associated with the light source become important. For the fiber gyro to be compact and have low power requirements, a laser diode or other solid state source must be used. Errors due to changes in the laser diode's wavelength, output power and line width can occur. All of these effects contribute to the devices' bias drift rate as well as the minimum observable rotation rate.

A third area of difficulty in the ring interferometer has been the discrete optical components used. Because the instrument is capable of measuring phase changes which are a function of the wavelength of light, extreme mechanical stability is required. Most researchers conclude that this problem is most likely to be solved only through the use of integrated optics, and the design of a solid block configuration.

Previous Approaches

Most efforts to date have been in the areas of polarization control and the development of signal processing techniques which overcome the error sources. Signal processing techniques have included: modulation of the laser source (Ref 27), phase sensitive detection, operating at "quadrature" (or with a 90° phase bias) (Ref 43), and frequency and phase modulation schemes (Ref 4, 9, 12, 17, 25, 32, 41, 43, 53). Polarization control consists of placing polarizers at each

end of the fiber (to ensure one state of polarization in the system) (Ref 36), and complex active polarization stabilization (Ref 4, 43). The next section discusses polarization control techniques. This is followed by a discussion of signal processing techniques which help overcome the noise problems.

Approaches in Polarization Control

The simplest method of at least reducing the polarization problem is to place polarizers at each end of the fiber. For the problem to be completely eliminated, however, the polarizers must be perfect, a condition which cannot be met in practice. A recent example demonstrated even for a modest drift goal of 0.01 deg/sec, that demands on polarizer quality are extremely stringent (Ref 20). Polarization control must therefore be achieved actively. This is done by inducing a birefringence artificially to the fiber which automatically cancels any polarization degradation. (See Appendix C for a discussion on birefringence and other properties of fibers). This control is applied by twisting or stretching the fiber (Ref 47), or squeezing it mechanically (Ref 19). It may also be possible to employ magneto optic techniques (Ref 38). At least one attempt has been made to introduce a large birefringence by coiling the fiber under tension on a cylinder (Ref 34). All of these methods introduce additional components which increase size and complexity or add to production problems. The best performance noted to date has

been achieved by a combination of active polarization control and complex signal processing schemes (Ref 7, 43).

One simple approach is to abandon any attempt to maintain polarization and to employ random polarization states. If the fiber propagates an infinite number of states of polarization any effects of the fiber on polarization are equally distributed and a constant scale factor is maintained. A recent example (Ref 6) uses a wide line width light source and a depolarizer (Ref 5) to achieve random polarization. Even with a comparatively simple set-up, no change in scale factor is observed, and a bias drift of 0.0013 degrees per second is achieved.

Signal Processing

As is discussed in Chapter III, maximum sensitivity at low rotation rates is achieved when the gyro is operated with an induced 90° phase shift between the counter-rotating beams (Ref 49). Most signal processing schemes studied so far deal with ways of achieving this operation. Other processing techniques are usually concerned with modulating the signal, the so-called a/c detection. A third method is to employ some sort of active feedback system to null out some characteristic of the signal (frequency or phase) (Ref 9, 43, 53). Some configurations have also employed

dual detection to help cancel out any correlated noises in the detector outputs (Ref 25). Recently, researchers have turned to integrated optics and laser diodes as possible solutions to the noise problem.

Laser Diodes and Integrated Optics

The noises due to backscattering in the fiber can be drastically reduced by the use of a wider linewidth source which has a shorter coherence length (Ref 6), such as an LED or a laser diode. This short coherence length suppresses most of the undesired interferences in the reflected waves. A recent study (Ref 53) emphasized the need for implementing the gyro in a solid-block. The laser diode and the emerging integrated optics technology seem to be the most promising candidates for achieving the theoretical sensitivity limit.

Present Research Approach

This thesis presents a possible alternative to the problems which have limited the fiber gyro's performance. The specific areas addressed are the polarization and backscatter noises. The use of an incoherent source which emits randomly polarized light is proposed. This is different from (Ref 6) a recent attempt, in that the random polarization is a characteristic of the source and not introduced by a depolarizing device. A light emitting diode (LED) is a good candidate for such a source and several are investigated for their applicability. It is discovered that an injection laser diode can in some cases be operated below

lasing threshold and thus have the desired incoherence and random polarization. The lasing threshold of such a device should be sufficiently high to allow a significant amount of light power output due to spontaneous emission. A diode having this characteristic ($I_{th} > 150$ mA) is extensively characterized during the experiment. This device is found to possess completely random polarization below about 120 mA with an available coupled power of about 0.1 mW.

The short coherence length (Ref 35, 41, 49) of the injection laser also make it ideal for reducing the noises resulting from scattering mechanisms in the fiber. The wide linewidth of an LED also make it attractive, but, as discussed later, the source size of an LED causes beam collimation and control problems.

Two signal extraction schemes are presented and the experimental data in Section IV is a result of an attempt to build the first configuration. Plan A is an open loop, modulated system which employs one acousto-optic device to induce a frequency difference between the two beams propagating in the fiber coil. This, in effect, adds an artificial phase bias in addition to any Sagnac phase shift. This additional phase can be useful for improving the sensitivity of the instrument at low rotation rates, as is discussed in Chapter III. The induced phase difference is modulated to help alleviate the need for high stability in the bias signal.

Plan B consists of a closed loop system employing two acousto-optic frequency shifters. Both beams are shifted in frequency by the modulators for zero rotation, the light travelling in both directions is of the same frequency. An additional frequency can be added to one of the beams to null out phase shifts due to rotation rates. This additional frequency can then be used as a direct measure of rotation rate.

Both plans can incorporate a dual detection scheme to further reduce any noises introduced in the detection process.

Chapter II presents a complete discussion on coherence and polarization aspects of the gyro along with details of the two modulation schemes. Chapter III is a review of the theory associated with optical rotation sensing. A detailed analysis of the sensitivity of the fiber gyro is included. Chapter IV reports on the results obtained in testing of the components needed to implement the incoherent fiber gyro and how these components are tested.

A recent extensive analysis of component contribution to gyro errors is summarized in Chapter V (Ref 53). The results of this analysis as related to the present gyro design are discussed. Conclusions and recommendations are presented in Chapter VI. A number of appendices are included to further explain the technology associated with fiber optic rotation sensing.

II. Design of the Incoherent Fiber Gyro

Light Source

The wavelength and spectral characteristics (linewidth) of the light source are of importance in determining the sensitivity of the gyro. It is well known that the attenuation of an optical fiber is dependent on the wavelength of the light passing through it (Ref 8). In general, the attenuation decreases with increasing wavelength. As the development in Chapter III shows, the shot noise limited rotation rate is also a function of wavelength. The limiting sensitivity of a simple gyro can be expressed in an equation relating rotation rate and wavelength (Ref 49).

$$\Omega_M = \frac{\lambda c}{4\pi RL} [2\hbar\omega B/\eta P_0]^{\frac{1}{2}} 10^{\alpha L/20} \quad (2-1)$$

Where:

P_0 = starting power

α = fiber attenuation

L = length of fiber

R = radius of coil

c = speed of light

λ = wavelength

η = detector quantum efficiency

B = detection bandwidth

\bar{h} = $h/2$ h = plank's Const. = 6.626×10^{-34} joule-sec

ω = frequency in radians.

From this relation, the optimum fiber length can also be found by maximizing the dependency of Ω_M on L. Because the equation contains both λ and α , which itself is dependent on wavelength, the two parameters offset for effect on minimum sensitivity. As the wavelength increases the minimum sensitivity increases, but the fiber also has less attenuation at higher wavelengths and the minimum sensitivity for a given power level decreases. Figure 2-1 which is adapted from (Ref 49) shows the sensitivity of the gyro as a function of wavelength and power. Each curve is generated using the optimum calculated length. For fiber lengths considerably less than optimum (< 1 Km for $\lambda = .84 \mu\text{m}$), the sensitivity is less dependent on wavelength.

Coherence Length

The coherence length (d_1) is an important parameter in the operation of any interferometer. It has a direct impact on the ability of two light waves to interfere and produce high contrast fringe patterns. In a normal interferometer it places restrictions on the amount of optical path difference that can exist between the two legs of an

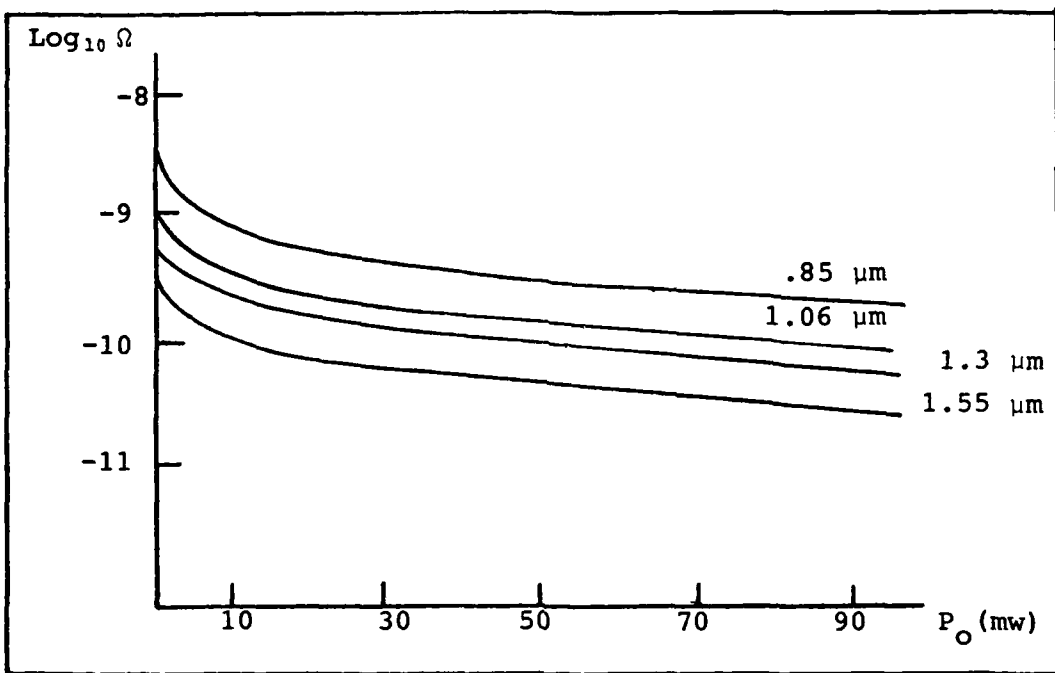


Figure 2.1 Sensitivity at Optimum Fiber Length

interferometer. For the fiber ring interferometer, the light waves occupy the same waveguide and, by definition, traverse the same path when the instrument is at rest. This fact theoretically allows the use of very short coherence length sources, as has been demonstrated (Ref 6, 7, 41).

The coherence length (d_1) can be related to the linewidth through the following expression (Ref 49):

$$d_1 = \frac{c}{dv}$$

where dv = linewidth (in Hz)

or:

$$dl = \frac{\lambda^2}{d\lambda}$$

where $d\lambda$ = linewidth (in meters).

For example, a diode emitting at $\lambda = 0.84 \mu m$ with a single mode of width $d\lambda = 1\text{Å}$, has a coherence length of:

$$dl = \frac{(0.84 \times 10^{-6})^2}{(1 \times 10^{-10})} = .0071 \text{ m}$$

A larger linewidth gives a correspondingly shorter coherence length. An extremely wide source such as an LED leads to extremely short coherence lengths. The use of a "superluminescent diode" has been reported (Ref 6) which has a coherence length of $20 \mu m$.

The coherence length can be used to an advantage in reducing the noises from backscattering in the fiber. A dramatic demonstration of this was presented in (Ref 7). Two fiber gyroscopes were built, one used a HeNe laser at $.63 \mu m$ and the second employed a GaAs laser centered at $.854 \mu m$. The scattering contribution to the noise was reduced by an order of magnitude by use of the laser diode.

It is known that a laser diode is essentially a multimode device at and below lasing threshold (I_{th}). The effect of multimode operation on coherence length has been

investigated (Ref 35). The coherence of a heterojunction GaAlAs laser is directly measured using a heterodyne detection scheme instead of a Fabry-Perot interferometer. It is noted that the laser modes observed peak around .89 μm with longitudinal mode spacings of about 2.7 \AA . The measured coherence length is found to increase as a function of drive current, which corresponds to the laser moving closer to essentially single mode operation. It is concluded that not only wide linewidth decreases coherence length. The "apparent" coherence length can be reduced by the presence of multiple modes.

Since in some cases the laser may be operated in a pulsed mode, the effect on modes of rapid turn-on has become important. The laser diode emission wavelength can also change as a function of thermal transients due to turn-on (Ref 28). Since pulsed operation is not required for the noncoherent gyro this effect is not discussed in this thesis.

Two Proposed Gyro Configurations

This section presents two modes of operation of the gyro. Both consist of signal processing techniques which employ the principle of acousto-optic deflection of light. When a light beam enters an acousto-optic crystal which is properly adjusted at the Bragg angle, it is not only deflected at this angle, but also shifted in frequency. The sign of the angle determines whether the light frequency is shifted up or down. A discussion of acousto-optic modulators is included

included in Appendix D. The interaction of the light and sound waves is an important aspect of the gyro operation as is discussed in the experiment. Appendix D also discusses these interactions as they related to the operation of this particular gyro.

Plan A

The first scheme discussed employs one acousto-optic frequency shifter in an open loop detection process. Figure 2.2 shows the basic idea. Light from a suitable source (LED or ILD) is collimated by a lens and passes through two beam-splitters. The second beam-splitter divides the light into two paths for circulation through the fiber coil. The clockwise (cw) beam is immediately coupled into the fiber via a microscope objective. The counter clockwise (ccw) beam first passes through the acousto-optic cell where it is shifted by frequency f_1 . For the case shown here, the A/O is adjusted so that f_1 is added to the basic light frequency (f_o).

When the cw beam (at f_o) passes through the A/O after traversing the coil, it too is shifted to $f_o + f_1$. The two beams then recombine at BS2 and interfere. Note that they are now at the same frequency ($f_o + f_1$) but a phase difference now exists. The phase shift between the two

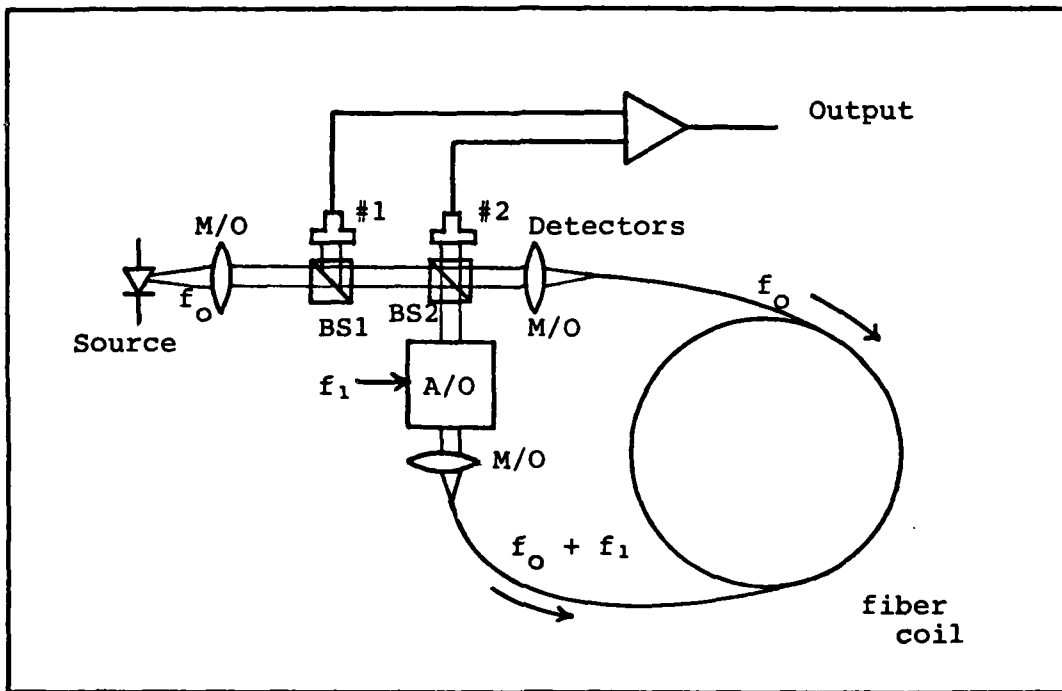


Figure 2.2 Plan A Gyro Configuration

beams is caused by the fact that in the coil, the beams propagate at different frequencies. When the interferometer is at rest in inertial space, this phase shift is determined only by f_1 . Upon rotation, an additional phase shift is induced by the Sagnac effect. As seen in Chapter III, the sensitivity of the detection process is dependent on the amount of the fixed phase bias for low rotation rates. Maximum sensitivity is obtained at low rates by the introduction of a $\frac{\pi}{2}$ phase bias between the counter rotating beams. This operation "in quadrature" (Ref 17, 25, 32), becomes important when an open loop detection scheme such as this is used.

The two beams are split after combining by BS2. One beam travels onto detector #2 and the second is reflected by BS1 onto detector #1. The signals falling on the two detectors, since they undergo different numbers and orders of reflections, are out of phase. It is assumed here that this difference is 180° . The output of both detectors can then be combined to help reject any common mode noises associated with the detection process.

The frequency f_1 can also be modulated about its center. This FM technique can reduce the need for a stable phase bias by allowing an A/C detection process to occur. Variations in the induced bias which cause the operating point to move around can be averaged out.

An attempt to implement this plan is the subject of Chapter IV, the experiment. The components required for this configuration are extensively characterized. Light source power limitations coupled with less than ideal component efficiencies prevents the demonstration of a working gyro, however.

Plan B

The second proposed configuration employs active feed-back to null out any frequency shifts due to rotation rates. This technique requires two acousto-optic frequency shifters.

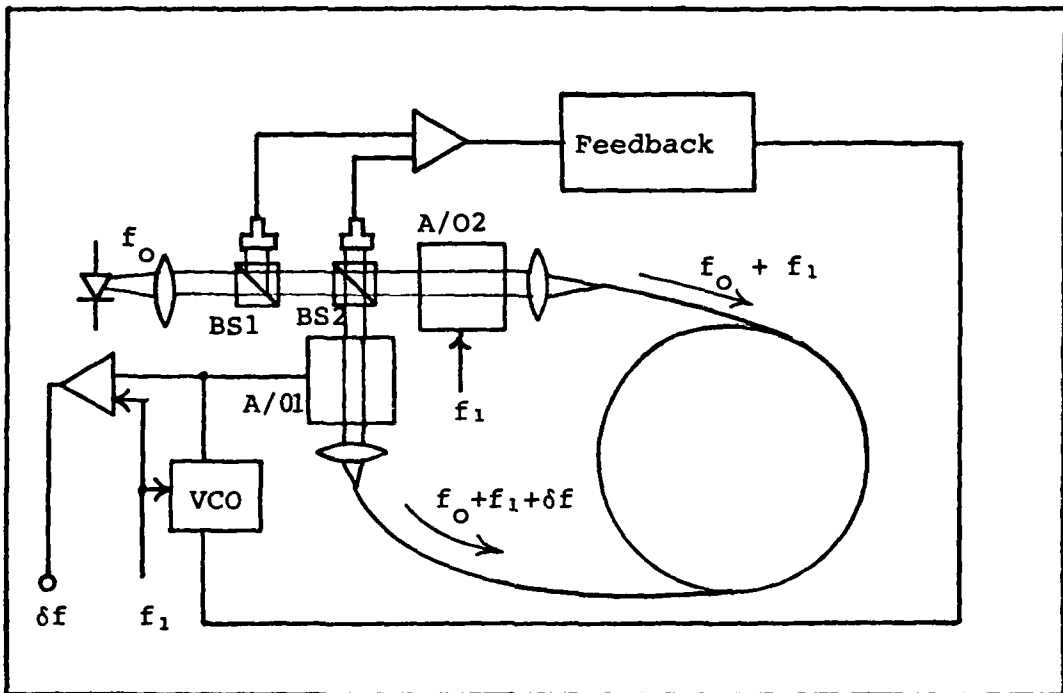


Figure 2.3 Plan B Gyro Configuration

This approach is similar to the one used for the passive ring laser gyro (Ref 14) and for a fiber interferometer (Ref 13). Figure 2.3 shows the basic idea. Both acousto-optics are driven at a stable reference frequency (f_1). Acousto-optic #1 has an additional frequency component (δf) which can offset the rotation induced Sagnac phase shift. When the device is at rest, δf is zero. δf is derived through a feedback network which attempts to null out any output changes from the detectors caused by fringe shifts. This induced difference δf can then be used as a direct readout of rotation rate. This design is similar to the

phase-nulling gyro (Ref 9) which employs only one A/O device but does use active feedback. Note that this scheme does not require operation in quadrature to achieve linear sensitivity at low rates. The fact that δf should vary directly with the Sagnac induced phase shift yields a linear output at any rate of rotation. The sensitivity at this configuration depends to some extent on the characteristics of the feedback network and the stability of the VCO.

III. Theory

All optical rotation sensors are based on the Sagnac effect (Ref 30), which in turn has its basis in relativity theory. This chapter discusses the Sagnac effect and the four types of rotation sensors which have been demonstrated or proposed to date. A detailed analysis of the sensitivity of a simple fiber ring interferometer is presented. The effect of component losses on the theoretical sensitivity is also included. This section concludes with a brief summary of the scattering and light polarization problems that occur in real optic fiber.

Rotation Sensing

Sagnac Effect. The first demonstration of optical rotation was achieved by Sagnac in 1913. The entire experiment including light source and fringe detector is placed on a turntable and rotated at two revolutions per second. Figure 3.1 shows a simplified schematic of the interferometer. Light from the source (LS) is directed to the beamsplitter, (in Sagnac's apparatus it was a half silvered mirror). The light is split and is propagated in both directions around the enclosed path by the three corner mirrors m_1 , m_2 and m_3 . The two beams recombine at BS and form a fringe pattern

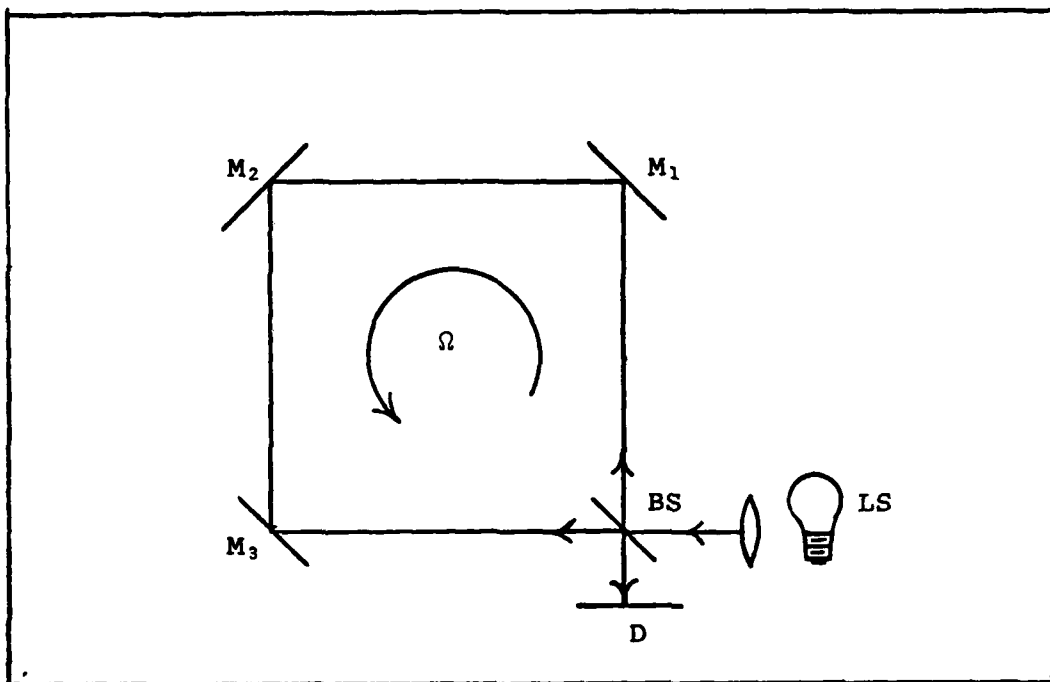


Figure 3.1 Sagnac Experiment

which is observed at D. The observation plane D can either be a screen, or a photodetector. Sagnac observed the fringes visually.

When the apparatus is set in motion at a rotation rate, Ω , the stationary fringe pattern shifts. The amount of the fringe shift is given by:

$$\Delta z = \frac{4\Omega A}{\lambda c} \quad (3-1)$$

where A is the area enclosed by the light path, and λ is the light wavelength.

This result can be obtained by use of the principle of space-time covariance and Lorentz transformations, but this approach is beyond the scope of this report. For this thesis, a simpler kinematic approach is taken. Figure 3.2 shows a circular interferometer with two signals propagating in opposite directions (Ref 49). The ring is assumed to be rotating in the clockwise direction at a rate Ω . The time for the clockwise beam to go from the point of injection to the same physical point on the ring is:

$$t_{cw} = \frac{2\pi R + \Delta S}{c} \quad (3-2)$$

Since the ring is shifted by ΔS due to rotation:

$$\Delta S = t_{cw} \Omega R \quad (3-3)$$

then substituting ΔS into (Eq 3-2) yields:

$$t_{cw} = \frac{2\pi R + t_{cw} \Omega R}{c}$$

$$t_{cw} = \frac{2\pi R}{c - \Omega R} \quad (3-4)$$

Likewise the time for the beam to travel in the ccw direction is:

$$t_{ccw} = \frac{2\pi R - \Delta S'}{c}$$

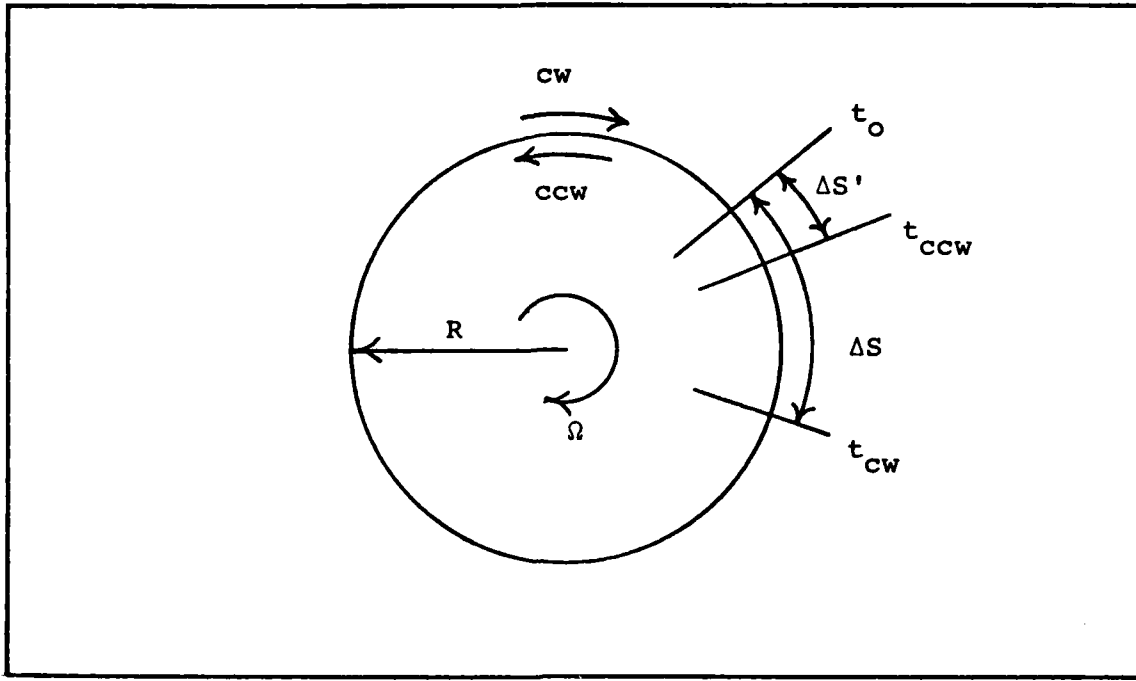


Figure 3.2 Simplified Ring

Since the path is shortened by $\Delta S'$, then:

$$t_{CCW} = \frac{2\pi R}{c + \Omega R} \quad (3-5)$$

The time difference between the two paths is:

$$\Delta t = t_{CW} - t_{CCW}$$

$$\begin{aligned} \Delta t &= 2\pi R \left(\frac{1}{c - \Omega R} - \frac{1}{c + \Omega R} \right) \\ &= 2\pi R \frac{2\Omega R}{c^2 - \Omega^2 R^2} \end{aligned}$$

For rotations rates of concern ($\Omega^2 R^2 < CC^2$), this equation reduces to:

$$\Delta t = \frac{4\pi R^2}{c^2} = \frac{4A\Omega}{c^2} \quad (3-6)$$

where A is the area enclosed by the ring.

The fringe pattern shifts due to the phase shift between the two waves caused by Δt . The shift

$$\Delta Z = \Delta t v = \Delta t c / \lambda$$

where v is the period.

Substituting Δt into the above relation yields:

$$\Delta Z = \frac{4\Omega A}{\lambda c}$$

which is the expression given by (Eq 3-1).

The difference in the phase relationships of the two waves is given by

$$\Delta\phi = 2\pi\Delta Z = \frac{8\pi\Omega A}{\lambda c} \quad (3-7)$$

This phase shift produces a change in the intensity of the fringe pattern and this intensity change is the quantity detected for measuring rotation rates.

Active Ring Laser Gyro. The use of the basic Sagnac interferometer is limited due to its lack of sensitivity, since the path difference is much less than a wavelength in most cases. The Active Laser Gyro (Ref 3) was the first rotation sensor to demonstrate enough sensitivity for use as an inertial grade rotation sensor. In the Active Ring Laser Gyro (ARLG), the laser gain medium placed in the cavity as shown in Figure 3.3. The improvement in sensitivity is due to the fact that the lasing frequency is now dependent on the cavity length. When the gyro is rotated, each of the two opposite traveling waves sees a slightly different cavity length. This change in cavity length gives a frequency separation between the two waves of:

$$\Delta f = \frac{4\pi\Omega}{L\lambda} \quad (3-8)$$

If the two beams are brought out of the cavity, as shown in Figure 3.3, and allowed to interfere, the frequency difference results in motions of the fringes. This beat frequency can be measured even though it is typically only $\sim 10^{-14}$ of the light frequency. An example of 13.2 cm per side, a rotation of 20 deg/hr and the He Ne wavelength of .633 μ m yields a beat frequency of 5.9 Hz.

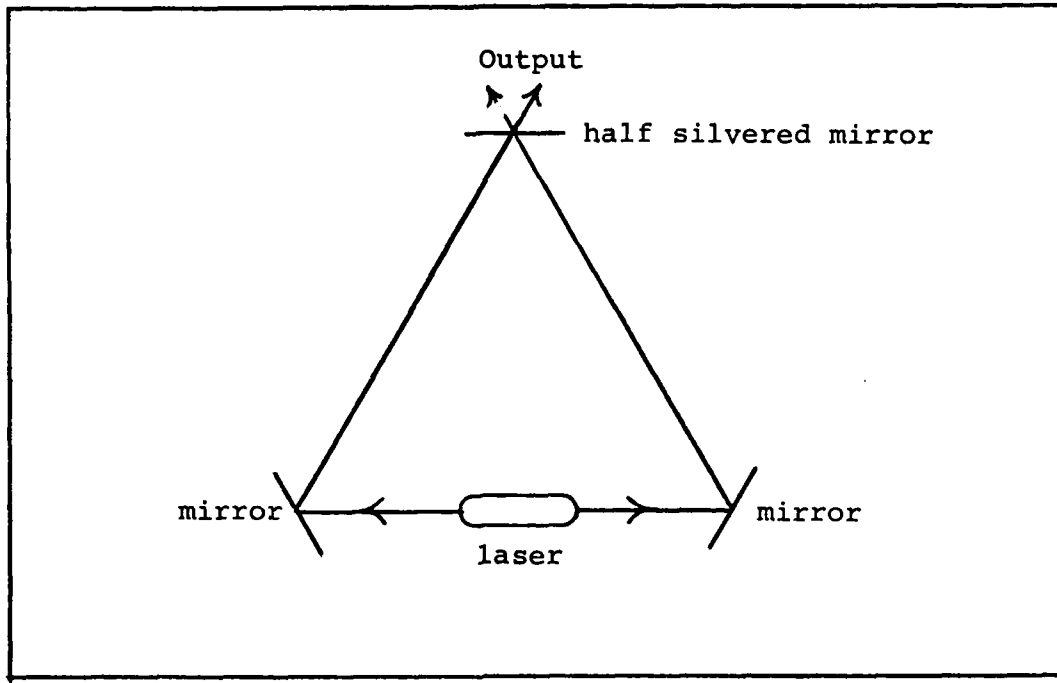


Figure 3.3 Active Ring Laser Gyro

The ARLG suffers from three major sources of error; null shift, lock-in and mode pulling. Null shift occurs when differences in the optical path length between the two directions occur. This can be caused by the properties of the lasing medium, or such things as gas flow in the cavity. Lock-in is the result of backscattering of the light waves at the various optical interfaces. This effect causes the beams to lock together in frequency for low rotation rates. At higher rates, the induced frequency change is large enough to overcome lock-in. Mode pulling is caused by dispersion effects of any material in the

cavity (such as the gas lasing medium). It results in instabilities which change the gyro's output scale factor.

Null shift and mode pulling can be reduced somewhat by careful design. Lock-in requires that an artificial frequency shift be introduced between the two waves. This is done by introducing a non-reciprocal phase shift (Faraday cell), by mechanically dithering the gyro to keep it above lock-in, or, more recently, by the use of magnetic mirrors.

The Passive Ring Laser Gyro (PRLG). If the lasing medium is removed from the cavity, most of the problems of the ARLG are eliminated. The laser may be placed outside a resonant cavity and its light beam used to measure path length difference in the two cavity directions. This was demonstrated first by Ezekiel and Balsamo (Ref 14). Their scheme, which is reproduced in Figure 3.4, uses two light frequencies in the cavity, created by employing acousto-optic modulators. An active feedback scheme is used to null out frequency differences due to rotation rate. The mechanical stability of the cavity is controlled by a mirror attached to a piezoelectric transducer which controls cavity length.

The frequency differences of the cavity (cw to ccw) is given by:

$$\Delta f = \frac{4A\Omega}{\lambda P} \quad (3-9)$$

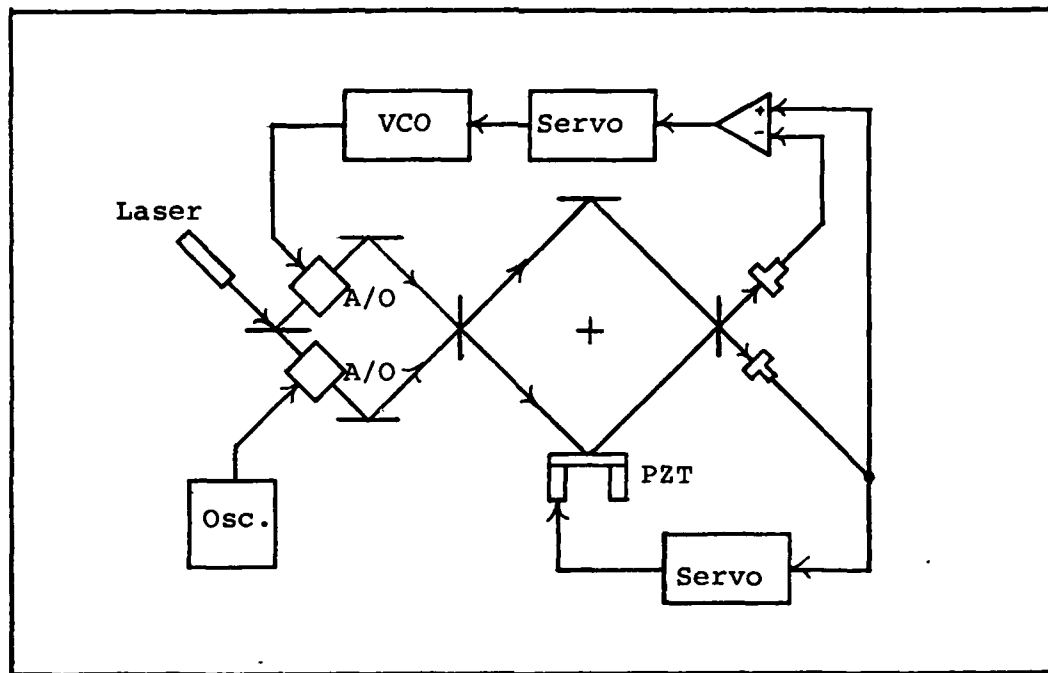


Figure 3.4 PRLG Concept

Where A is the area and P is the perimeter of the cavity. Assuming shot noise limited detection they predicted a rotation rate uncertainty of $\delta\Omega$ given by:

$$\delta\Omega = \frac{10^5 \lambda P \Delta f_c}{4A\sqrt{N\tau}} \text{ (deg/hr)} \quad (3-10)$$

Where

Δf_c = linewidth of cavity

N = number of photons transmitted at resonance

τ = integration time

Fiber Optic Gyro. The fiber ring interferometer was first demonstrated by Vali and Shorthill in 1976 (Ref 47 48). Their basic configuration is shown in Figure 3.5. Light from a HeNe laser was focused onto the two ends of 10 m single mode fiber. Fringes were observed easily but no rotation data was presented. The fringe shift expected was:

$$\Delta Z = \frac{4NA\Omega}{\lambda c} \quad (3-11)$$

Where N is the number of turns of the fiber. In a later section, a calculation of optimum fiber length is discussed. Vali and Shorthill predicted that the minimum detectable fringe shift would be

$$\Delta Z_m = \frac{\sqrt{B}}{2\pi} \frac{hv}{\eta P}^{1/2} \quad (3-12)$$

where P is the beam power out of the interferometer, B is the detector bandwidth, and η is the quantum efficiency.

$$P = P_0 10^{-\alpha L} \quad (3-13)$$

and α is the attenuation of the fiber and L its length. Using a 3 mW HeNe laser as a source and a 2 dB/Km loss fiber of L = 4.3 Km, and R = 15 cm, a minimum detectable rotation rate of 1.5×10^{-9} rad/sec is predicted.

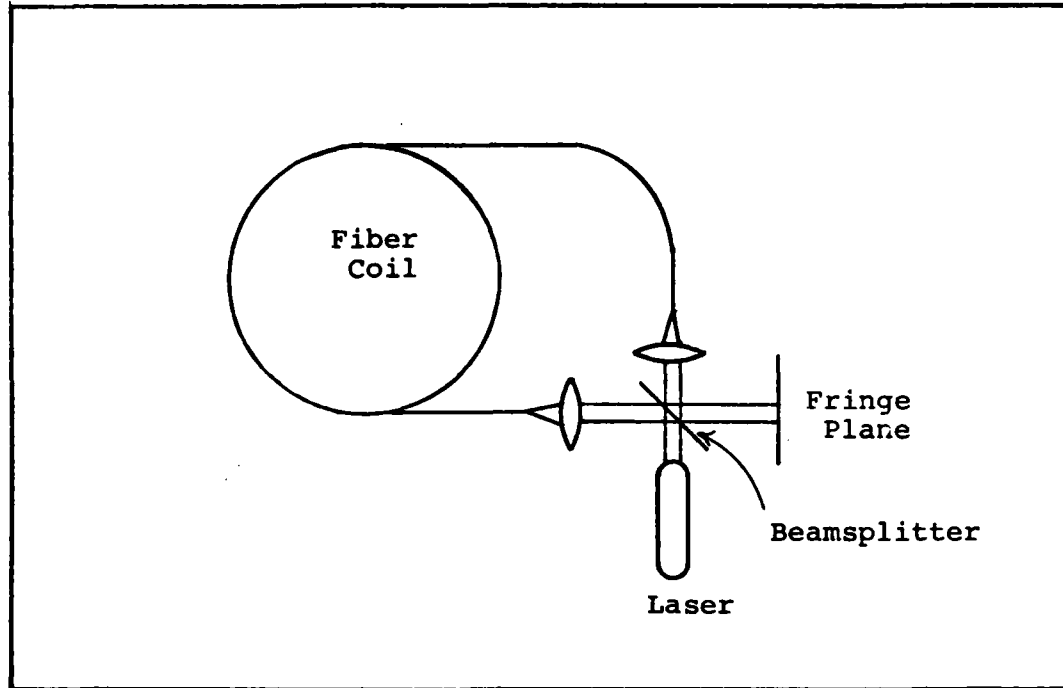


Figure 3.5 Fiber Interferometer

Fiber Resonator. A fourth type of Sagnac instrument has been proposed (Ref 14) in which the mirror cavity of the PRLG is replaced by a coil of fiber. The fiber forms a closed loop and acts as a resonator. Figure 3.6 shows the idea as represented by Shupe (Ref 37).

Light from the laser is frequency shifted by the two acousto-optic modulators and coupled into the coil by an evanescent type coupler. The signal processing is the same as for the PRLG. Shupe gave the equations for optimizing the fiber length and theoretically predicts a sensitivity equal to that of the fiber ring interferometer. He lists

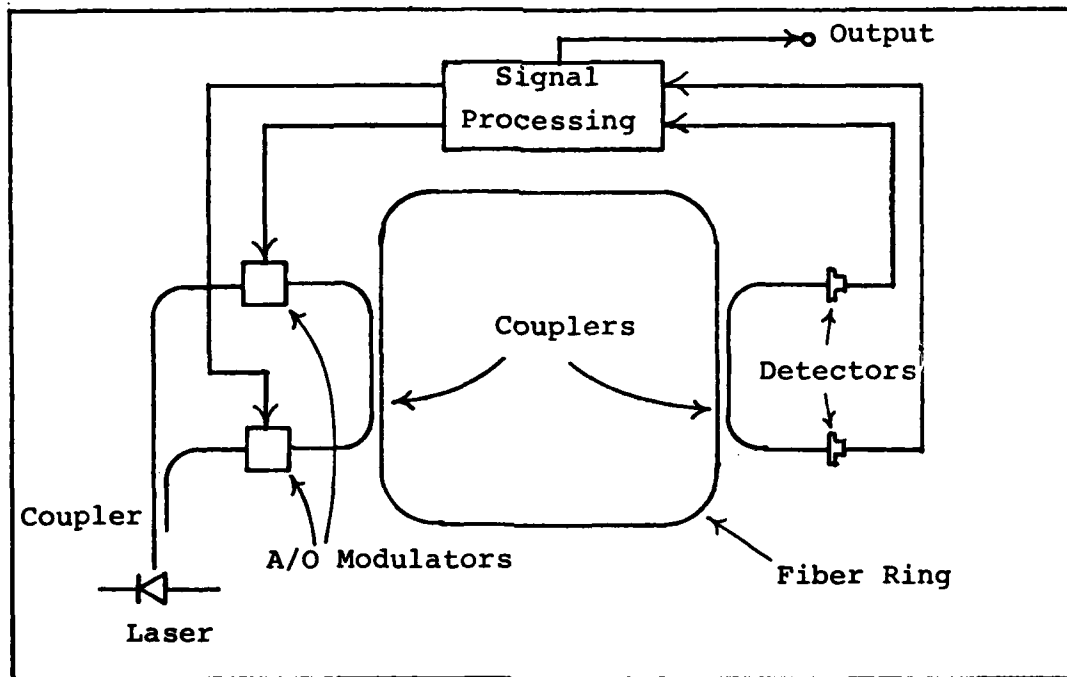


Figure 3.6 Fiber Ring Resonator

the following technological advances that are required to make a practical resonator gyro: 1. narrow line diode lasers, 2. splicing of birefringent single mode fibers, and 3. polarization preserving single mode couplers.

Sensitivity Analysis of the Fiber Gyro

Sensitivity Based on Interference Pattern Alone.

The signals exiting the ring can be represented as simple cosine waves before interfering. The form is

$$A \cos(kz - wt + \delta + K)$$

where z is the path length, ω is the radian frequency of the light (assuming single mode operation). The Sagnac phase shift is δ and K is an additional phase shift introduced by the signal processing or some other change in the path such as defocusing the coupling optics. When the two beams are added the resulting amplitude is:

$$\begin{aligned}
 A_T^2 &= (A_1 + A_2)^2 \\
 &= (A_1 \cos(kz - \omega t + \delta_1 + K_1) + \\
 &\quad A_2 \cos(kz - \omega t + \delta_2 + K_2))^2 \\
 &= A_1^2 \cos^2(kz - \omega t + \delta_1 + K_1) + A_2^2 \cos^2(kz - \omega t + \delta_2 + K_2) + \\
 &\quad 2A_1 A_2 \cos(kz - \omega t + \delta_1 + K_1) \cos(kz - \omega t + \delta_2 + K_2)
 \end{aligned}$$

Taking the time average (Ref 49) over a period τ yields for the first two terms

$$A_1^2 \frac{1}{\tau} \int_0^\tau \cos^2(kz - \omega t + \delta_1 + K_1) dt =$$

$$A_1^2 \frac{1}{\tau} \int_0^\tau [1/2 + \cos(2(kz - \omega t + \delta_1 + K_1))] dt = \frac{1}{2} A_1^2$$

likewise

$$A_2^2 \frac{1}{\tau} \int_0^\tau \cos^2(kz - wt + \delta_2 + K_2) dt = \frac{1}{2} A_2^2$$

The cross term product can be written as

$$A_1 A_2 [\cos(\delta_1 - \delta_2 + K_1 + K_2) + \cos(2kz - 2wt + \delta_1 + \delta_2 + K_1 + K_2)]$$

using the trigometric identity

$$\cos X \cos Y = \frac{1}{2} [\cos(X+Y) + \cos(X-Y)]$$

Averaging over τ as before yields:

$A_1 A_2 \cos(\delta_1 - \delta_2 + K_1 - K_2)$ since the second term in the above equation averages to zero. The amplitude squared is now

$$\bar{A}_T^2 = \frac{1}{2} [A_1^2 + A_2^2] + A_1 A_2 \cos(\Delta\phi - \psi)$$

$\Delta\phi = \delta_1 - \delta_2$ and is the Sagnac phase shift

$\psi = K_1 - K_2$ and is the nonreciprocal shift

\bar{A}_T^2 indicates averaged amplitude which is the case for any real detection scheme.

In order to simplify the analysis, it is now assumed that the amplitudes are equal. Thus $A_1 = A_2 = A$

$$\bar{A}_T^2 = A^2 [1 + \cos(\Delta\phi + \psi)]$$

or for power

$$P_T = P[1 + \cos(\Delta\phi + \psi)]$$

where P is the power contained in each wave, and $P = \frac{P_o}{2}$

where P_o is the total power into the interferometer. Note that this equation gives the expected range of output intensity as a function of the Sagnac phase shift. With no losses, the output intensity varies from zero up to the full intensity of the input, with an average value of $\frac{1}{2} P_o$. If $\psi = 0$, the signal portion has the least sensitivity (since it is a cosine function) at low values of $\Delta\phi$. That is, small fluctuations of $\Delta\phi$ about zero yield small changes in the output intensity. By introducing a phase shift of $\psi = \frac{\pi}{2}$ into the path (non-reciprocal) the sensitivity becomes maximum for small $\Delta\phi$. This is known as operation in quadrature.

This section presents the sensitivity based on no losses or external noises. The effects of component loss and

the addition of noise to the system is considered next.

Effect of Component Loss. In any real fiber gyroscope, the components reduce the power level that is available at the output. Fibers attenuate, and the beamsplitters divide the signal. In both of the proposed plans, acousto-optic modulators are required and these have an associated diffraction efficiency.

Consider Figure 3.7 which is a simplification of Plan A. Assume that the laser has output power P_o . The two beamsplitters are taken to be lossless with a power reflection coefficient (α_1) of $\frac{1}{2}$. (i.e., designed for a 50/50 split). As the beam passes through BS1, the transmitted part is $P_o(1 - \alpha_1)$. This attenuated beam then passes to BS2 which splits it into two equal intensity beams, each of power $\frac{1}{2} P_o(1 - \alpha_1)$ or $\frac{1}{4} P_o$. The waves are then coupled to the fiber. One must first pass through the acousto-optic modulator which deflects part of the energy to the first order mode with efficiency $E_{a/o} = \frac{I_{\text{diff}}}{I_{\text{incident}}}$. It is then coupled into the fiber with coupling efficiency E_c . The power in this beam is now $\frac{1}{2} E_c E_{a/o} P_o(1 - \alpha_1)$. The other beam is coupled into its end of the coil with the same efficiency E_c and its power is $\frac{1}{2} E_c P_o(1 - d_1) = \frac{1}{4} E_c P_o$.

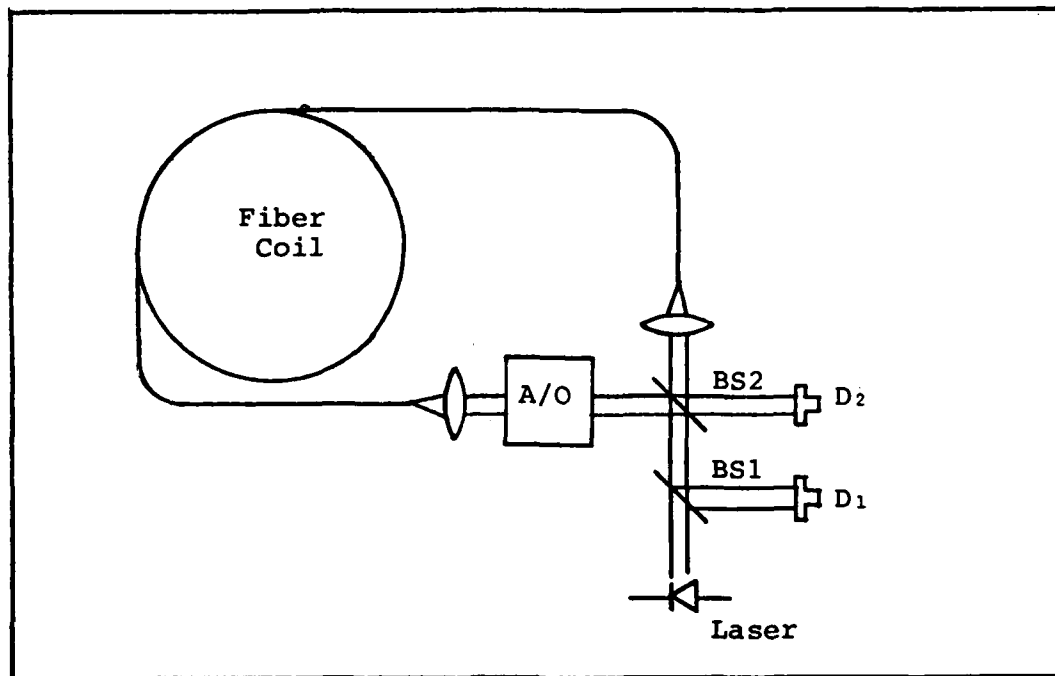


Figure 3.7 Fiber Ring For Loss Analysis

If the total power loss in the fiber follows an exponential law with attenuation coefficient α , and the loss is the same in both directions, then the power of the first beam is

$$\frac{1}{2} E_c E_{a/o} P_o (1 - \alpha_1) e^{-\alpha L}$$

where L = total length of the fiber. The second beam has the same power since it too passes through the A/O and is deflected after traversing the fiber. It is now assumed that both beams are 100 percent recollimated.

The cw beam undergoes one more reflection and the ccw beam has one more transmission before they form an interference pattern at D_2 . The power in each beam is thus.

$$P = \frac{1}{4} E_c E_a / o P_o e^{-\alpha L}$$

which for 50/50 beamsplitter is

$$P = \frac{1}{8} E_c E_a / o P_o e^{-\alpha L}$$

The fringe pattern at D_1 has a power in each beam of $\frac{1}{2}$ the value at D_2 .

$$P = \frac{1}{16} E_c E_a / o P_o e^{-\alpha L}$$

The combined waves emerging from BS2 undergo one more reflection before hitting D_2 , so the oscillations at D_1 and D_2 are out of phase in general. This phase difference is usually taken to be 180° .

The power levels calculated here are the average values available for detecting the Sagnac phase shift. The intensity will vary about this value as a function of $\Delta\phi$. This variation is the signal of interest. A number of noise sources degrade this signal further, preventing the theoretical sensitivity level from being reached. These noise sources are the subject of the next section.

Noise Sources. There are two classes of noise associated with the fiber gyro, those of the detection process and noise sources originating in the optic fiber. A third type, due to fluctuations in the laser source, is also present and its effects are discussed in Chapter V. It can easily be eliminated by the differential detection scheme. The discussion here follows closely that of Lin (Ref 25) with additional material coming from several other authors (Ref 7, 17, 49).

Noises associated with the detection process are shot noise, thermal, generation-recombination, flicker ($1/f$), dark current, and amplifier noise. Problems in the fiber arise from scattered light, and environmental effects such as thermal variations, and acoustic and mechanical vibrations.

Detector Associated Noises. The minimum detectable phase shift as limited by shot noise can be found by calculating the signal to noise ratio. For the case of a non-reciprocal phase shift of $\pi/2$ the phase shift power is

$$\begin{aligned} P_T &= P[1 + \sin\Delta\phi] \\ &= P[1 + \Delta\phi] \end{aligned}$$

for $\Delta\phi$ small, this can be written as

$$P' = P + \Delta P$$

where $\Delta P = \Delta\phi P$ resulting in a ratio

$$\frac{\Delta P}{P} = \Delta\phi$$

which is a result of ignoring the DC part of the signal, and is the ratio of interest.

By using a detector with quantum efficiency η , the signal current is given by

$$S = \eta q P/\hbar\omega$$

where q is the electronic charge. The shot noise inherent in the signal is

$$S_N = \sqrt{2qSB}$$

where B is the detection bandwidth.

The shot noise level is now taken to be the minimum detectable change in signal, that is

$$\Delta S = S_N$$

then

$$\Delta S = S(\Delta P) = \eta q \Delta P / \bar{h}\omega = S_N$$

or

$$\frac{\eta q \Delta P}{\bar{h}\omega} = [2q(\eta q P / \bar{h}\omega) B]^{\frac{1}{2}}$$

and

$$\frac{\Delta P}{P} = [2\bar{h}\omega B / \eta P]^{\frac{1}{2}}$$

The shot noise limited minimum detectable phase shift is thus

$$\Delta\phi = \sqrt{2\bar{h}\omega B / \eta P}$$

A similar discussion leads to the quantum noise limited phase shift of

$$\Delta\phi = \sqrt{\bar{h}\omega B / \eta P}$$

which is less than the shot noise limit (Ref 47). The combined noises yield a limitation of

$$\Delta\phi = \sqrt{3\hbar\omega B/\eta P}$$

by simply adding signal powers since the two processes are considered independent.

The phase shift expression (Eq. 3-7) can be used to find the overall sensitivity of the gyro due to shot and quantum noise.

$$\Delta\phi = \frac{8\pi NA\Omega}{\lambda c} = \sqrt{3\hbar\omega B/\eta P}$$

or

$$\Omega_{\min} = \frac{\lambda c}{8\pi NA} \sqrt{3\hbar\omega B/\eta P}$$

which is the minimum observable rotation rate considering shot and quantum noises.

Taking into account the component losses developed for the fiber gyro in the previous section

$$P = \frac{1}{8} E_c E_a / o^P_o e^{-\alpha L}$$

the minimum detectable rotation rate is now

$$\begin{aligned}\Omega_{\min} &= \frac{\lambda c}{8\pi NA} \sqrt{24\hbar\omega B/\eta E_c E_a / o^P_o} e^{-\alpha L} \\ &= \frac{\lambda c}{8\pi NA} \sqrt{24\hbar\omega B/\eta E_c E_a / o^P_o} e^{\alpha L/2}\end{aligned}$$

Flicker noise ($1/f$) is common to all solid state devices. It is called $1/f$ noise because it has a $1/f^a$ power spectrum where $0.8 < a < 2.0$ usually. It is mostly of concern at very low frequencies (Ref 25). But at this low end, it can be orders of magnitude greater than the shot noise. This is one of the reasons for using modulation and an a/c detection scheme. The modulation frequency must be selected to be above the cutoff of the $1/f$ noise associated with the particular detectors used.

Light Scattering in the Fiber

Various scattering mechanisms add to the noise present at the output of the gyro. Parts of the scattered light are trapped in the core and appear at both ends of the fiber, others are coupled out of the core and lost. The major scattering mechanisms are Rayleigh scattering, Mie scattering, core-cladding interface scattering, and Brillouin. Another type is Raman scattering but since its scattering coefficient is 10 to 20 times smaller than that of Brillouin, it is typically not considered for the fiber gyro. All of these components oscillate at the same frequency as the input laser beam except for Brillouin scattering which has a slight frequency shift in the back-scattered direction (Ref 26). Rayleigh scattering is an optical interaction with density fluctuations. Brillouin

scattering is an interaction of photons with acoustic phonons. The Rayleigh and Brillouin components are equally distributed in both directions, while those due to Mie and core-cladding interface scattering are in the forward direction only. The Mie scattering, which is caused by large imperfections on the order of $\sim \lambda/10$, has an angular dependence. As the size of the scattering particle approaches λ , the scattering can become very intense. This is the same type of scattering that occurs for a change in the optical axis, (microbending loss).

The Mie and core-cladding interface scattering are thought to be the cause of a strong forward peak that is observed. This peak has an effective scattering coefficient (α_{FP}) of about one-fifth that of the Rayleigh coefficient (α_{SR}).

A word about scattering coefficients is now in order. The coefficient is a constant factor in the exponential distribution law for light power in the fiber. For example, the forward unscattered part of the beam follows:

$$P(x) = P_i e^{-\alpha x}$$

where x is any point along the fiber and α is an attenuation coefficient. Because of the trapping and attenuation experienced by the scattered light, the forward and back scattered light components are distributed according to

$$P_s(L) = F P_o \alpha_s e^{-\alpha L} L$$

$$P_s(0) = B_t P_o \frac{\alpha_s}{2\alpha} (1 - e^{-2\alpha L})$$

where $P_s(L)$ is the power out due to forward scattering of a fiber of length L , and $P_s(0)$ is the backscattered light at the input. The associated scattering coefficient for the process in question is α_s , and F and B_t are the percentages of light trapped in the forward and back directions.

These trapping factors have been derived and are given by Lin (Ref 25) as

$$F = \frac{1}{2} [1 - \frac{3}{4} (\frac{1}{n_{core}} + \frac{1}{3n_{core}^3})]$$

for a bare cladding fiber, and

$$F = \frac{1}{2} [1 - \frac{3}{4} (\frac{n_{clad}}{n_{core}} + \frac{n_{clad}}{3n_{core}^3})]$$

for a fiber immersed in index fluid (mode stripped). n_{clad} is the refractive index of the cladding and n_{core} is that of the core. In general $B_t = F$ due to symmetry. The trapping factor is a measure of how much of the scattered light is guided out. Lin made comparisons of the mode stripper vs. the bare cladding case and for a typical fiber he found that the use of a mode stripper reduced the trapping factors by

about 100 times for the Rayleigh as well as the Brillouin component.

The scattering coefficients are a strong function of wavelength, both Rayleigh and Brillouin coefficients follow a $1/\lambda^n$ distribution law). The trapping factors, (since they are a weak function of the index of refraction, which does not vary in fused silica for wavelengths of 0.6 to 1.3 μm), are essentially constant for the wavelengths of interest. A summary of typical scattering factors (in terms of effective-cross sections) for a fused silica fiber is given in Table 3.1.

Component	Direction	Trapping Factor		Scattering Coeff.	
		Bare	Mode Stripper	$\lambda = .633 \mu\text{m}$	$\delta = 1.1 \mu\text{m}$
Direct Beam	+	100%	100%		
Rayleigh	+	$F=0.2$	2.3×10^{-3} cm^{-1}	6.93×10^{-6} cm^{-1}	7.46×10^{-7} cm^{-1}
	-	$B=0.2$ t	2.3×10^{-3} cm^{-1}		
Brillouin	+	$F=0.2$	2.3×10^{-3} cm^{-1}	9.24×10^{-7} cm^{-1}	0.993×10^{-7} cm^{-1}
	-	$B=0.2$ t	2.3×10^{-3} cm^{-1}		
Forward Peak	+	$F=1$	<1	$\frac{1}{5} \alpha_{\text{sr}}$	$\frac{1}{5} \alpha_{\text{sr}}$

Table 3.1 Summary of Scattering Data for a Typical Fiber
Where + and - indicate forward and backward direction.

It can be seen that it is better to use a longer wavelength, and heavy mode stripping is advised.

Effect of Coherence Length on Rayleigh Scattering.

The previous discussion leads to the conclusions that Rayleigh scattering is the predominate noise contributor in an optic fiber. Recently, there has been an attempt to reduce its contribution to the detected signal (Ref 7, 12). The phase of the Rayleigh scattered light has been observed to fluctuate with a characteristic time constant of 0.01 - 1 sec. due to vibration and temperature fluctuations. This fluctuation is superimposed upon the rotation induced Sagnac phase shift and degrades the output sensitivity.

Böhm (Ref 7) has calculated the effects of reducing the coherence time (τ_c) on the backscattered light power. The coherence time is another measure of the relative coherence of a light wave and is equal to

$$\tau_c = \frac{d_1}{c}$$

where d_1 is the coherence length as described previously.

τ_c is thus proportional to the coherence length.

Böhm gives the minimum observable rotation rate, for a highly coherent source, as a function of Rayleigh scattering as

$$\Omega_{\min} = \lambda c (R_o/T_o)^{1/2} / 8\pi NA$$

Where R_o is that fraction of the input power back-scattered by a fiber of length L . The resulting amplitude ratio of backscattered to transmitted light at the output of the fiber is $(R_o/T_o)^{1/2}$. If the transmitted and scattered light are coherent, their superposition may affect the phase of the output beam by up to $\pm(R_o/T_o)^{1/2}$ (rad).

In evaluating the backscattering factor, R_o , reflections at the discrete optical interfaces are ignored since they can be avoided by careful design and use of antireflective coatings. Brillouin scattered light is also ignored as it is frequency shifted. The Rayleigh backscatter is given by:

$$R_o = (\frac{B\alpha}{t_{sr}}/2\alpha)(1 - T_o^2)$$

where α_{sr} is the scattering coefficient due to Rayleigh, and α is the total attenuation of the fiber. T_o follows the usual exponential law

$$T_o = e^{(-\alpha L)}$$

The backscatter noise is reduced considerably by the use of a laser whose coherence time τ_c is considerably shorter than the group delay time of the fiber (τ_o), or

$\tau_c \ll \tau_o$, (i.e., the coherence length is much shorter than the fiber length). Thus only a fraction of the backscattered light can interfere (τ_c/τ_o) with full contrast. Also the interfering fraction is assumed to be centered at $L/2$. So the Rayleigh backscattering is reduced and is

$$R_o = \alpha_{sr}^{LBT} \tau_o (\tau_c/\tau_o)$$

and is the value to be used in the equation for minimum rotation rate. If the laser oscillates with m independent longitudinal modes a further reduction of \sqrt{m} can be expected.

Böhm reports the results of using a short coherence length GaAs laser with 12 modes in a 2 mm wide region at $\lambda = .854 \mu\text{m}$ compared to a HeNe laser. A reduction of the backscattered light by an order of magnitude is observed. A short-time noise equivalent rotation rate of

$$\Omega_{min} = 8 \times 10^{-4} \text{deg/sec}$$

is measured.

An alternative to reduction of the backscattered noise is offered by Cutler (Ref 12). A pulsed technique is presented where short pulses are allowed (1 msec) and the output is gated so that only the scattered energy from a short section of the fiber contributes to the noise level

The pulses can also be frequency modulated. These techniques require careful investigation of the effects of pulsing on the wavelength and linewidth stability of the GaAs laser diode.

IV. Experiment

Light Source Selection

The first problem encountered in designing an incoherent fiber gyro is the selection of a suitable source. This source must have the characteristics of low coherence and totally random polarization, as well as providing enough power output to overcome expected losses in the discrete optical components in the signal path.

A light-emitting-diode (LED) has the incoherence and polarization properties desired and can provide high power. However, beam divergence properties of the LED make it less than desirable for maximum coupling efficiency to the optic fiber. A laser diode, while providing good beam collimation potential (due to it's small output aperture), does not possess the incoherence and random polarization properties desired.

The main objective of the first experiments was to evaluate various LED's and one injection laser along with beam shaping techniques to determine the best source to use. Three visible wavelength and two infrared LED's were evaluated for power output and a lens system was designed for best collimation of the beam. One laser diode was also tested using a 20X microscope for collimating it's output beam. This section discusses the results of these tests.

The laser diode was chosen as the source since it was discovered that a reasonable amount of power was obtained from it while operating in the LED regime, (below lasing threshold).

Light Emitting Diodes. An experiment was first conducted using an ordinary visible (Red) LED of the type used for panel indicators. The device was mounted in a plastic collar which was fixed to a circuit board. The mount was then placed in an adapter plate as part of an optical bench rail system fabricated from a standard kit (Ref 55).

Figure 4.1 shows a schematic of the experimental set-up and lens focal length which resulted in the best collimation of the red beam.

The DC power supply voltage was adjusted for desired current as monitored by the digital multimeter (DMM). R_l was a 130Ω current limiting resistor. The F10 lens was adjusted so the source is slightly off from its focal length. This caused the beam to converge and then diverge between the lenses. The output F50 lens served to converge the beam but did not refocus it and produced an approximately Gaussian shaped beam with a waist size of 1.5 cm. This was the best result that could be obtained using the relatively large spot size and rapid divergence of the red

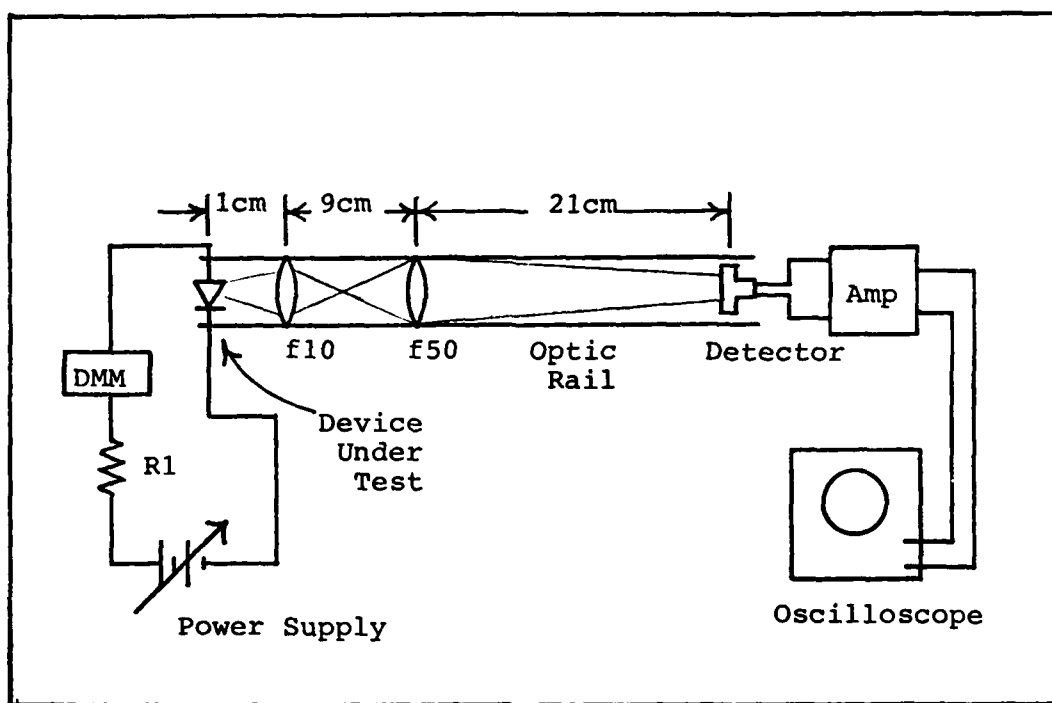


Figure 4.1 LED Test Set-up

LED. When viewed right into the plastic dome lens, the spot was approximately 0.5 cm in diameter.

Three visible and two IR devices were tested. Table 4.1 shows the types, lens configurations and other specifications of all types tested. Initially, only the first four types were looked at. The fifth, designed for short length fiber systems was later compared with device #4.

Device	Type	Lens	λ	Dispersion Angle	Max Current
#1	visible	plastic dome	-	large	30ma
#2	visible	plastic fresnel	700 μm	diffused	30ma
#3	visible point source	plastic dome	-	large	30ma
#4	IR	plastic dome	880 μm	24°	60ma
#5	IR	glass dome	940 μm	12°	100ma

Table 4.1 LED Types

Intensity output for each diode as a function of current was measured using a PIN 6D photodetector. Relative voltage output of the detector electronics was recorded. Figure 4.2 shows the results of this comparison.

As can be seen, the infrared diode far out performed the visible wavelength types. It was noted that the sensitivity curve of the photodetector peaked between 800 μm and 900 μm but the difference in sensitivity did not account for the power advantage of the IR diode. For a more complete discussion of the photodetectors, see Appendix F.

An improved detector circuit was then constructed using the PIN 10D and PIN 10 photodetectors, since these devices had BNC connectors which allowed easy attachment to coaxial cable. This arrangement allowed the detector head to become

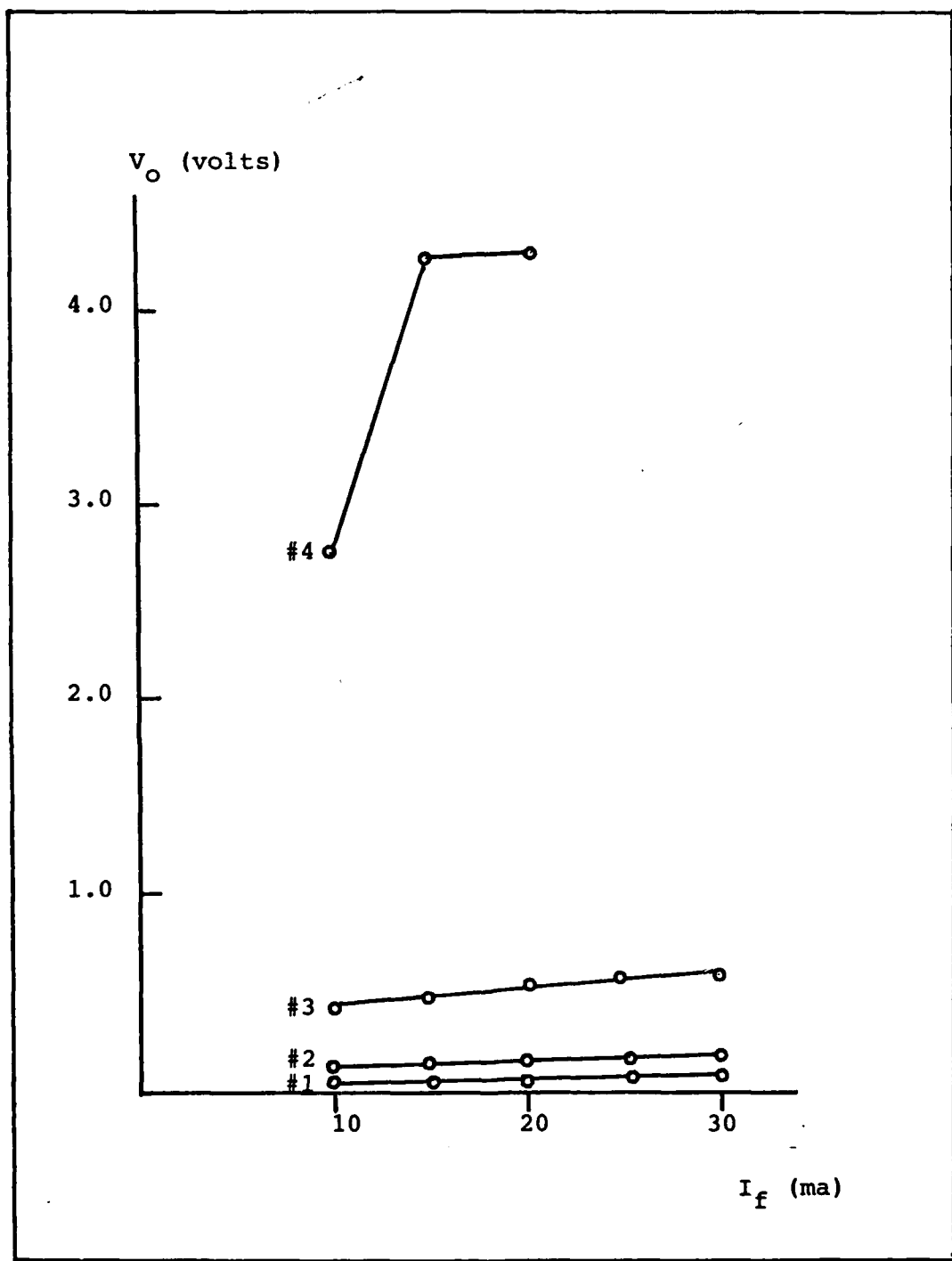


Figure 4.2 LED Intensity

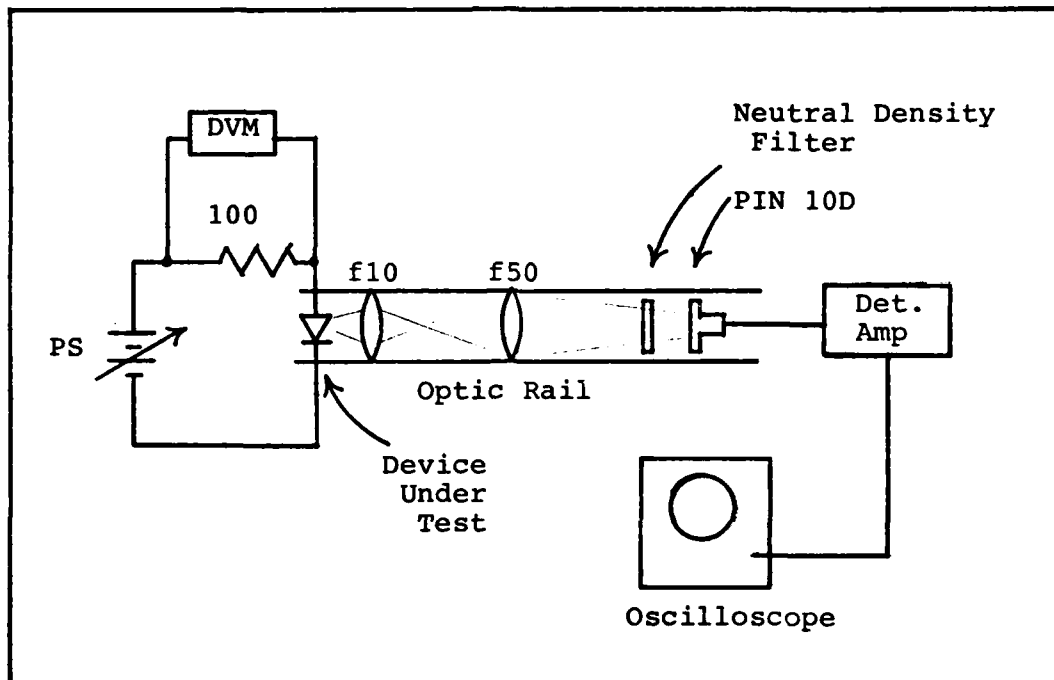


Figure 4.3 Improved Set-up

movable and it acted as a "roving eye" which proved very useful for characterizing the invisible IR beams. Additionally, the experimental set-up was modified to improve current monitoring. A schematic of this arrangement is given in Figure 4.3. This was used to compare the two IR LED's. Power curves were taken for LED #4 and #5, with forward currents from 20 mA up to the maximum ratings. A 1/20 power neutral density filter (NDF) was used to prevent saturation of the detector amplifier and ensure the Pin diode was operating in the linear region. The measured intensity is plotted in Figure 4.4. In each case, the lenses were adjusted slightly on the optic rail to obtain

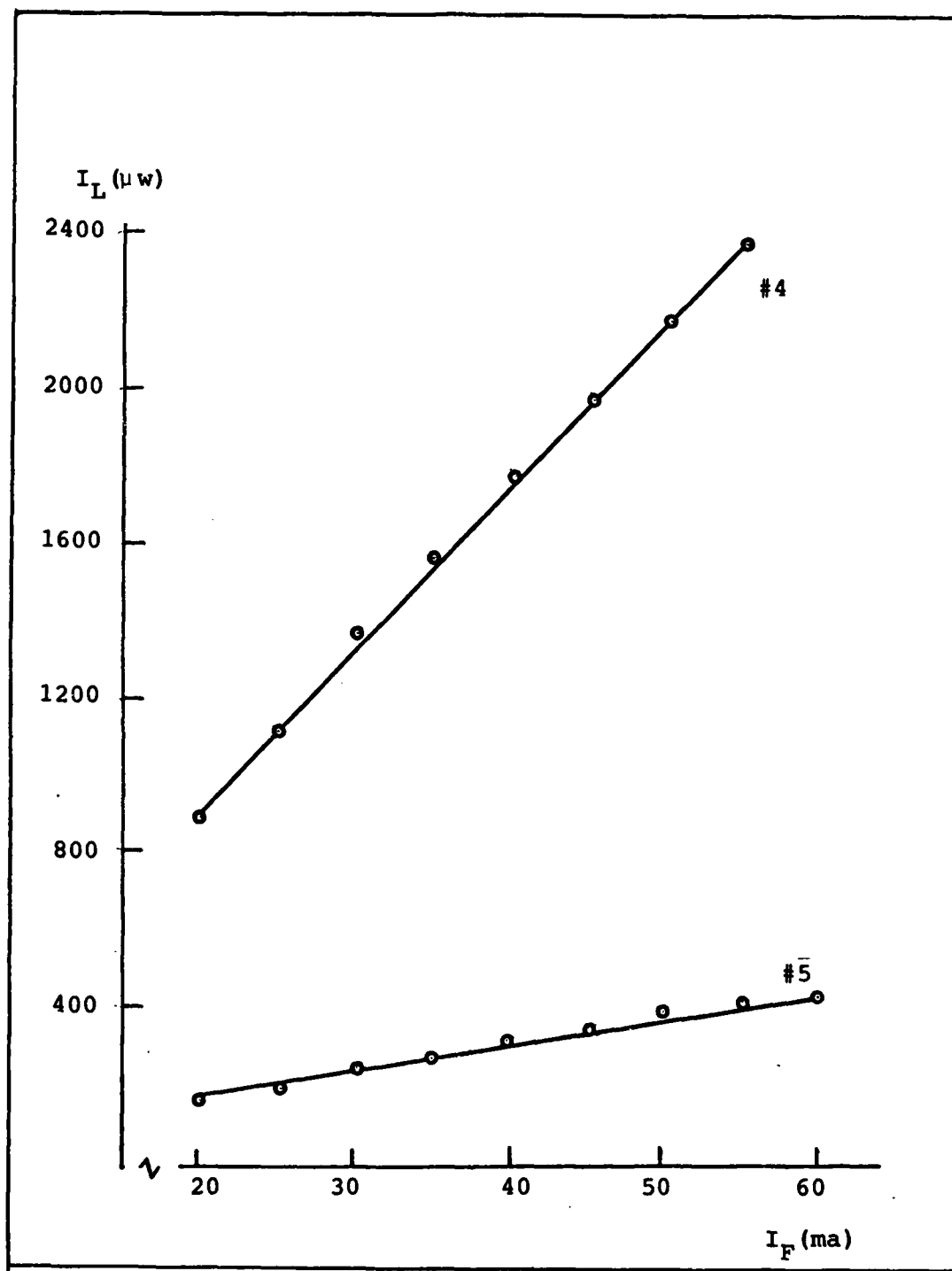


Figure 4.4 Power of Two IR LED's

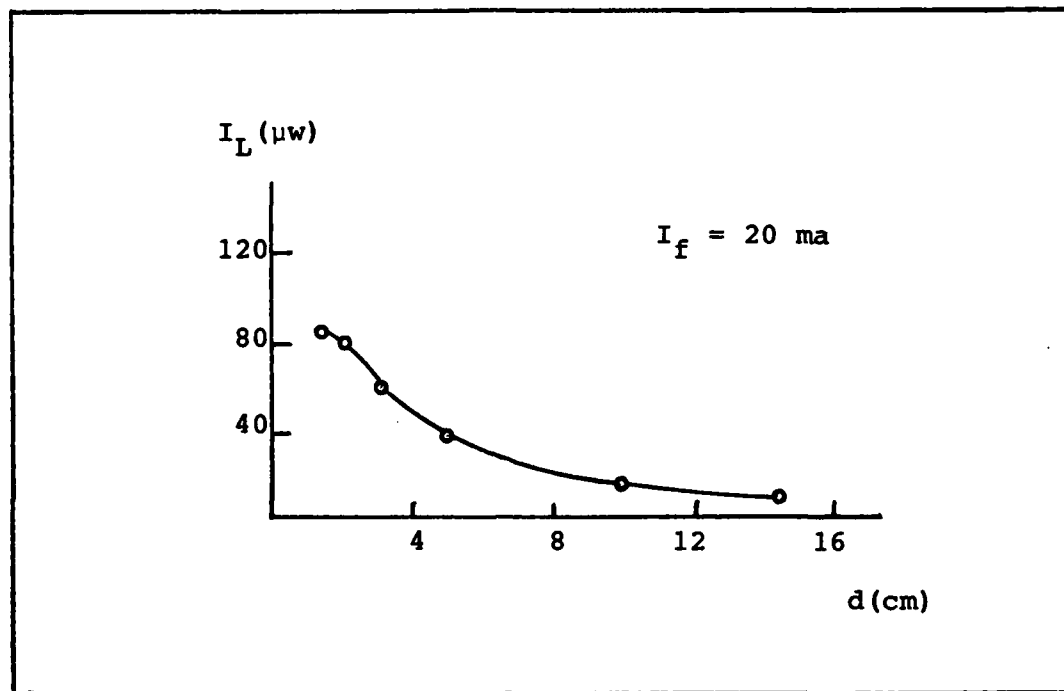


Figure 4.5 Intensity vs. Distance to Detector for Device #5

a peak output of the detector. Since the two LED's had different size lenses the optics had to be peaked for each one to obtain a reasonable comparison. As can be seen, device #4 had far better output.

In order to ensure that the optics were not in fact "spoiling" the transmission of device #5's beam, a test was performed without any lenses. Device #5 had a much narrower radiation pattern than #4 and its dispersion was checked. The device was run at $I_f = 20$ mA while the detector distance (d) was varied. Results are plotted in Figure 4.5. In this case a 1/2 power NDF was used.

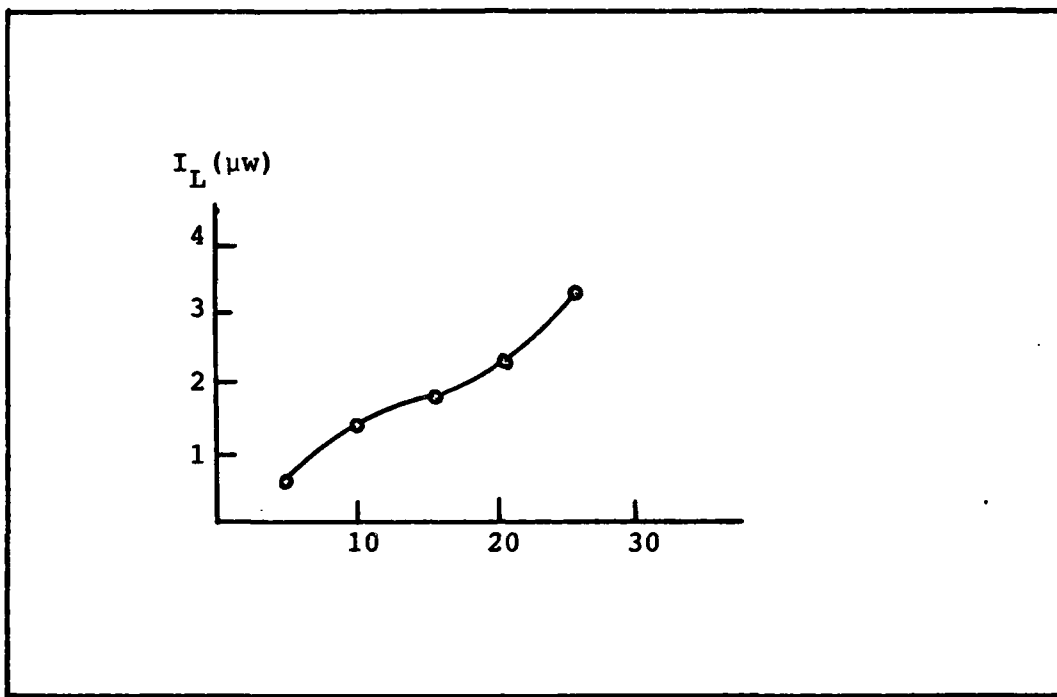


Figure 4.6 Intensity vs. Current,
 $d=18$ cm, device #5

Next, a curve of total power received as a function of I_f was obtained, for a distance of 18 cm which corresponded to the set-up with the lenses in. This plot is Figure 4.6.

One final check was performed to compare the IR LED's total output at their nominal operating points. For device #4, this current was $I_f = 20$ mA and for device #5 I_f was 50 mA. Distance of the detector from the diode output lenses was 1.5 cm. A 1/20 NDF was used and device #4 was measured at 1.55 mW while device #5 measured .8 mW. In terms of power output, device #4 had the greatest available

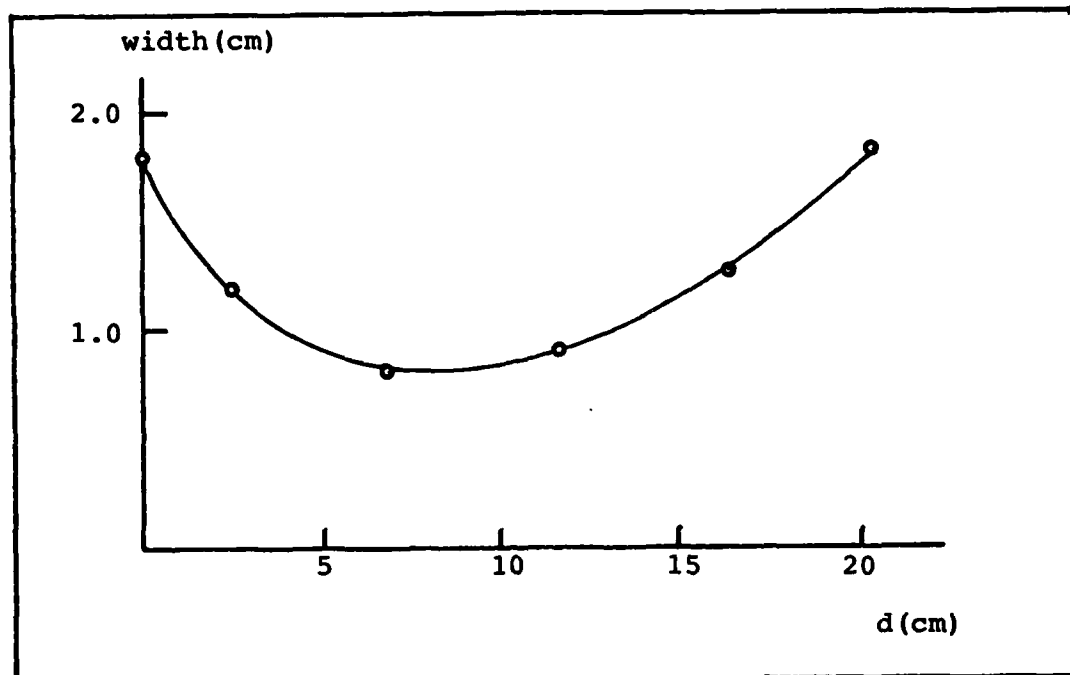


Figure 4.7 Beam Shape From Device #4

power and the characteristic of its' beam through the lens system was next studied for applicability to the gyro design.

The half power beam width as a function of distance from the F50 lens was obtained using a PIN 6D detector on a cable as a probe. At a given distance, d , the probe was adjusted for a peak indication on the oscilloscope. The probe was then moved to the side until the voltage output dropped to half. The distance travelled was noted as $1/2$ the total half power beam width at d . Results shown in Figure 4.7 clearly indicate the Gaussian shape of the beam.

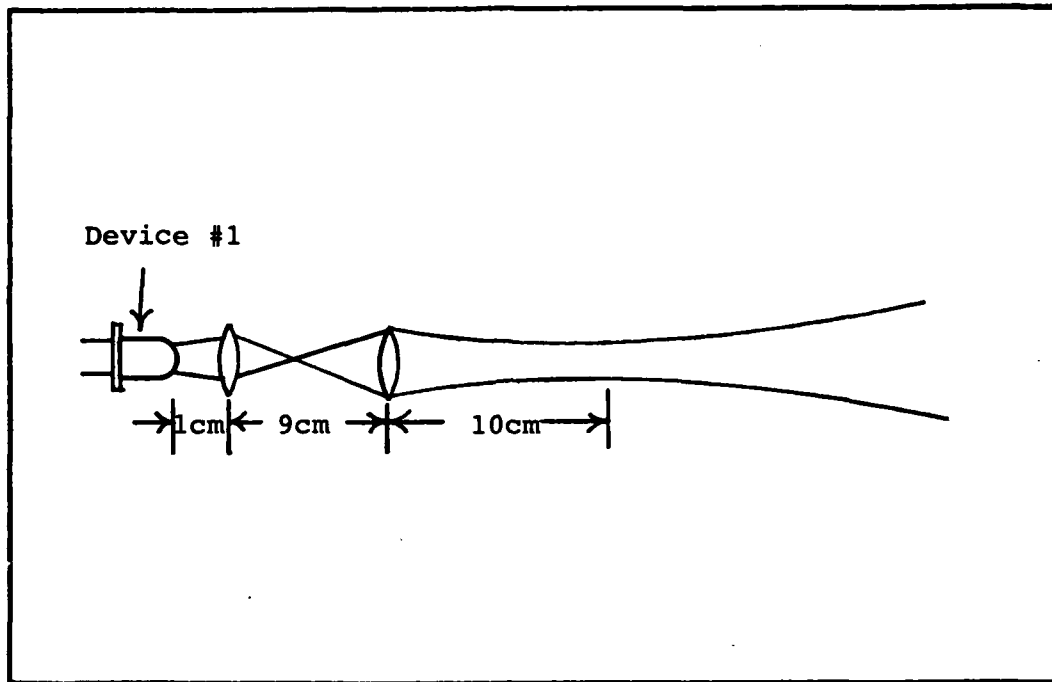


Figure 4.8 Qualitative Beam Shape Using Red LED

The observed minimum diameter is 8 mm at $d = 10$ cm from the output F50 lens. To get a clearer picture of what this beam looked like and to make sure that the perceived minimum was a Gaussian waist and not a focus, a visible LED was replaced into the system. This device had the same type lens as the IR diode and the beam was qualitatively the same shape. The red beam was observed on a movable screen and the general shape is seen in Figure 4.8. The fact the rays were not crossing outside the system was verified by aperture blocking at various locations between the lenses and observing the spot at its minimum at 10 cm.

The question remaining at this time was; was this suitable for use in the fiber gyro? The first critical component that the beam encountered after the beam splitting process was the acousto-optic modulator. From a mechanical design standpoint, it would have been possible to place the A/O so that the waist of the beam has centered in the crystal. It was known that for maximum deflection efficiency, the entire light beam must interact with the entire width of the acoustic column (Ref 52). These modulators had a column width of 2 mm and had corresponding 2 mm apertures at the input and outputs. A rather simplified calculation of what power can be passed through such an aperture was made. Consider Figure 4.9, which is a cross section of a 2 mm aperture superimposed on the minimum beam diameter.

Assuming uniform illumination over the beam waist, the expected power transmitted can be found by the ratio of the aperture area to the beam size:

$$\text{Efficiency} = \frac{\pi r_1^2}{\pi r_2^2} \times 100 = \frac{r_1^2}{r_2^2} \times 100 = \frac{(1\text{mm}^2)}{(4\text{mm}^2)}(100)$$

$$\text{Efficiency} = 6.3\%$$

Thus, only 6.3% of the light which passed the beamsplitters was available for acousto-optic modulation. Assuming 50/50 beamsplitters and nominal operation of the LED, the

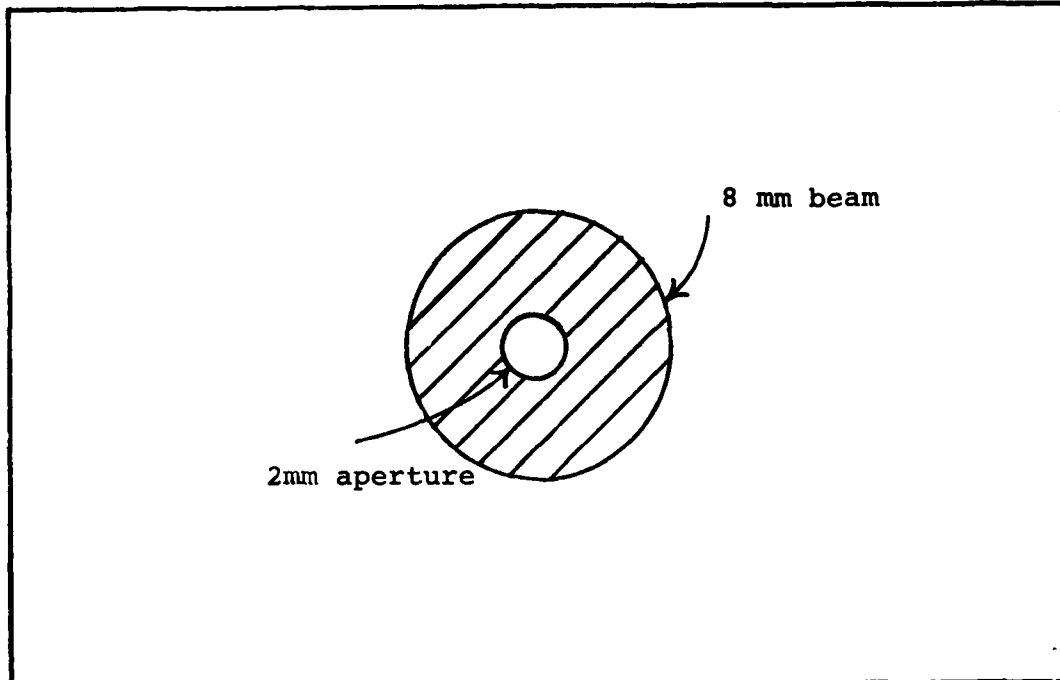


Figure 4.9 Aperturing of Beam

available power to the acousto-optic was estimated. The diode could be operated continuously at 2 mW output. A calculation of losses follows:

$$2 \text{ mW} \times .5 \times .5 \times .063 = 32 \mu\text{watts}$$

It was also known (see Appendix D) that the diffraction efficiency of an acousto-optic modulator is dependent on the ratio of the acoustic divergence to light divergence. To achieve maximum design efficiency this ratio must be greater than 2 (Ref 52). At this time it was felt that power losses due to aperturing the beam and possible acousto-

optic modulator effects would make use of the IED unacceptable. Attention was then turned to the injection laser diode as a potential source.

Laser Diode Characteristics

The first test involving the LCW-10 injection laser was a quick power output check. The device was mounted on a "solder iron" type heat sink which was threaded into its holder. Clip leads were attached and a current (I_{lsr}) was applied. I_{lsr} was monitored with a 100Ω resistor and a DVM. At $I_{lsr} = 100 \text{ mA}$ total power measured was $74 \mu\text{W}$. The power was taken by holding the detector head close to the tip of the heat sink and adjusting for peak reading. By checking the power supply voltage and subtracting the voltage across the load resistor, the diode forward voltage was found to be 1.6 V. No lenses were used at this time so that effects of collimating optics and other components could be determined.

The power output measured was far below the manufacturers specifications but was expected since this diode had been the subject of a previous experiment to investigate anti-reflective facet coatings. This resulted in an increased lasing threshold (I_{th}).

The diode/heat sink was then fitted into a threaded phenolic disc which had been fabricated to fit in the standard adapter plate of the optic rail kit. A 20X

microscope objective (M/O) was mounted in an X-Y-Z translation holder and installed on the rail system. The Z-axis adjustment consisted of two micrometers at either side of the rails pushing against compression springs. This system allowed for side-to-side tilt adjustments. As will be noted in the next section, the proper adjustment of this microscope was most difficult. This was due to the extremely small spot size emitted ($<10 \mu\text{m}$) and wide divergence angle of the beam.

Once a satisfactorily narrow beam had been obtained, a laser power (P_{laser}) versus drive current (I_{laser}) plot was obtained. The results can be seen in Figure 4.10. Power output ran from $<40 \mu\text{W}$ to more than 0.3 mW. Note that at $I_{\text{laser}} = 100 \text{ mA}$; $P_{\text{laser}} = .060 \text{ mW}$, a reduction of 19% from the case without the lens. This loss could have been reduced by the use of a larger numerical aperture (NA) lens but then working distance considerations became a problem. Also, the M/O was not anti-reflective coated for IR wavelengths.

The power was measured using a 1/20 NDF, and the detector aperture adjusted for full beam width. The aperture effectively blocked out any optical noise from the laboratory ambient lighting.

From the graph it is difficult to define lasing threshold, especially since the laser modes do not come in

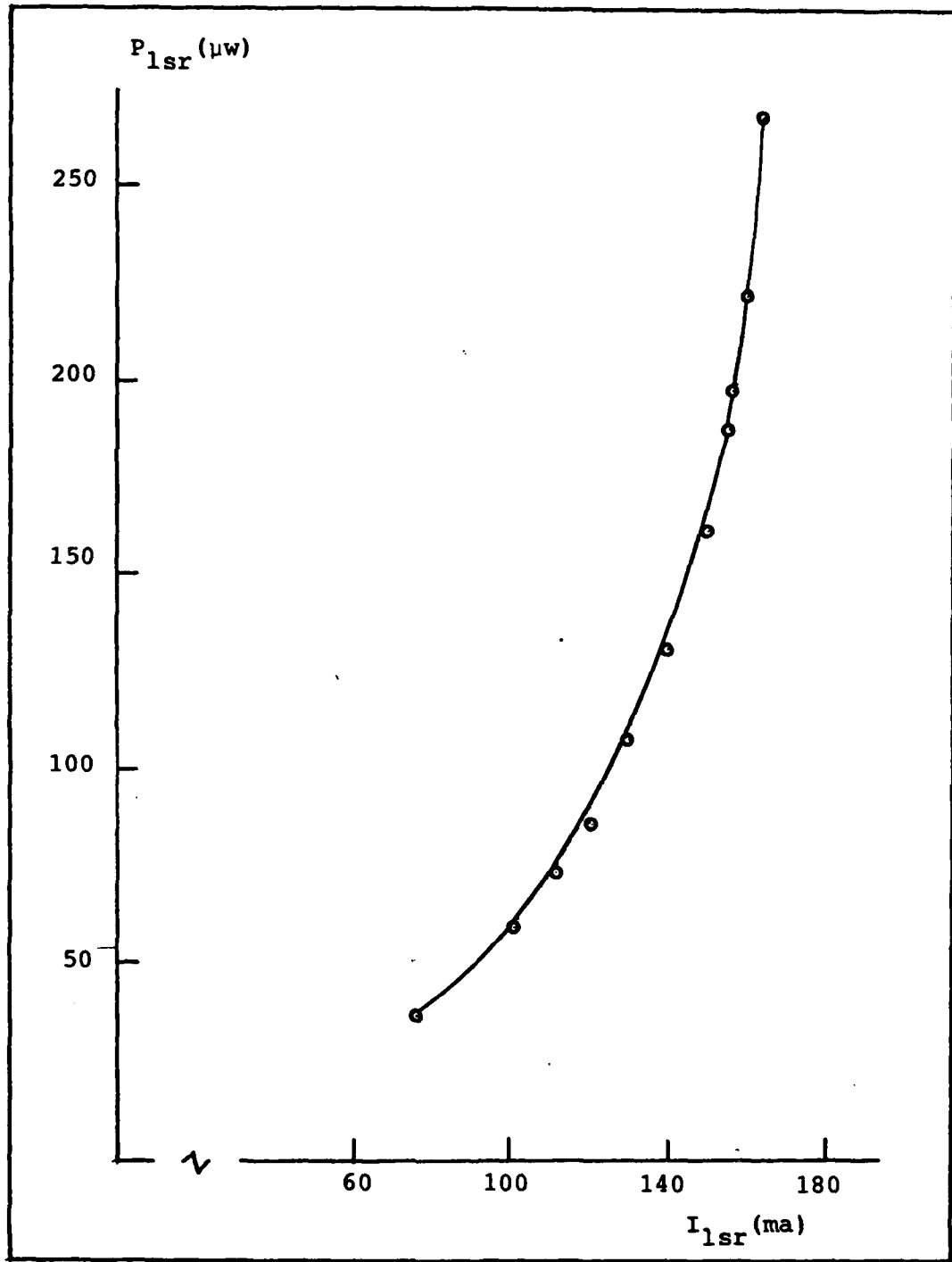


Figure 4.10 Laser Output Through Collimating Optics

suddenly, but they gradually form as current is increased (Ref 42). For the operation of the incoherent gyro, the laser should be operated well below I_{th} for maximum linewidth (See section I-D), and random polarization.

The next test was to determine the relative state of polarization (SOP) as a function of I_{lsr} . A polarizer was placed between the M/O and the detector. This polarizer could be rotated through a full 360° while the detector output voltage was monitored. The output detected was recorded for each arbitrary angle of the polarizer for seven values of I_{lsr} ranging from 130 to 173 mA. A family of voltages recorded vs. angle for each value of I_{lsr} is presented in Figure 4.11. As can be seen, at low values of I_{lsr} , the polarization was random. At higher values the preferred states began forming, with polarization occurring rapidly after $I_{lsr} = 165$ mA.

In order to get a better picture of how rapidly the polarization was occurring, a factor defined as degree of polarization (DP) was calculated.

$$DP = \frac{\text{max. output}}{\text{min. output}} | I_{lsr}$$

It was the ratio of the largest to the smallest voltage output of the detector for a given value of I_{lsr} . It was noted that the highest output was always at either 90° or

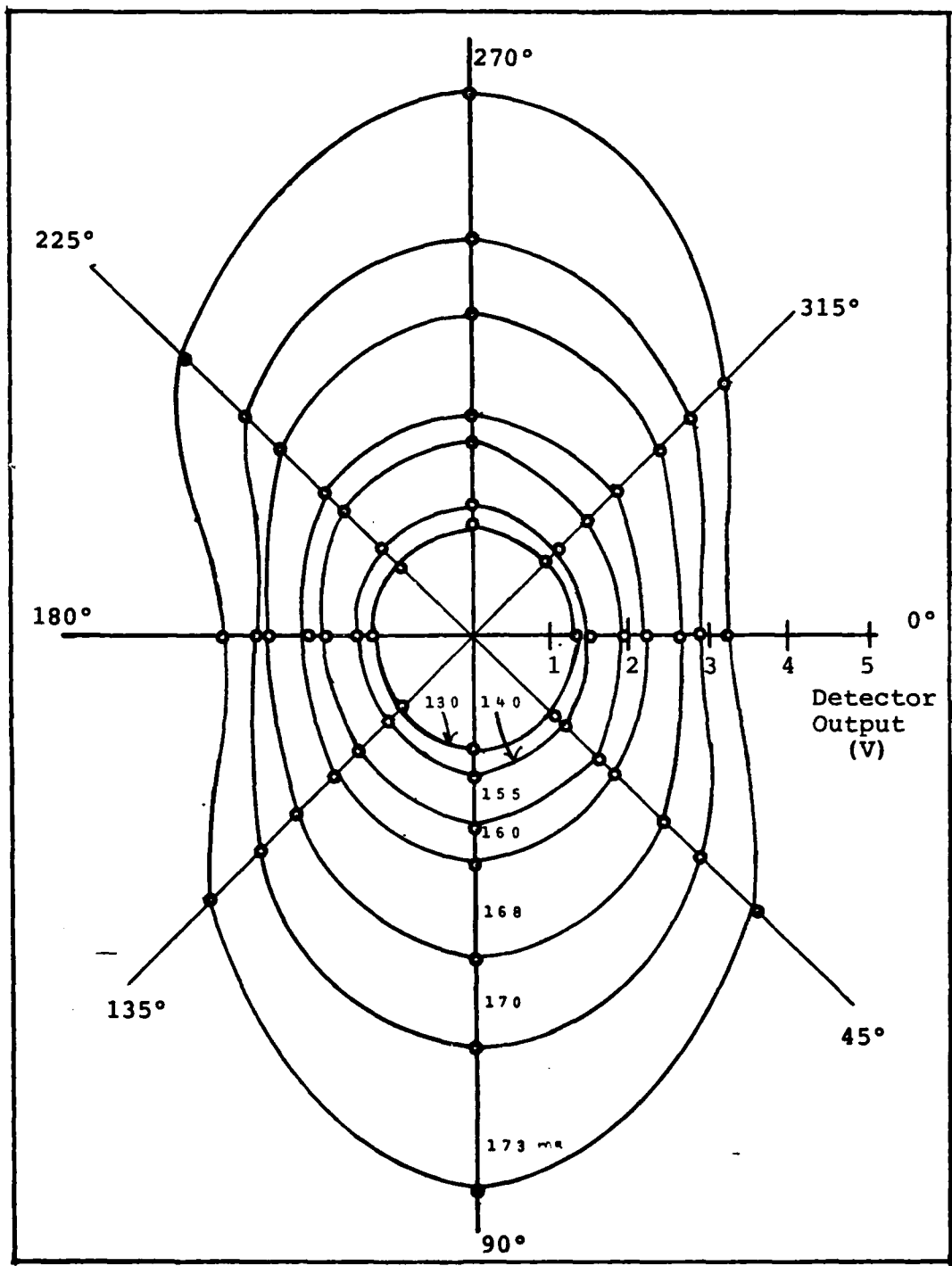


Figure 4.11 Evolution of Laser Beam Polarization

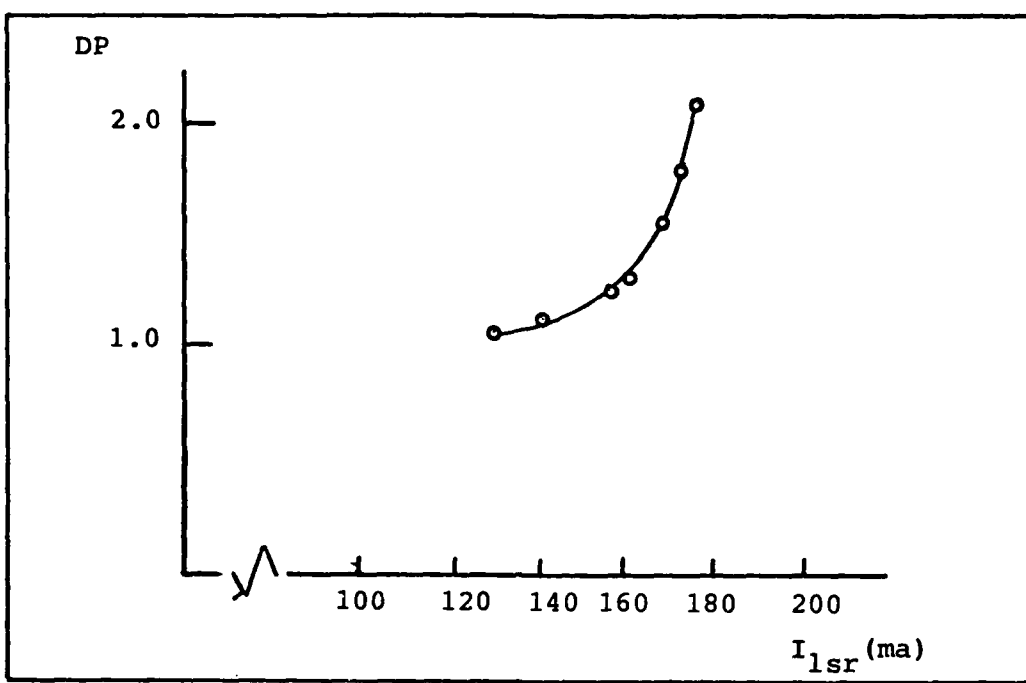


Figure 4.12 Degree of Polarization

270° while the lowest reading was consistently at 180° .

Note that for perfectly random polarization, the value of DP should be 1. A curve of DP versus I_{lsr} is given in Figure 4.12.

As a result of these tests the maximum I_{lsr} at which the gyro can be operated and still have random polarization can be found. Operation below 120 mA should be sufficient for randomness. Incoherence must also be obtained and this can be checked by use of a spectrum analyzer such as a scanning Fabry-Perot Etalon. Injection laser diodes can have a large number of modes just below lasing

threshold. At least one author reports that the diode must be operated 65% above V_{th} for essentially single mode operation (Ref 42). Incoherent operation will require the diode to be in the LED regime, or to have multiple modes which effectively reduce the coherence length.

Collimating and Beam Splitting Optics

The 20X microscope objective was initially mounted in a spring loaded X-Y positioner with Z-axis adjustment accomplished by sliding the adapter plate on the four rails and holding with set screws. This arrangement proved to be most unsatisfactory. The diode/heat sink mount could not be adjusted during laser operation. Visual alignment of the heat sink was only a rough estimate, resulting in the beam not pointing directly down the optical axis of the system. Beam off-axis pointing could be compensated for by twisting the adapter plate slightly and carefully tightening the set screws while monitoring the detector output. This procedure usually resulted in an acceptably collimated beam after about an hour of work. It did not remain stable, however. The beam divergence would change from day to day usually causing great difficulty with other alignment and characterization attempts.

The Z-axis adjustment was improved by the addition of 2 micrometers pushing against 4 compression springs (see

Appendix E). Beam alignment still proved to be difficult but once desired beam characteristics were achieved, the beam was stable for the rest of the experiment.

A note about the alignment procedure is in order at this point. The only tool available for checking the beam was a movable detector head containing the PIN 10D detector and an adjustable aperture. This aperture could be used to determine if the beam was converging or diverging in the following manner. The beam was found at the edge of the mounting plate by obtaining a peak on the scope using a 1 mm aperture by sliding and turning the detector head. The voltage on the scope was noted and the detector head was then moved closer to the output of the M/O. If the power detected increased, the beam was known to be diverging; if it decreased, the beam was converging. The Z-axis positioners were adjusted until a minimum difference was obtained in the voltage reading at the near and far positions. Each time the Z-axis was adjusted, the X-Y positioners also had to be peaked, verifying that the beam was not straight down the axis.

A level, slightly diverging beam was obtained in this manner. The diameter of the beam was checked by noting at which aperture size the voltage dropped to 1/2 maximum. This yielded the half power beam width (HPBW). Beam leveling was checked by rocking the detector head forward

and backward while watching the scope, and using a small aperture opening. The beam was considered level if the output was maximum when the detector mount was upright. The beam obtained in this manner had a HPBW of 1 mm at the output of the bench rail and a HPBW of 2 mm at the edge of the mounting plate.

The beam splitter cubes were initially glued to machined aluminum discs which were fitted into the one inch holes in the optic bench and held with set screws. Azimuth adjustment was easy but tilting for beam leveling was not possible. The beamsplitters were then glued to standard prism holders, one of which could be tilted easily. The other one was only adjustable in azimuth and height. Tilt adjustment was achieved by loosening the adapter plate screws and tilting the whole assembly.

The power transmitted by a beamsplitter (BS) can be characterized by the power reflection coefficient (α_1) (Ref 25):

$$\text{Transmitted Power} = P_o(1 - \alpha_1)$$

$$\text{Reflected Power} = \alpha_1 P_o$$

These relations assume a lossless beamsplitter.

Relative voltage readings were obtained of the incident light into BS₂ (output BS) and the light transmitted and

reflected. Input was measured at 2.0 V, output was 0.4 V and the reflected value was 1.5 V. Since these do not add to 2.0 V, the beamsplitter is not lossless. A more reasonable number is the transmitted efficiency (and reflected efficiency), (E_{tx} and E_{ref}). These are calculated as:

$$E_{tx} = \frac{.4}{2.0} \times 100\% = 20\%$$

$$E_{ref} = \frac{1.5}{2.0} \times 100\% = 75\%$$

Indicating that about 5% of the light is lost in the beam-splitter. Also, at this value of I_{lsr} ~ 145 mA the beam-splitters are not 50/50 as desired. This fact proved to have a serious effect on total power lost in the system while operating incoherently.

Received power curves vs. I_{lsr} were obtained at the output of the beamsplitters, both with and without a polarizer. The result using a polarizer which was adjusted for maximum is Figure 4.13. The obtained P_{lsr} vs. I_{lsr} for the case without a polarizer is also plotted on this graph.

As expected, the curves agree at low values of I_{lsr} and values above I_{th} where the polarization is random and well defined respectively. What was unexpected was the fact

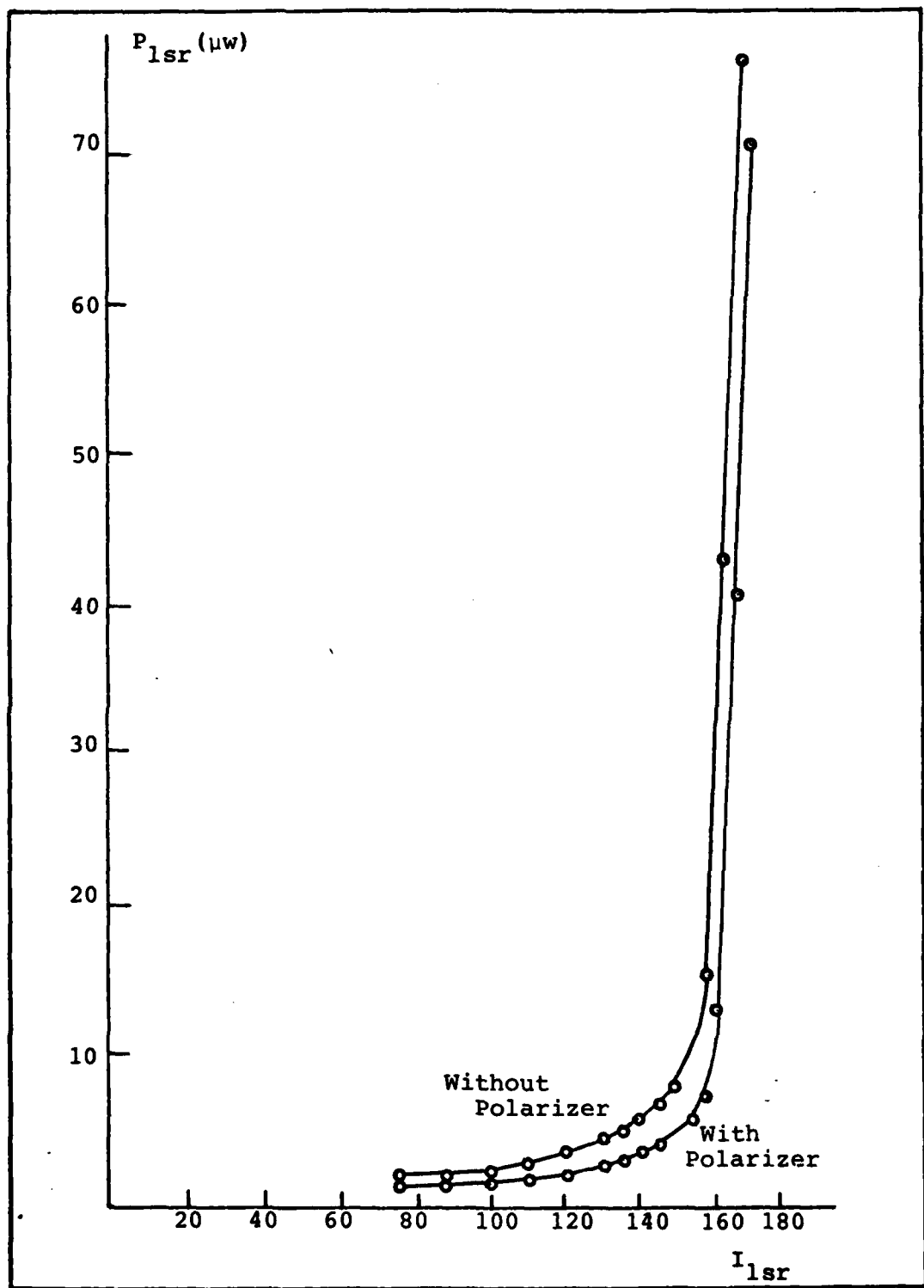


Figure 4.13 Laser Power Through Two Beamsplitters

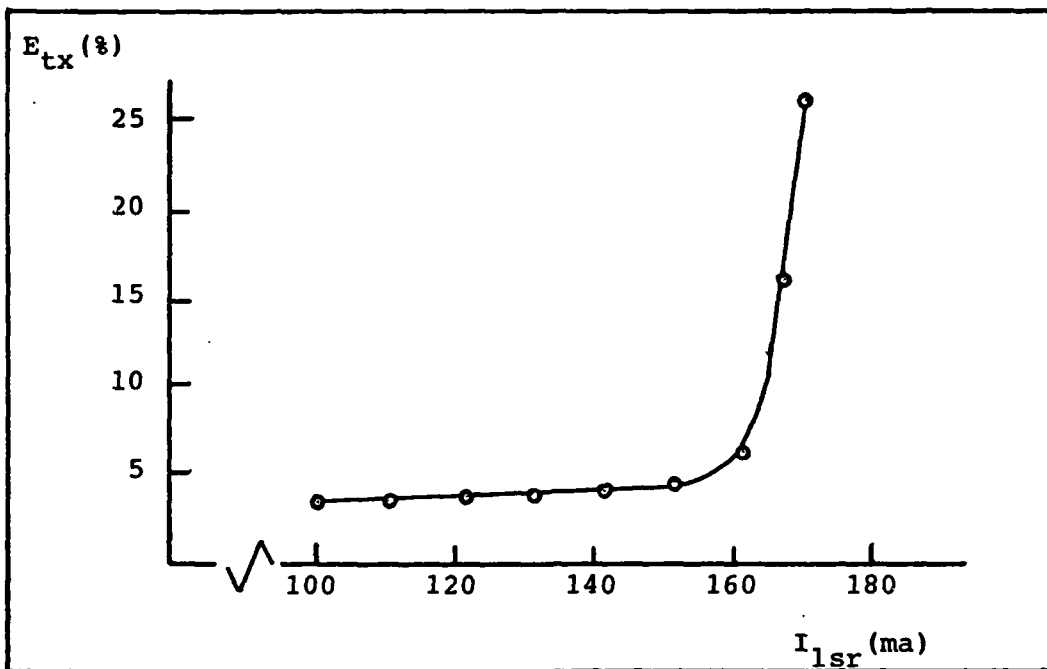


Figure 4.14 Beamsplitter Transmittance

that the total transmitted efficiency through the two beamsplitters, $(E_{tx})^2$, was not a constant. A comparison of Figure 4.10 and Figure 4.13 was used to plot the total system efficiency through the beamsplitters. A plot of this transmitted efficiency vs. I_{1sr} is given in Figure 4.14.

The beamsplitters obviously can transmit some states of polarization better than others. This is a common occurrence in beamsplitters cubes, such as these. When the light is randomly polarized, only about half of the light is in the preferred SOP. Thus, the normal 50% transmitted efficiency drops to ~ 20 to 25% as experienced.

The effect of the cube beamsplitters on the light available for the gyro can be seen by repeating the experiment of Figure 4.11, the evolution of polarization for various laser drive current. The results of Figure 4.15 were obtained in the same manner as previous, with light passing straight through the two beamsplitters.

The ratio of maximum to minimum detected voltage can be plotted as before and the DP's compared. Figure 4.16 shows the DP curves superimposed. After an initially lower degree of polarization, the curve with the beam-splitters shows a rapid increase in the evolution of polarized light. The operating point of the gyro should be set using this new curve for determining randomness of the polarization.

Acousto-Optics

The Coherent Associates acousto-optic (A/O) modulators were to be used in both versions of the fiber gyro and the beam deflection efficiency of this device was investigated.

The modulator was mounted on a baseplate of sufficient height to bring the aperture in line with the optic axis of the system. The power in the beam which could be passed through the apertures was monitored and the A/O was adjusted to allow the entire beam to pass.

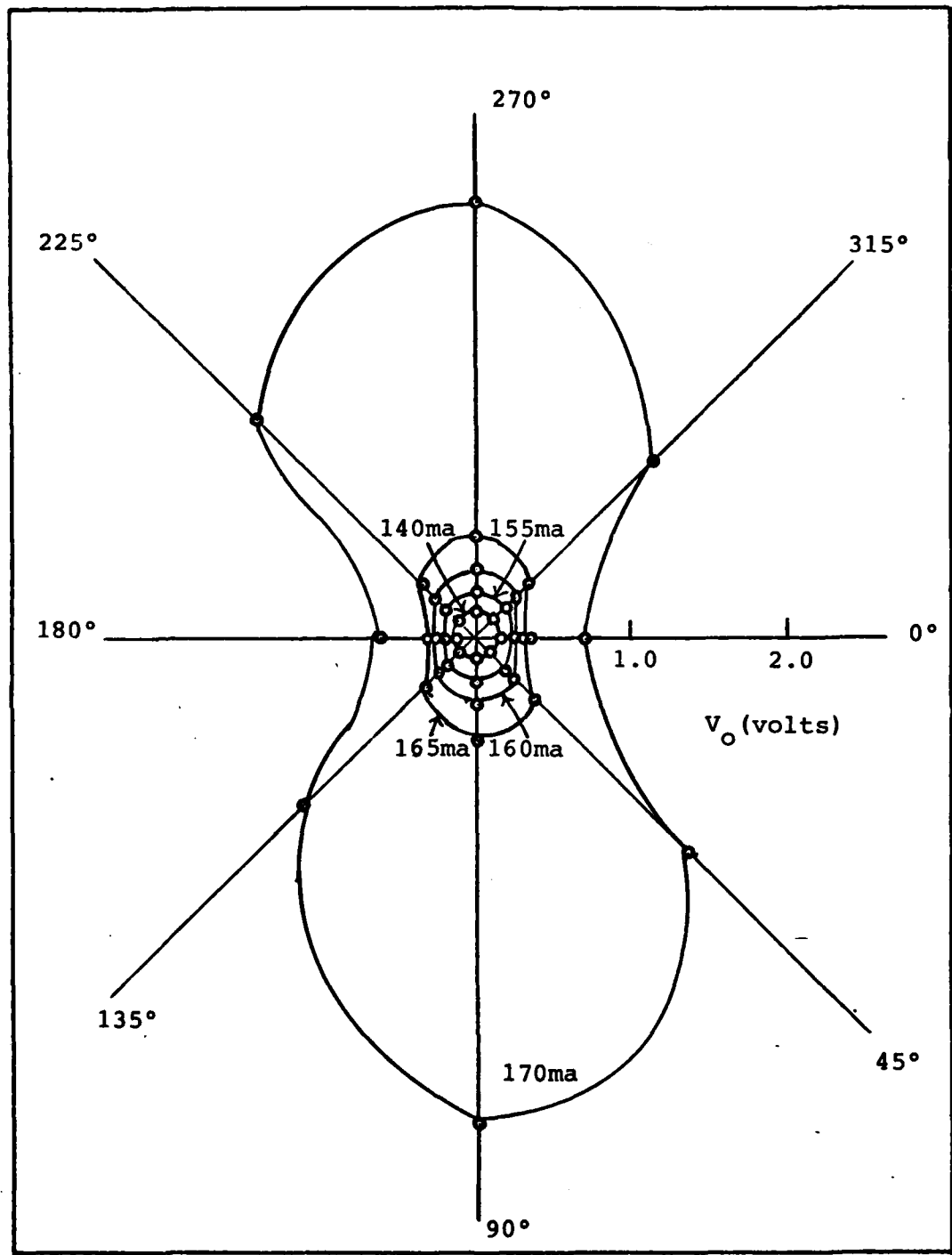


Figure 4.15 Evolution of Polarization With Beamsplitters

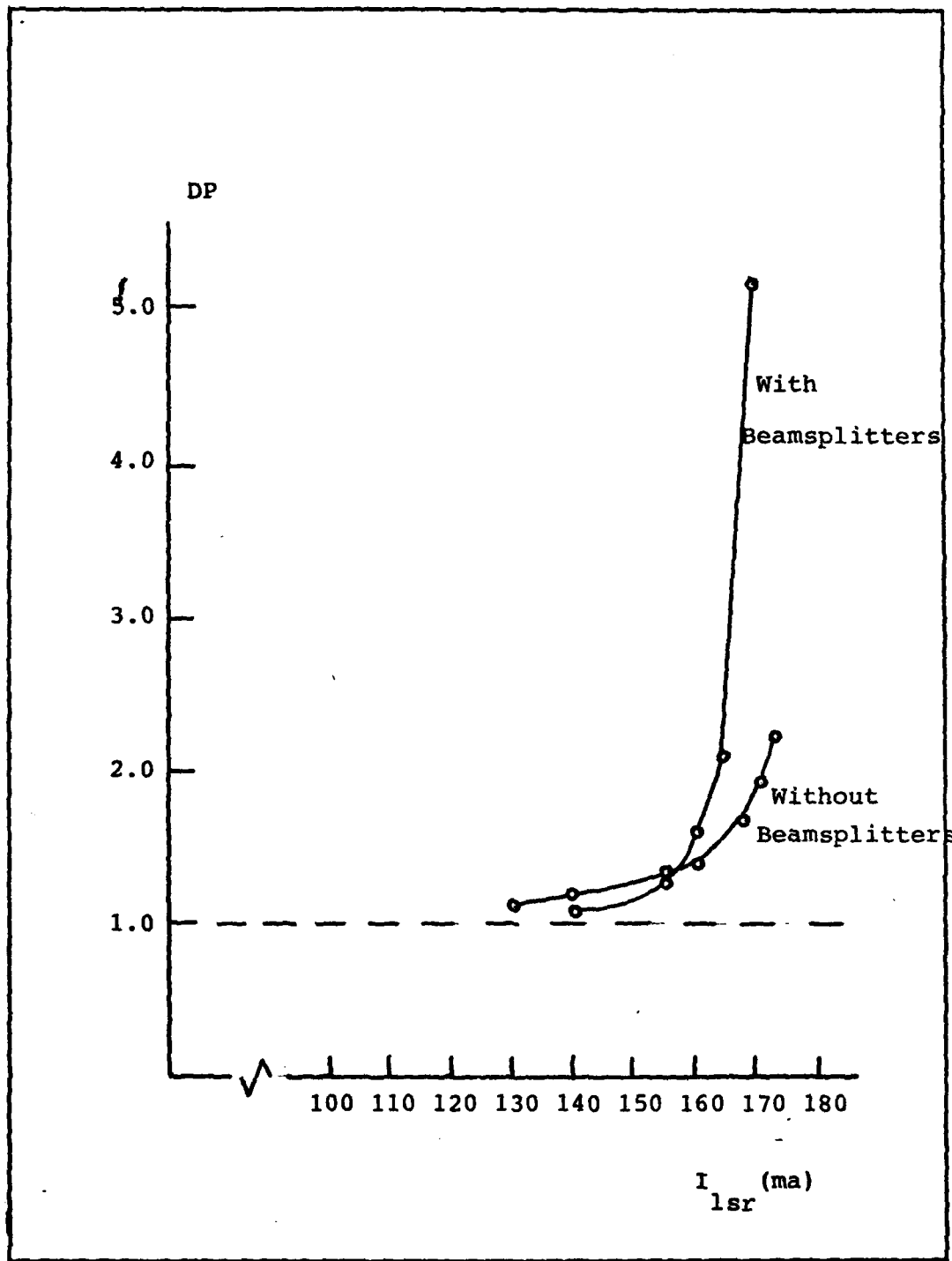


Figure 4.16 Effect of Beamsplitters on DP

A 28 V p-p, 40 mHz radio frequency signal was then applied to the A/O while observing this 0th order output. Usually, a noticeable dip in the detector voltage was observed. The A/O could then be turned carefully to maximize this dip. The point at which the V_0 was minimum without getting aperture blocking due to A/O windows is the Bragg angle. See Appendix D for a brief discussion of this device and its' design considerations. The detector/aperture could then be moved to one side to observe the deflected first order beam and a fine adjustment to the A/O angle could be made by peaking this signal. By adjusting the aperture on the detector small enough, a zero reading could be obtained when the rf power was removed, yielding a good estimate of the amount of power deflected into the first order.

The efficiency of the A/O diffraction to first order was found in this manner. In all cases, this efficiency was found to be less than 30 percent and usually was closer to 20 percent.

Yariv (Ref 50) (See Appendix D) has given an equation for diffraction efficiency as a function of wavelength, interaction length, material and acoustic power.

$$\frac{I_{\text{diff}}}{I_{\text{incident}}} = \sin^2(1.4 \frac{0.6328}{\lambda} \sqrt{\frac{M_w}{I_{\text{acoustic}}}})$$

Where

λ = light wavelength (in mm)

l = acoustic column length (in mm)

M_w = diffraction figure of merit of material
relation to water

$I_{acoustic}$ = acoustic intensity (watts)

For these modulators $M_w = .12$, $l = 2$ mm, and $I_{acoustic}$
is some fraction of the applied rf power. If $I_{acoustic} = .9$
(rf power), then it is $(.9)(2.0\text{ W}) = 1.8$ Watts. Thus
using these numbers:

$$\frac{I_{diff}}{I_{incident}} = \sin^2(1.4) \frac{0.638}{0.84} (2) \sqrt{.12(1.8)} \\ = .697$$

for an efficiency of ~70%.

For a value of $I_{acoustic} = .65$ (rf power).

$$\frac{I_{diff}}{I_{incident}} = .548 \text{ or } 55\%$$

The value of .65 was found by solving the equation using
a HeNe laser as an example and using the advertised
specification of 80% efficiency for HeNe at 2 watts of
rf power.

Normal operation of the modulator should have yielded a deflection efficiency of at least 55%, assuming the beam was completely interacting with the acoustic column. As is pointed out in Appendix D, the efficiency is also a function of the ratio of the acoustic beam divergence to the light beam divergence (Ref 50, 52). This was considered the most likely reason for the observed low efficiency since at this time the beam was known to be diverging slightly, (see previous section).

At this point, the system was ready for investigation of the fiber losses and alignment produces.

Fibers

The fiber to be used in the gyro was a single mode step-index type. The core has a diameter of about 6 μm , a cladding diameter of 111 μm , with an additional plastic coating of 200 μm . The fiber was mounted in a Newport Research Corporation X-Y-Z positioner which was mounted in an aluminum block containing a 10X microscope objective. The microscope objective was used to focus the beam onto the core, improving the coupling efficiency.

Once the acousto-optic modulator had been aligned for maximum efficiency of deflection into the first order beam, the microscope/fiber positioner mount could be aligned.

First, the mount was aligned with the fiber positioner removed and the detector mounted in its place. The system could be adjusted for a peak reading of the first order beam. This assured that the first order, which was the one of interest was passing completely through the center of the optical axis of the M/O. Because of the small separation angle between the 0th and first order beams, and the close proximity of the M/O to the output of the acousto-optic, both beams passed easily through.

In order to ease alignment, a short piece of multimode fiber was prepared and placed in the fiber positioner, with the free end of the fiber placed in the detector aperture. With the laser operating at 164 mA, a peak was found quite easily using this fiber with its relatively large (50 - 100 μm) core. Once the alignment had been achieved by successive tweaking of the X, Y and Z axes until no improvement could be made, the fiber holder rod was removed. This could be done without disturbing the X-Y position. A short piece of single mode fiber was prepared and then inserted, being careful to orient the fiber holder rod exactly as before. After a couple of attempts, a peak was found indicating the beam was focused onto the fiber end.

The above alignment was performed with the rf drive to the acousto-optic modulator turned off, since the higher power 0th order beam was easier to align to. Once alignment was obtained, the rf was turned on, and the fiber could be

AD-A115 477 AIR FORCE INST OF TECH WRIGHT-PATTERSON AFB OH SCHOOL--ETC F/G 20/6
DESIGN CONSIDERATIONS FOR AN INCOHERENT FIBER OPTIC GYROSCOPE. (U)
DEC 81 R L ICE
UNCLASSIFIED AFIT/GE/EE/81D-29 NL

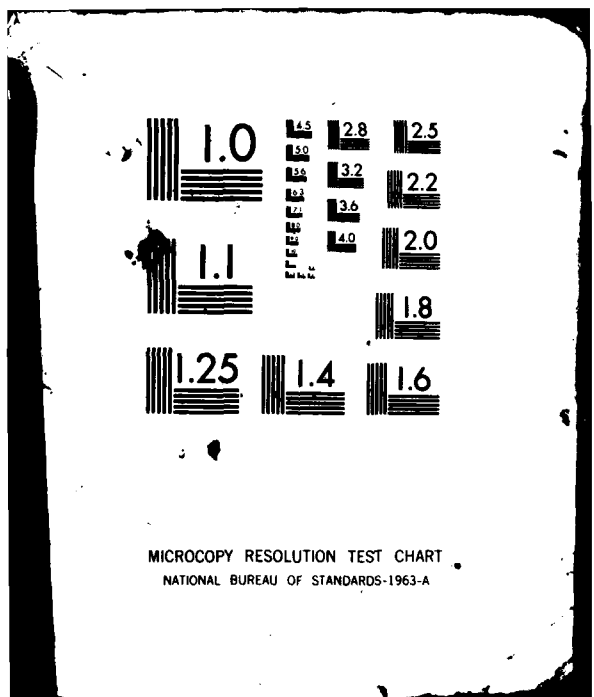
2-2

2-2

2-2



END
DATE FILMED
7 82
DTIC



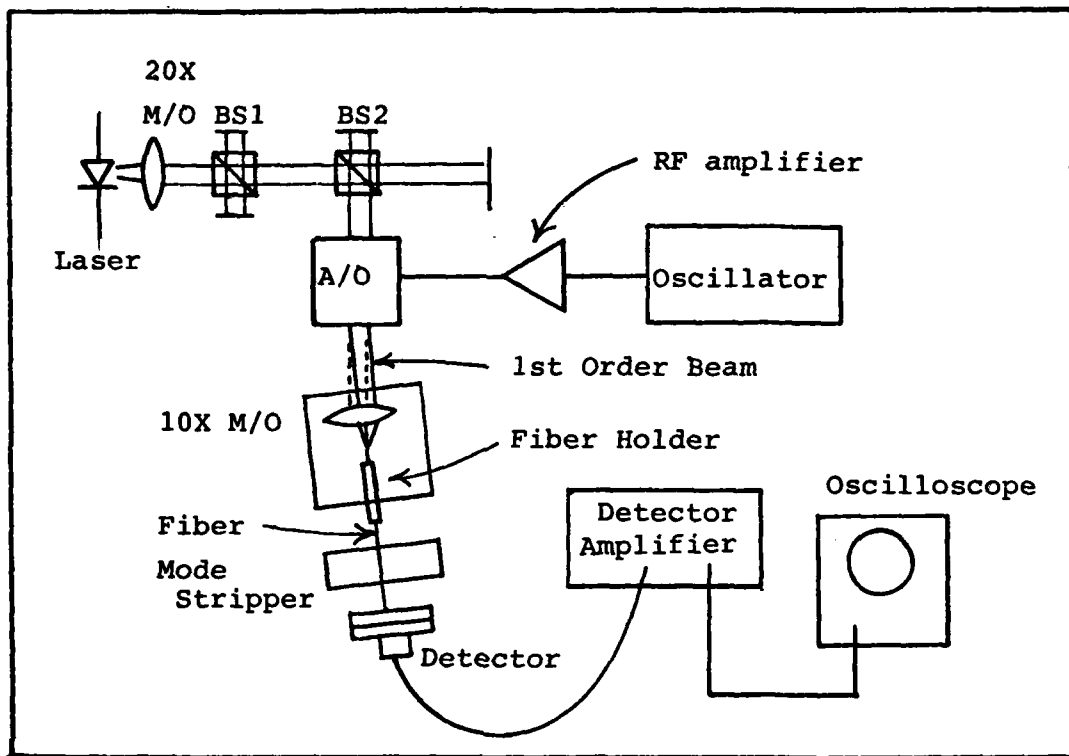


Figure 4.17 Partially Constructed Gyro

adjusted slightly to the side to peak on the first order beam.

The layout of the system at this time can be seen in Figure 4.17 showing the progress of construction of the fiber gyro at this point. The single mode fiber was supported by a microscope slide mounted on a block. The glass slide served as an effective mode stripper when a drop in index matching fluid was dropped onto the fiber as it rested on the slide.

The peak reading at the detector output of the first order beam was 330 nW. When the index fluid was applied, output intensity fell to only 170 nW indicating the amount of power in the first order mode that was actually propagating down the core.

At this time a calculation of the coupling loss measured into this short section of fiber was made. The net transmission in the beamsplitters was $0.25 \times 0.95 = .238$ (since there was one transmission and one reflection, net loss was .25 minus the known loss of 5%). The expected loss in the 10X microscope objective was about 20% based on the result obtained with the lasers 20X M/O. The acousto-optic modulator efficiency to first order was only 20%. At $I_{laser} = 164$ mA the plot of Figure 4.8 yields a power out of the laser M/O of 260 μ W. The expected power available to couple into the core of the fiber was thus:

$$\text{Power avail.} = (260 \mu\text{W}) (.238) (.2) (.8) = 9.9 \mu\text{W}$$

The power observed with this piece of fiber was 0.170 μ W so the coupling efficiency was:

$$\text{Efficiency} = \frac{0.17}{9.9} \times 100 = 1.7\%$$

Another piece of multimode fiber was inserted and data was taken of power versus I_{1sr} for the 0th and the first order modes. This was done to get a clearer picture of what the A/O diffraction efficiency was since the core of the multimode fiber acted as a more effective aperture than the one on the detector. The fiber effectively separated the two beams so the actual power being diverted into the first order could be measured. Also it was observed that the modes were being confined effectively to the core since the addition of index fluid resulted in no visible drop in the output. The curves of 0th and first order power are presented in Figure 4.18. From these curves a plot of deflection efficiency to first order as a function of I_{1sr} was generated. Figure 4.19 shows the calculated efficiencies. Within the realm of experimental error, no effect of I_{1sr} on efficiency was seen. This was expected since the efficiency equation contains no incident light power terms. The perceived fluctuations were considered due to measurement error. The average value of efficiency over the entire range (ignoring the low point at $I_{1sr} = 180$ mA) was 23.125% so a value of 23% will be used for any further calculations of A/O efficiency.

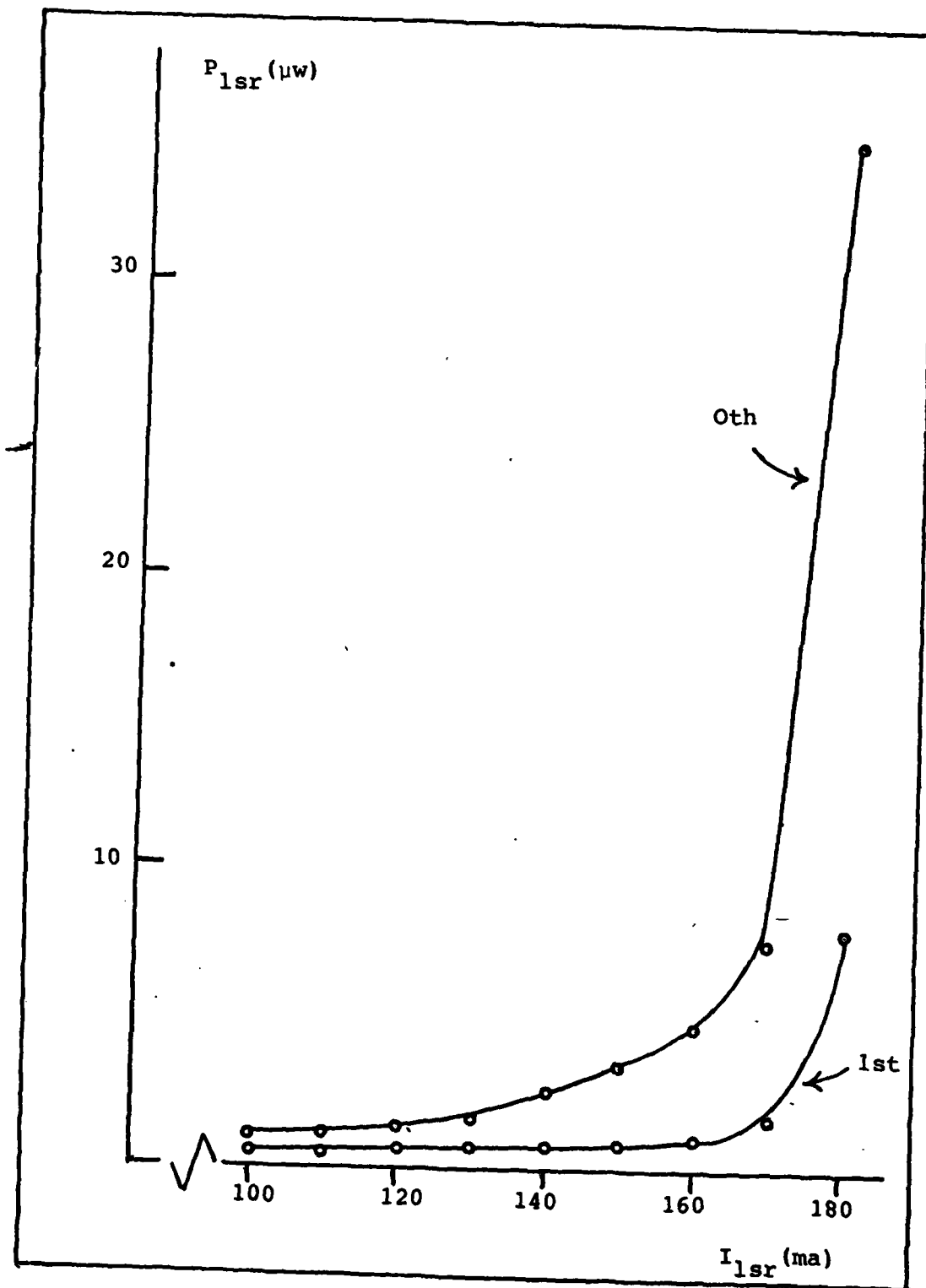


Figure 4.18 Oth and 1st Order Modes, (Multi-mode Fiber)

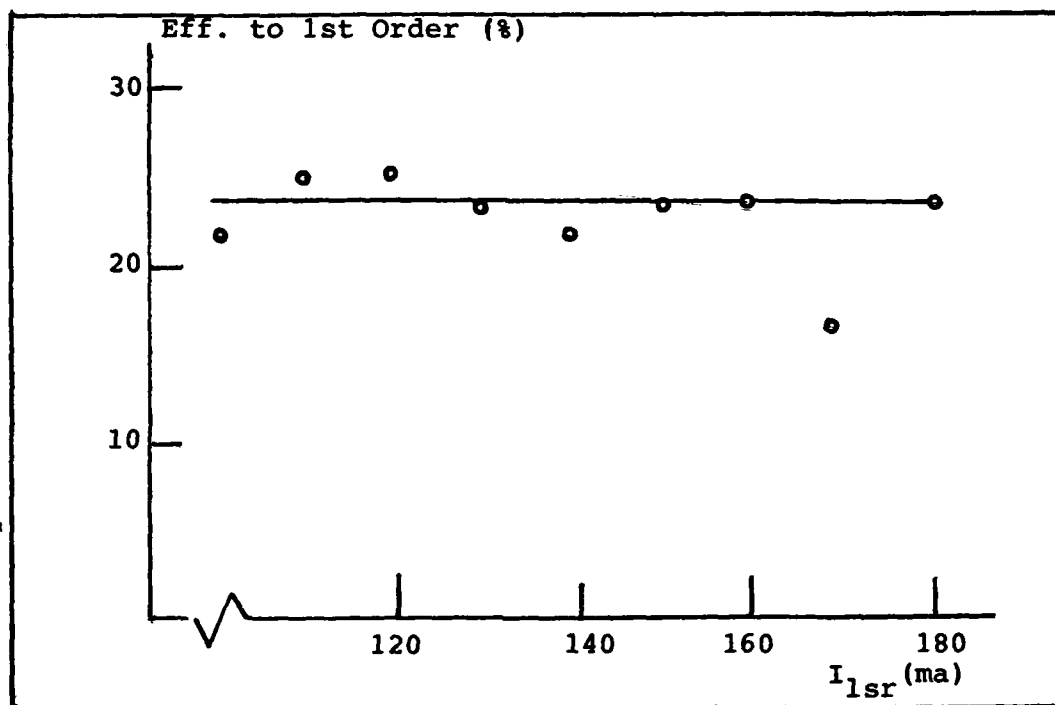


Figure 4.19 A/O Efficiency

After much difficulty, another short piece of single mode fiber was prepared and aligned. A curve of the power in the 0th order is presented in Figure 4.20. Measurements at this point became difficult due to the high level of noise at the detector output. Peak-to-peak noise was about 0.1 V while the output at $I_{lsr} = 100$ mA was only 0.14 V. The high noise level was a consequence of the high detector gain required at this point.

One final test was attempted. The 15 m main coil of single mode fiber was prepared and mounted on the gyro baseplate. One end of the fiber was inserted into the

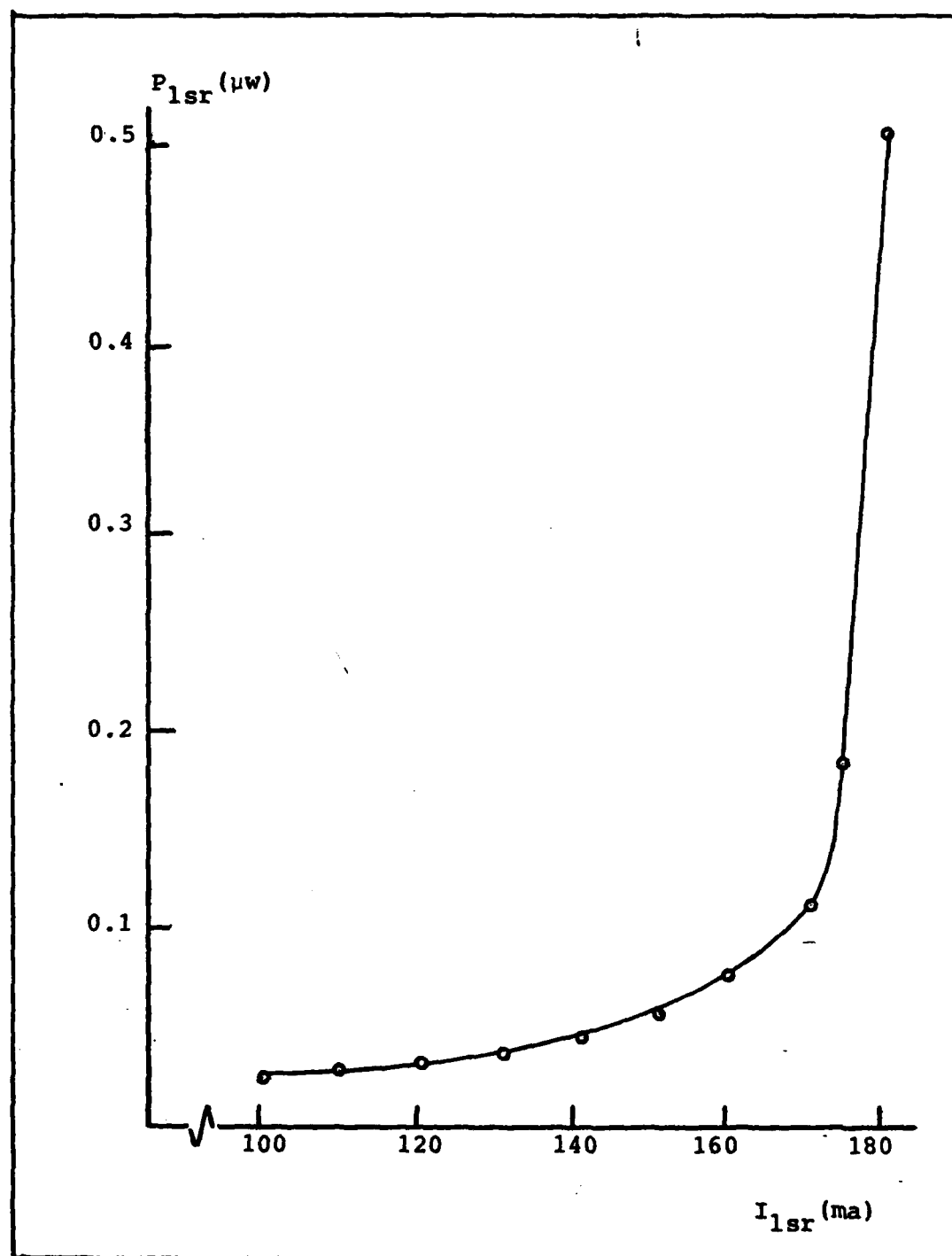


Figure 4.20 0th Order Mode Through a Single-Mode Fiber

positioner and the other end into the detector aperture. After much careful tweaking, a 0th order peak was found, but only intermittently. The fiber, with its plastic jacket removed was not being held firmly in the mount and alignment could not be maintained. The transient peak observed, however, was 0.5 V which corresponds to about 83 nW. The laser was operating at 180 mA at this time. With the multimode fiber, 34.65 μ W was coupled out. The relative efficiency of the 15 m single mode fiber vs. the multimode was $.083/34.65 \times 100 = .24\%$, a drastic power reduction. Efficient coupling into the single mode fiber was not achieved.

V. Component Contributions to Error

The Critical Components

During the course of this investigation the major contributing components to the gyro error are determined. The critical components are the light source, the collimating and coupling optics, and the acousto-optic modulator. The problems associated with each component are as follows (Ref 53).

Laser Diode

- fluctuations in drive power
- wavelength changes
- mode stability

Optics

- beam quality
- misalignment
- fiber coupling efficiency
- losses

Acousto-optics

- change in RF drive power
- acoustic wavelength variation
- temperature gradients
- deflection angle

All of these sources of error can contribute to gyro error. Table 5.1 which is adapted from (Ref 53) shows the error sources as they affect gyro performance. An "X" in the table indicates that the component contributes to gyro error.

As seen in the table, most of the components contribute a bias drift due mostly to fluctuations in the signal power. The problems due to the laser diode should be reduced somewhat for the noncoherent gyro since the intention is not to operate the laser in a single mode.

Component Performance	Laser Diode	A/O	Fiber Couplers			
	Mode Shape λ	Polarization	Thermal Gradients	Deflection Angle	Back Scat. & Angle	Chg. Reflec. Pos.
Bias Drift						
-long term						
-short term	X	X	X	X	X	X
-repeatability						
Scale Factor						
-linearity						
-asymmetry	X	X				
-repeatability						
-stability						
Maximum Rate						
				X		X

Table 5.1 Component Characteristics vs. Performance

It is assumed that incoherent operation (or use of an LED) will eliminate all source errors except for intensity fluctuations. Any change in the source output intensity can be nulled out by using a detector to monitor the diode output, and controlling the drive current to the device through an appropriate feedback network.

Likewise, there should be no polarization problems since as demonstrated in Chapter IV, a suitable source can be chosen which can be operated with random polarization. Any fluctuations in the polarization are evenly distributed over all states and are unobservable.

The major remaining error sources are the acousto-optic modulator and the collimating and fiber coupling optics.

Coupling Optics

The tasks associated with coupling are 1) collimating the beam from the light source, 2) alignment of beamsplitters, 3) coupling into the acousto-optic, 4) coupling into the fiber and then recollimating the beam at the output. The problems involved with these tasks are: achieving good power transfer efficiencies, achieving and maintaining alignment conditions, and avoiding scattered or reflected light. The last item is not a serious problem and any aspects of it can be avoided by careful design and use of anti-reflection coated optics. The major power transfer

problems occur with the beam splitters and the acousto-optic device. The beam splitters do not exhibit 50/50 splitting for the randomly polarized light and prove to be a major source of power loss. Coupling into the face of the fiber, even though a focusing lens is used, is an even more serious problem. Observed coupling efficiencies are of the order of one percent or lower.

The fiber coupling efficiency is given by, (Ref 53)

$$E_{fc} = \left(\frac{2w_0 w_1}{w_0^2 + w_1^2} \right)^2$$

for the case of maximum efficiency, when the displacement of the focused beam off the core (X_0) is zero, and the angular deviation from the correct entrance angle (θ) is zero.

w_0 is the fiber beam waist and is given by

$$w_0 = \frac{d}{2} [.65 + 1.619 \left(\frac{\pi (NA) d}{\lambda} \right)^{3/2} + 2.879 \left(\frac{\pi (NA) d}{\lambda} \right)^6]$$

when d is the core diameter and NA is the numerical aperture of the fiber.

w_1 is the focused beam waist and is given by

$$w_1 = \frac{2.44\lambda FL}{2D} \left(\frac{2}{3} \right)$$

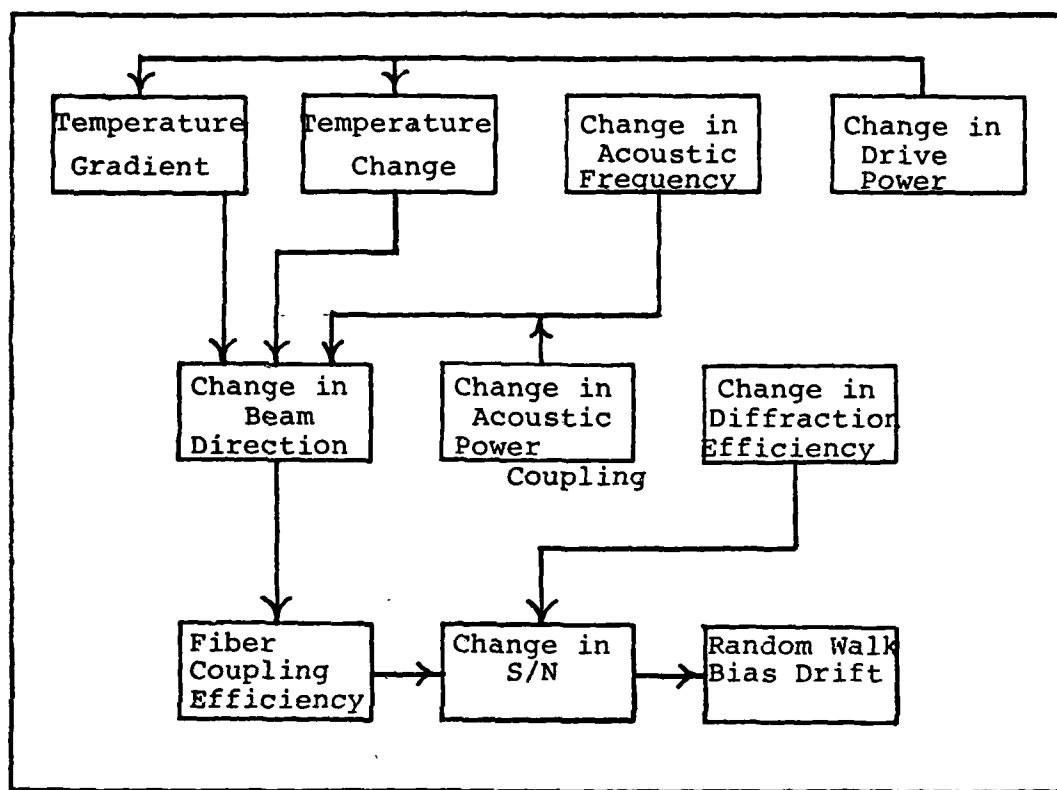


Figure 5.1 A/O Error Sources

Where FL is the focal length of the lens used and D is the initial collimated beam diameter.

Acousto-optic Modulator

There are several operational problems that can occur for the A/O besides low diffraction efficiency into the first order. Any change in this efficiency, whether due to thermal instabilities, changes in RF drive power, or changes in the driving frequency, can affect output bias drift.

Figure 5.1 shows a flow chart that relates errors that are due to the A/O (Ref 53).

A conclusion which can be drawn from Figure 5.1 is that any fluctuations in the temperature or drive power/frequency must be minimized. In addition, the diffraction efficiency is dependent on wavelength and degree of beam collimation, i.e., changes in the collimating optics can affect output S/N ratio via the acousto-optic modulator.

Changes in the acoustic wavelength (Λ) directly affect the beam direction since this is determined by the Bragg angle which is given by

$$\sin\theta_B = \frac{f}{2\Lambda}$$

and changes in the beam direction seriously impact the fiber coupling.

Summary of Major Error Source in the Incoherent Fiber Gyro

The anticipated serious error sources for the incoherent gyro are 1) beam collimation and stability, 2) mechanical stability of the coupling optics, 3) the acousto-optic modulator, 4) mechanical stability of the fiber coupling. If an appropriate source which exhibits incoherence and random polarization while supplying adequate power can be found, it is not expected to be a major contribution to the error.

VI. Conclusions and Recommendations

The goal of this project is to determine the component qualities needed to build an incoherent fiber optic gyroscope. Several potential light sources are investigated and one laser diode in particular is characterized. It is concluded that such a diode can be operated in the incoherent mode but its subsequent low power output is a problem.

The other components added to the low power problem. The beamsplitters are found to not yield a 50/50 split for the randomly polarized light. The efficiency of the acousto-optic modulator is much less than the ideal calculated efficiency due to beam collimation problems. In spite of these problems, a detectable amount of power is coupled through a 15 meter length of single mode fiber (83 nW). However, this requires operation of the laser above threshold. A further refinement in the detector amplifier design may have allowed detection of an even lower signal power.

Many of the problems associated with the fiber such as polarization, degradation and backscatter noise may probably be reduced. The reduction of backscatter by using the shorter coherence length source has been demonstrated in the literature (Ref 7, 41). The operation of at least one randomly polarized fiber gyro has been reported, (Ref 6) indicating that polarization control elements may soon be

unnecessary. The incoherent fiber gyro promises to be significantly less complex than current, high sensitivity fiber gyro.

The problems associated with the optics (lenses, beam-splitters, fiber coupling) can be almost eliminated through the use of presently available and emerging technology. The cube beamsplitters can be replaced by evanescent couplers (Ref 7, 39). Various approaches to the beam collimation problems are also available. A short section of fiber may be butted against the face of the laser (or LED) and the output of the fiber can be collimated with a lens if needed. The use of Graded Index Lenses (GRINS) has recently been proposed (Ref 53). These are basically large diameter gradient index multimode fiber.

The LED is an attractive alternative source to use because of its high incoherent power output and wide linewidth. One device is tested which yields up to 3 mW but difficulties in collimating its output are encountered. Alternate means of using the output of this device should be investigated. It is noted, that even with an aperture for reducing the beam diameter, power comparable to that of the laser diode is available. Another possibility is to focus the LED beam at some point in the system, perhaps in the center of the acousto-optic modulator,

through the use of lenses. There are many other types of LED's available due to the recent advances in optical communications (Ref 8). Both the Burrus type surface-emitter and the edge-emitter diodes can be fabricated with small source sizes suitable for coupling to fibers. They promise to have better linearity and less sensitivity to gradual degradation than the diode laser.

Two signal processing plans are also presented. One is an open loop system employing a frequency shift of one of the beams in the coil to introduce the non-reciprocal phase shift. This can be used to increase sensitivity at low rotation rates. The second employs a closed-loop, frequency nulling technique which promises to provide a linear output over a wide dynamic range. An investigation of the relative advantages/disadvantages of these two plans can be an excellent topic for further thesis research.

An alternative to the discrete optical component approach is to use integrated optics (Ref 15). This emerging technology has great potential in the field of rotation sensing. Recently an all waveguide configuration was proposed (Ref 17) which is considered buildable. It is basically a hybrid approach where all optical elements can be constructed using integrated optics chips, including the modulator and phase bias elements. The waveguide coupler and phase bias elements were constructed and tested.

A recent study (Ref 53) made several recommendations and those that are applicable to the incoherent fiber gyro are repeated here.

Laser Diode (or LED)

- feedback to stabilize the output power
- packaging to allow solid block construction and beam collimation
- selection of linewidth to minimize backscatter noises

Acousto-optic Modulator

- heat sinking to avoid thermal problems
- use of a different crystal material to improve maximum efficiency (tellurium dioxide)
- optimum matching of acoustic beam size and shape to optical beam

Fiber Coupler and Collimating Optics

- solid block construction
- use of graded index lenses
- mode stripping and index matching
- rigid potting of the fiber ends in index matched epoxy

With most of these recommendations taken into account, it should be possible to construct an inertial grade, incoherent fiber gyro.

Bibliography

1. Anderson, D.B. "Integrated Optical Spectrum Analyzer: an Imminent 'Chip,'" IEEE Spectrum, (Dec. 1978).
2. Anthony, P.J., et al. "Reliability of 0.87 micron (AlGa)As Double Heterostructure Lasers with Ga(As,Sb) Active Lasers," IEEE Electron Device Letters, EDL-2, (Feb. 1981).
3. Aronowitz F. "The Laser Gyro," Laser Applications, Volume 1. Boston: Academic Press, Inc. 1971.
4. Bergh, R.A., H.C. Lefevre, and H.J. Shaw. "All-Single-Mode Fiber-Optic Gyroscope," Optics Letters, 6 (4): 198 (April 1981).
5. Billings, B.H. "A Monochromatic Depolarizer," Journal of the Optical Society of America, 41, 966 (Dec. 1951).
6. Bohm, K., P. Marten, K. Petermann, E. Weidel, and R. Ulrich. "Low Drift Fibre Gyro by Using a Depolarizer and a Superluminescent Diode," Instrumentation Conference, Paper No. TUL 7-1, San Francisco, California (May 1981).
7. Bohm, K., P. Russer, E. Weidel and R. Ulrich. "Low-Noise Fiber Optic Rotation Sensing," Optics Letters, 6 (2): 64 (Feb. 1981).
8. Botez, D. and G. Herskowitz. "Components for Optical Communications Systems," Proceedings IEEE, 68 (6): (June 1980).
9. Cahill, R. F. and E. Udd. "Phase-Nulling Fiber-Optics Laser Gyro," Optics Letters, 4 (3) (March 1979)
10. Chang, I.C. "Acoustooptic Devices and Applications," IEEE Transactions on Sonics and Ultrasonics, SU-23 (1): 2 (Jan. 1976).
11. Chinone, N. and R. Ulrich. "Elasto-optic Polarization Measurement in Optical Fiber," Optics Letters, 6 (1): 16: (Jan. 1981).
12. Cutler, C. C., S. A. Newton and H. J. Shaw. "Limitations of Rotation Sensing by Scattering," Optics Letters, 5 (11): 488: (Nov. 1980).

13. Davis, J. L. and S. Ezekiel. "Techniques for Shot-Noise-Limited Inertial, Rotation Measurement Using a Multiturn Fiber Sagnac Interferometer," SPIE, 157 131: (1978).
14. Ezekiel S. and S. Balsamo. "Passive Ring Resonator Laser Gyroscope," Applied Physics Letters, 30 (9): 478 (May 1977).
15. Garmire, E. "Optical Waveguides for Laser Gyro Applications," SPIE, 157: 95 (1978)
16. Gordon, E. I. "A Review of Acousto-optical Deflection and Modulation Devices," Proceedings IEE, 54 (10): (Oct. 1966).
17. Goss, W. C., R. Goldstein, M. Nelson, H. Fearnehaugh and O. Ramer. "Fiber Optic Rotation Sensor Technology," Applied Optics, 19 (6): 82 (March 1980).
18. Jacobs, I. and S. Miller. "Optical Transmission of Voice and Data," IEEE Spectrum, (Feb. 1977).
19. Johnson, M. "In-line Fiber-optical Polarization Transformer," Applied Optics, 18 (9): 1288 (May 1979).
20. Kintner, E. C. "Polarization Control in Optical-Fiber Gyroscopes," Optics Letters, 6 (3): 154 (March 1981).
21. Klein, W. R. and B. D. Cook. "Unified Approach to Ultrasonic Light Diffraction," IEEE Transactions Sonics and Ultrasonics, SU-14: 123 (July 1967).
22. Korpel, A. "Acousto-Optics - A Review of the Fundamentals," Proceedings IEEE, 69 (1): 48 (Jan. 1, 1981).
23. Kressel, H. "Room Temperature CW Laser Diodes - An Overview," Paper WC 1-1, Integrated Optics Topical Meeting, (Jan. 12-14, 1976).
24. Kressel, H., I. Ladany, M. Ellenberg, and H. Lockwood. "Light Sources," Physics Today (May 1976).
25. Lin, S. C. and T. G. Gralorenzi. "Sensitivity Analysis of the Sagnac Effect, Optical Fiber, Ring Interferometer," NRL Report 8250, (Nov. 16, 1978).

26. Marcuse, D. Principles of Quantum Electronics. Boston: Academic Press, Inc. 1980.
27. McLandrich, M. N. and H. E. Rast. "Fiber Interferometer Gyroscope," SPIE, 157 (127): (1978).
28. Melman, P. and W. J. Carlsen. "Interferometric Measurement of Time-Varying Longitudinal Cavity Modes in GaAs Diode Lasers," Applied Optics, 20 (15): 2694 (Aug. 1981).
29. Panish, M.B. "Heterostructure Injection Lasers," Proceedings IEEE, 65: (Oct. 1977).
30. Post, E. J. "Sagnac Effect," Reviews of Modern Physics, 39 (2): (April 1967).
31. Preston, E. J. "Pressure Sensing With Fiber Optics and Interferometry." MS Thesis, Wright-Patterson AFB, Ohio: Air Force Institute of Technology, December 1980.
32. Rashleigh, S. C. and W. K. Burns. "Dual-Input Fiber-Optic Gyroscope," Optics Letters, 5 (11): 482 (Nov. 1980).
33. Rashleigh, S. C. and R. Ulrich. "Polarization Mode Dispersion in Single-Mode Fibers," Optics Letters, 3 (2): 60 (Aug. 1978).
34. Rashleigh, S.C. and R. Ulrich. "High Birefringence in Tension-Coiled Single-Mode Fibers," Optics Letters, 5 (8): 354 (Aug. 1980).
35. Resinger, A. R., C. D. David, Jr., K. L. Lawley and A. Yariv. "Coherence of a Room-Temperature CW GaAs/GaAlAs Injection Laser," IEEE Journal of Quantum Electronics, QE-15 (12): (Dec. 1979).
36. Schiffner, G., W. Leeb, H. Krammer, and J. Wittmann. "Reciprocity of Birefringent Single-Mode Fibers for Optical Gyros," Applied Optics, 18 (13): 2096 (July 1979).
37. Shupe, D. M. "Fiber Resonator Gyroscope: Sensitivity and Thermal Nonreciprocity," Applied Optics, 20 (2): 286 (Jan. 1981).
38. Smith, A. M. "Polarization and Magneto Optic Properties of Single Mode Optical Fiber," Applied Optics, 17 (1): 52 (Jan. 1978).

39. Stillwell, J. W. "A Feasibility Study of Single Mode Fiber Optic Evanescent Field Coupling." MS Thesis, Naval Post Graduate School, C. S. Draper Lab Report #T694, June 1979.
40. Stowell, W. K. "Air Force Applications of Optical Rotation Rate Sensors," SPIE, 157: 167 (1978).
41. Thompson, D. E., D. B. Anderson, S. K. Yao, and B. R. Youmans. "Sagnac Fiber-Ring Interferometer Gyro with Electronic Phase Sensing Using a (GaAl)As Laser," Applied Physics Letters, 33 (11): 940 (Dec. 1978).
42. Thompson, G. H. B. Physics of Semiconductor Laser Devices. John Wiley and Sons, 1980.
43. Ulrich, R. "Fiber-Optic Rotation Sensing With Low Drift," Optics Letters, 5 (5): 173 (May 1980).
44. Ulrich, R. and M. Johnson. "Fiber-Ring Interferometer: Polarization Analysis," Optics Letters, 14 (5): 152 (May 1979).
45. Ulrich, R., S. C. Rashleigh, and W. Eickoff. "Bending-Induced Birefringence in Single-Mode Fibers," Optics Letters, 5 (6): 273 (June 1980).
46. Ulrich, R. and A. Simon. "Polarization Optics of Twisted Single Mode Fibers," Applied Optics, 18 (13): 2241 (July 1979).
47. Vali, V. and R. Shorthill. "Fiber Ring Interferometer," Applied Optics, 15 (5): 1099 (May 1976).
48. Vali, V. and R. Shorthill. "Ring Interferometer 950 m long," Applied Optics, 16 (2): 290 (Feb. 1977).
49. Williamson, T. L. and D. A. Willie. "Passive Fiber Optic Gyro Study," AFAL-TR-79-1197, (Oct. 1979).
50. Yariv, A. Introduction to Optical Electronics. 2nd Ed., Holt, Rinehart and Winston, 1976.
51. Yen, Y. and R. Ulrich. "Birefringence Measurement of Fiber Optic Devices," Applied Optics, 20 (15): 2721 (Aug. 1981).

52. Young, E. H. and S. Yao. "Design Considerations for Acousto-Optic Devices," Proceedings IEEE, 69 (1): 54 (Jan. 1981).
53. "Components for Passive Fiber Optic Gyros," Draft Report on Contract F33615-80-C-1025, McDonnell Douglas Astronautics Company, April 1981.
54. United Detector Technology Specifications for PIN 10, PIN 6, PIN 6D Detectors, 2644 30th Street, Santa Monica, California 90405.
55. Microbench Catalog, Spindler and Hoyer, Göttingen, Federal Republic of Germany

Appendix A. Semiconductor Lasers

Introduction

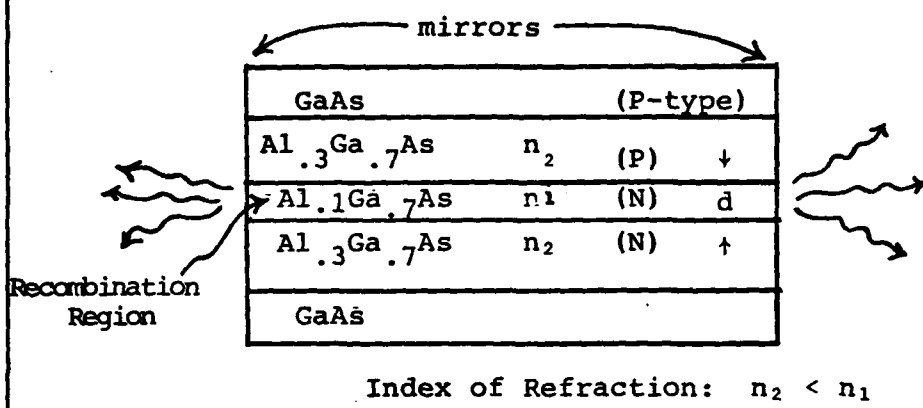
The operation of the semiconductor laser is very similar to that of the conventional laser. In such a "normal" laser energy is pumped by various means into the gain medium which results in the generation of photons. For lasing action to occur, these photons must be confined in a resonant cavity in such a manner that losses are overcome and light amplification occurs. This resonant cavity is typically comprised of two parallel mirrors, the so-called Fabry-Perot cavity. The semiconductor laser also makes use of such a cavity but the pumping action and photon emission occur in different ways. Stimulated emission occurs in the semiconductor laser as a result of transitions between energy states in the conduction and valence bands of the material, and not between isolated atomic levels. This is known as electron-hole recombination. The pumping method is due to carrier injection across a p-n junction. This injection is caused by the band gap differences in the semiconductor alloys on the two sides of the junction.

While there are many different types of laser diodes being developed, out of just as many kinds of materials, this paper will focus on one type. The double hetero-junction, stripe contact laser, fabricated out of AlGaAs,

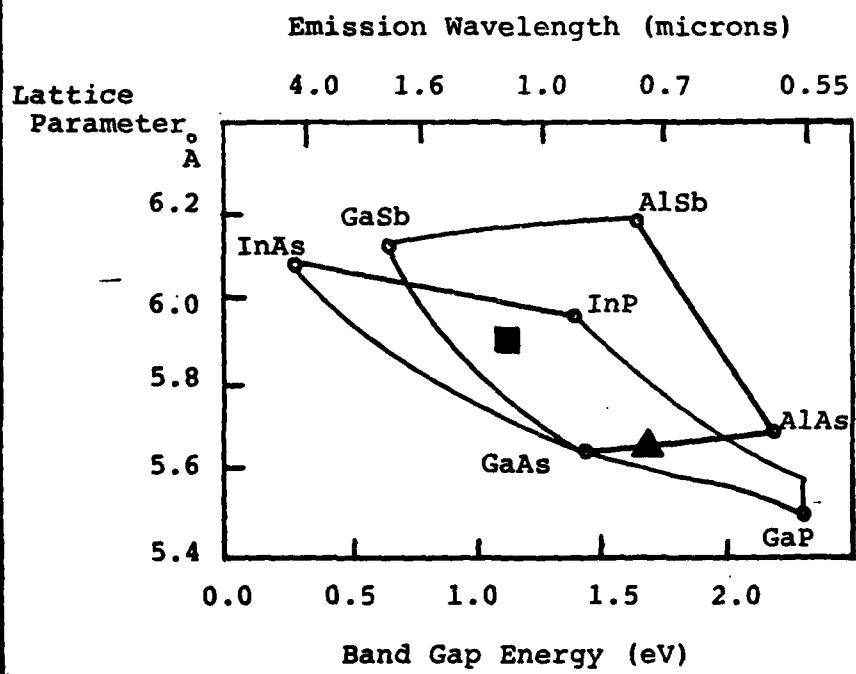
has made possible room temperature continuous wave operation (Ref 23). Much work has been done on these diodes and as a result this is the type found in most recent applications. The detailed operation of this structure is discussed in this paper. Some design parameters, reliability concerns, and applications, both realized and projected will also be covered.

Principle of Operation

A simple, double heterostructure laser is shown in cross section in Figure A.1a. Typical mole-fractions for the AlGaAs alloy are shown (Ref 24). The center region of thickness, d , is the recombination region, analogous to the gain medium. The relative amounts of Al and Ga in the crystal structure determine such important properties as emission wavelength and efficiency of the carrier injection (Ref 29). The interfaces above and below the active region are the heterojunctions. Upon forward bias, carriers are injected from both the p and n regions into the active layer where they radiatively recombine. The resulting optical radiation is then confined to the active region by the junctions. Laser oscillation occurs if at least two edges of the crystal block act as mirrors and form the resonant Fabry-Perot cavity. When the drive current exceeds a threshold (J_{th}), lasing action takes place and a beam is



(a) Cross section of Double Heterojunction Diode



(b) Characteristics of GaAs and InP Alloys

Figure A.1 (Ref 24)

emitted from each of the two facets. The frequency at which the light is emitted is predominately a function of the semiconductor (AlGaAs) and the mole-fractions. Figure A.1b depicts the band gap energy and associated wavelength, for various compounds of interest (Ref 24). It can be seen that wavelength and the lattice parameter can be varied independently to obtain desired operating and structural characteristics. The two most important classes of laser materials, the GaAs and InP are shown. The triangle depicts the compound represented in Figure A.1a. (i.e., Al_{.1}Ga_{.9}As). The associated wavelength is .82 microns. This particular alloy is of interest because its lattice parameter very nearly matches that of the GaAs substrate on which the diode is fabricated.

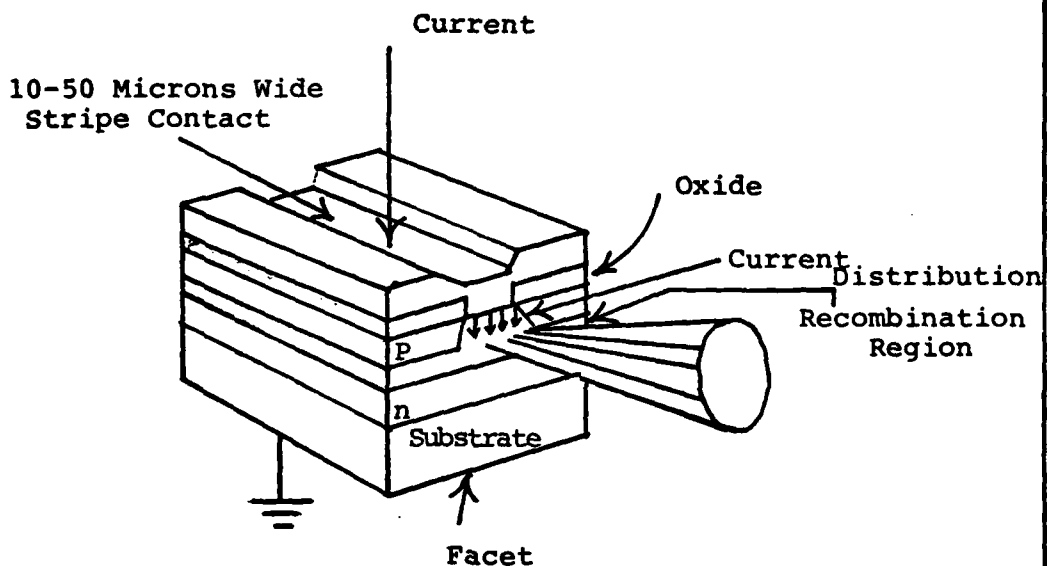
Of recent interest are compounds of In and P, a typical example of which is shown as the rectangle on Figure A.1b, (In_{.8}Ga_{.2}As_{.35}P_{.65}). This alloy emits at 1.1 micron, a wavelength which is important because losses in optic fibers are lower at this frequency.

The optical energy is confined by the mismatch of the indices of refraction of the materials. The active region has index N₁, while the regions on the other side of the junctions have index N₂, with N₂ < N₁. The relative magnitudes of N₁ and N₂ determine divergence properties of the emitted beam as well as efficiency of operation.

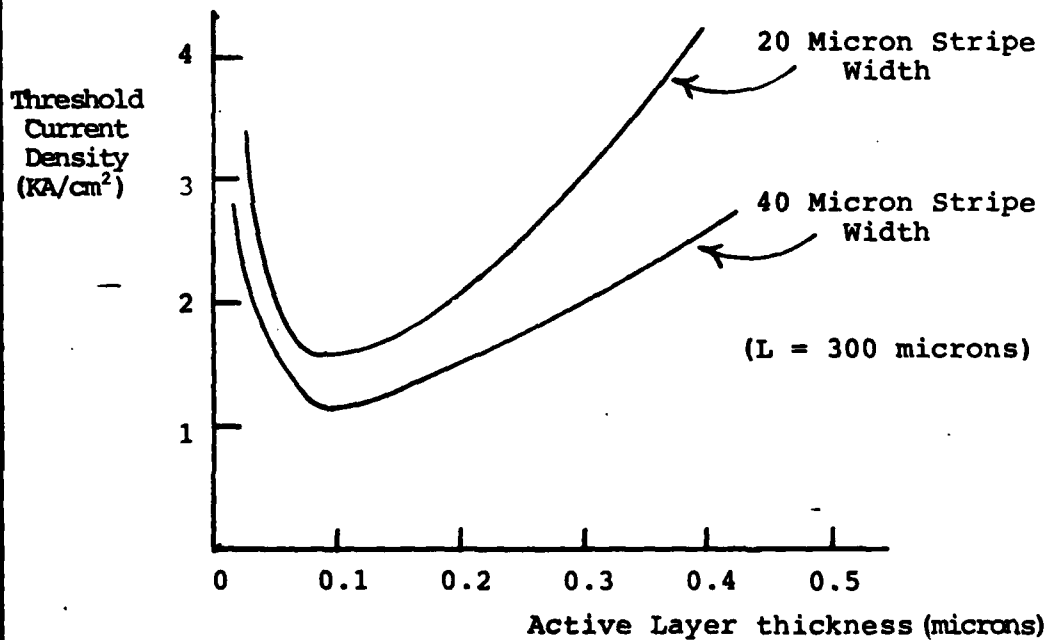
Longitudinal confinement and mode control is determined by the spacing of the mirror facets. Allowed modes are also a function of the average index of refraction. Lateral confinement is achieved for this particular structure by limiting the current density to a narrow region. A simple way to achieve this is through the use of a stripe contact on the P side of the diode. Figure A.2a, which is adapted from (Ref 24), shows the stripe contact. Typical stripe widths in use today are 10 microns and below. Parameters of interest to the applications engineer are discussed in the next section.

Device Parameters

Threshold Current. The minimum value of current at which lasing action will occur is a function primarily of the spacing (d) between the two junctions, as seen in Figure A.2b. There appears to be a particular value of d for which threshold current is a minimum. The thickness at which this minimum occurs is dependent on cavity length, facet reflectivities and the relative refractive index (Δn). Typical values of threshold current are 100 to 300 mA. Threshold current is also a strong function of temperature due to band gap shifts with resulting lower quantum efficiency.



(a) Stripe Contact Heterojunction Laser (Ref 28)



(b) Threshold Current Characteristic (Ref 8)

Figure A.2

Wavelength Considerations. Since the emitted frequency of radiation is dependent on band gap parameters, the output wavelength is also a strong function of temperature. The wavelength can vary as much as $4\text{\AA}/^\circ\text{K}$. Recent devices using distributed feedback and Bragg reflector gratings in the junction areas have shown much lower temperature dependence. Sensitivities as low as $.5\text{\AA}/^\circ\text{K}$ with narrow bandwidths ($< 10^\circ\text{A}$) have been reported (Ref 8).

Power Output. Typical emitted optical power from each facet of the laser is 10 to 20 mW for an input drive current of 80 to 150 mA (Ref 29). Output power is linear with current once threshold has been achieved. Several newer devices (Ref 8) have been reported which can emit these power levels at lower values of threshold. The Buried Heterostructure laser, which has an additional layer between the AlGaAs layers and the GaAs substrate, has achieved 20 mW per facet with a threshold of 20 to 40 mA. The Constricted DH laser, which obtains confinement with diffused regions in conjunction with the stripe contact, shows much promise as a high power CW device. Single-longitudinal mode CW operation has been reported up to 21 mW per facet. 50 mW per facet has been achieved in a pulse mode with a 50 percent duty cycle.

Beam Properties and Coupling to Fibers. The pattern emitted is usually elliptical with transverse and lateral beamwidths at half power of 40° and 10° . Because of the small spot size the beam is much more divergent than that of a conventional laser, a fact which can have an adverse effect when coupling into single mode fibers of low numerical aperture. The transverse (vertical) beamwidth is a function of the thickness (d) of the active region. Beamwidths of 15° to 25° have been obtained with very thin active regions ($400 - 600 \text{ \AA}$). In order to minimize power losses due to coupling of fibers, the fiber is typically butted right up to the mirror facet. Coupling losses using this technique are usually 50 percent (or 3 dB). Recent advances in the design of microlenses and techniques of fiber end preparation have reduced coupling losses to as low as 0.6 dB.

Reliability

The use of semiconductor lasers in optical communications depends on the availability of reliable devices. Much research has been done on failure mechanisms in AlGaAs diodes. The major problem areas are: bulk degradation, facet (mirror) damage, and metallization failure. Bulk degradation is a slow process which is only correctly characterized by long term tests at room temperature operation.

Recent results have shown laser operation approaching four years is possible. Facet damage can be eliminated by using coatings as long as power output is moderate. Recently, devices with Sb added to the active layer have had median lifetimes of 10^5 hours (Ref 2).

Applications

The use of semiconductor lasers has been closely tied to the optical communications field. For optical transmission systems to be practical, low power, cheap, and reliable sources of coherent light must be available. The development of laser diodes has thus gone along with breakthroughs in fiber optics. A significant demonstration of optic telecommunications occurred in Atlanta in 1976 (Ref 18). GaAs injection lasers were modulated with digital signals and coupled into two fiber cables each 658 meters long. AlGaAs Double-hetero-structure lasers radiating at .825 microns were used to couple more than 1 mW peak power into the fibers. The fibers were of multimode type with core diameters of 60 microns and 0.23 numerical aperture. An interesting feature of laser diodes is the availability of light output from both facets. In the Atlanta experiment, the back emission was monitored by a photodiode which then compensated the drive current of the laser for thermal stability.

Another proposed application in the field of integrated optics is the use of laser diodes in an optical spectrum analyzer (Ref 1). The use of heterostructure lasers with integrated waveguides, modulators, switches and detectors will be an important advancement in the instrumentation field.

For inertial instruments such as the Laser Gyroscope and the Sagnac Interferometer, the semiconductor laser has much potential. Its low power consumption and light weight make the laser diode well suited for aerospace applications. The implementation of a single axis rotation sensor on a single chip may even be possible.

Appendix B. Fiber Preparation and Handling

In order to achieve maximum coupling into the small ($10 \mu\text{m}$) core of the single mode fiber that is used, the fiber has to be prepared carefully. Fiber preparation consists of two distinct tasks, end preparation, or cleaving, and jacket removal. The removal of the plastic jacket is necessary to expose the glass cladding for mode stripping and to allow the fiber to fit into the holder. Achievement of a good end face cleave is essential for maximum light coupling.

A previous thesis (Ref 31) reported successful jacket removal using a scraping technique with a sharp scalpel blade. This technique works but the fiber can be broken too easily by accidental exertion of too much pressure. A better approach is to remove the jacket by immersion in concentrated sulfuric acid. A time of only 2 minutes is needed to completely remove the jacket.

Various means are used to obtain mirror flat end breaks. The scalpel blade is used to scribe a line on the fiber and then the fiber is broken by snapping it over the edge of a plate. The fiber can also be bent under tension around cylindrical surfaces and scribed (Ref 39). These techniques are difficult since the blade can only be used once or twice before it becomes too dull and

a satisfactory break is not achieved each time. The quickest results are obtained by simply breaking the fiber by bending over the edge of a plate and then viewing under the microscope. If a satisfactory break is obtained, the jacket is removed with the acid, and the end can be cleaned by wiping gently with a lens tissue soaked in acetone. Once prepared in this manner, extreme care must be exercised in placing the end of the fiber in the holder since even the slightest lateral pressure can result in a broken fiber.

Appendix C. Polarization Optics of Fibers

Birefringence

Birefringence is a property of crystals which is a measure of the difference between the phase velocities of different polarizations of light. In single mode optical fibers two orthogonal modes of propagation can exist. So, taking the state of polarization of the light into account, the single mode fiber is actually a two mode fiber. In a real fiber, coupling between these two modes can occur causing changes in path length and mode dispersion.

The birefringence can be written as (Ref 33)

$$k_B = k_x - k_y$$

where k_x and k_y are the propagation constants of the two orthogonally polarized modes. According to Yariv (Ref 50), the propagation constants can be written as

$$k_x = \omega\sqrt{\mu\epsilon_x}$$

$$k_y = \omega\sqrt{\mu\epsilon_y}$$

where μ is the magnetic permeability and ϵ_x and ϵ_y are the electric permeabilities in the x and y directions.

Depending on the magnitude of the birefringence, different effects on the state of polarization can occur. Simple pressure or deformations of the circular core can induce a linear birefringence where the polarization vector is only rotated as it evolves down the fiber. Twisting the fiber (Ref 46) can cause a circular birefringence. For the case of twisting three distinct situations can be discussed. The twist rate is defined as (T) and for weak twist, $|T| \ll |k_\beta|$, the linear birefringence is dominant. For medium twist, $|T| \approx |k_\beta|$ the strain induced in the fiber produces a circular birefringence (k_c) proportional to the twist $k_c = gT$ along with the linear birefringence. This results in elliptical birefringence which causes a complicated evolution of the polarization. At large values of the twist $|T| \gg |k_\beta|$ the situation is dominated by the circular birefringence.

Bending of the fiber also induces a birefringence (Ref 45). It is a stress effect as well and results from the lateral compressive stress that builds up in a bent fiber. The dominant stress component is σ_z where

$$\sigma_z = \kappa Ex$$

where $\kappa = 1/R_c$ and R_c is the radius of curvature of the bend, E is Young's modulus and x is a direction associated with the light polarization.

The dominant stress does not contribute directly to the birefringence, but a second order dependence of k_β on K has been observed and is given by

$$k_\beta = (-7.7 \times 10^7) \kappa^2 r^2 \quad (\text{deg/M})$$

where r is the radius of the fiber. This bending induced birefringence is used to overcome variations in polarization. A polarization holding fiber can be achieved by coiling a fiber under tension (Ref 34).

The birefringence can be measured in a number of ways. The most recent is the use of a polarimeter, which is an analyzer which is a device that measures the polarization vector (Ref 51). The direction of this vector defines the angles of the polarized modes, or eigenstates, and its magnitude is the degree of retardation where the fiber is modeled as a retardation plate (Ref 38). Variable azimuth, linearly polarized light, is input to a fiber and the output is analyzed by the polarimeter which is synchronized to the varying azimuth of the input. In this manner, the linear birefringence is measured directly.

The evolution of the polarization can be measured elasto-optically (Ref 11). The fiber is squeezed laterally with a periodic force. This force can be varied in azimuth (rotated around fiber). The polarization at the

output is thus modulated and its minimum amplitude occurs when the angle of the force is parallel or perpendicular to the unknown state of polarization in the fiber. Thus the evolution of the polarization vector can be determined at any point along the fiber.

The evolution of polarization is also measured using the Faraday effect in a magneto-optic set-up (Ref 38). The direction of the linear polarization is rotated by an applied magnetic field and the linear retardation measured. The Verdet constant, which is a measure of the amount of rotation of the polarization for a given magnetic field is found to be $\sim 1.5 \times 10^{-2} \text{ min A}^{-1}$ for the fiber tested.

Knowledge of the evolution of polarization can be used to design polarization controller devices, and this has been demonstrated (Ref 43). The most common technique to date is to employ electro-mechanical squeezing devices (Ref 19) which are driven by a feedback network which monitors the output state of polarization. An interesting possibility has been reported (Ref 44) where a multimode fiber can be used if polarizing elements are placed at each end, and spatial mode filters in the form of short single mode fibers are used. Each of these act to filter out a single arbitrary mode.

Appendix D. Acousto-Optic Efficiency

In the acousto-optic modulator, an input beam of light interacts with an acoustic pressure wave. For the case of light deflection, or frequency shifting, which is of interest here, the light must pass through the pressure wave at the Bragg angle (θ_B) given by

$$\sin\theta_B = \frac{\lambda}{2\Lambda}$$

for maximum deflection efficiency.

The maximum efficiency is a function of the material in the acousto-optic crystal and the power contained in the acoustic wave (Ref 16). The design of the acoustic transducer is also a key element. A parameter (Q) is usually defined (Ref 22)

$$Q = 2\pi \frac{\lambda w}{\Lambda^2}$$

where w = width of the transducer. The factors w and Λ determine the shape of the acoustic beam. Usually a condition for Bragg diffraction is stated as

$$Q \gg 1$$

The diffraction efficiency formula is presented in Chapter IV but is repeated here for reference.

$$E_{a/o} = \frac{I_{\text{diff}}}{I_{\text{incident}}} = \sin^2(1.4 \frac{0.6328}{\lambda} \ell \sqrt{M_w I_{\text{acoustic}}})$$

calculations for the laser and acoustic power used result in an expected efficiency of ~55%, while only 20-30% is observed.

It is known that the diffraction efficiency is also a function of the amount of optical and acoustic beam interaction, (Ref 10, 52). The above equation assumed the light was well collimated and the optic and acoustic beams interact 100%. But maximum efficiency will only be achieved if the beam spread ratio (R_{BS}) is greater than two, i.e.,

$$R_{BS} = \frac{\delta\theta_a}{\delta\theta_o} > 2$$

and $\delta\theta_a$ is the acoustic beam spread, and $\delta\theta_o$ is the optic beam spread. Ideally, the ratio of $\delta\theta_a$ to $\delta\theta_o$ should be large in order to obtain the maximum efficiency as determined by the material and the acoustic power.

θ_o can be measured experimentally. θ_a is determined by (Ref 10)

$$\delta\theta_a = \frac{\Lambda}{w}$$

Thus, if the width of the transducer and the material properties are known, the beam spread ratio can be determined.

A complete analysis of acoustic-light beam interactions has been presented by Klein and Cook (Ref 21). They describe the diffraction problem as a solution to a set of coupled difference-differential equations, and this formed the basis of most design calculations made to date.

Appendix E. Equipment and Experimental Set-Up

A total of six light sources were tested for their suitability for the incoherent gyro. Figure E.1 is a photograph of all devices characterized. Left to right they are: 1. visible plastic dome LED, 2. visible plastic fresnel lens LED, 3. visible point source LED, 4. IR plastic dome lens LED, 5. IR glass dome lens LED, injection laser diode on solder iron tip heat sink. The light sources were all mounted to an adapter plate which was part of an optic bench rail kit. A fixture was constructed from the kit which contained the necessary lenses and beamsplitters.

This fixture, along with the A/O and the fiber positioners, fiber coil, and detector electronics, was mounted on a 71 cm by 46 cm aluminum plate of thickness 2.6 cm. The plate was placed on a 5 cm thick piece of foam to minimize vibrations. Figure E.2 shows the components of the gyro mounted on the base.

Figure E.3 is a close-up of the laser mount with its 20X microscope objective. The protective cover has been removed for display. Figure E.4 is an overall view of the experimental apparatus showing the components mounted on the Genisco rate of turntable. Shown are the laser and detector power supplies, current monitor, and the rf drive equipment associated with the acousto-optic modulator.

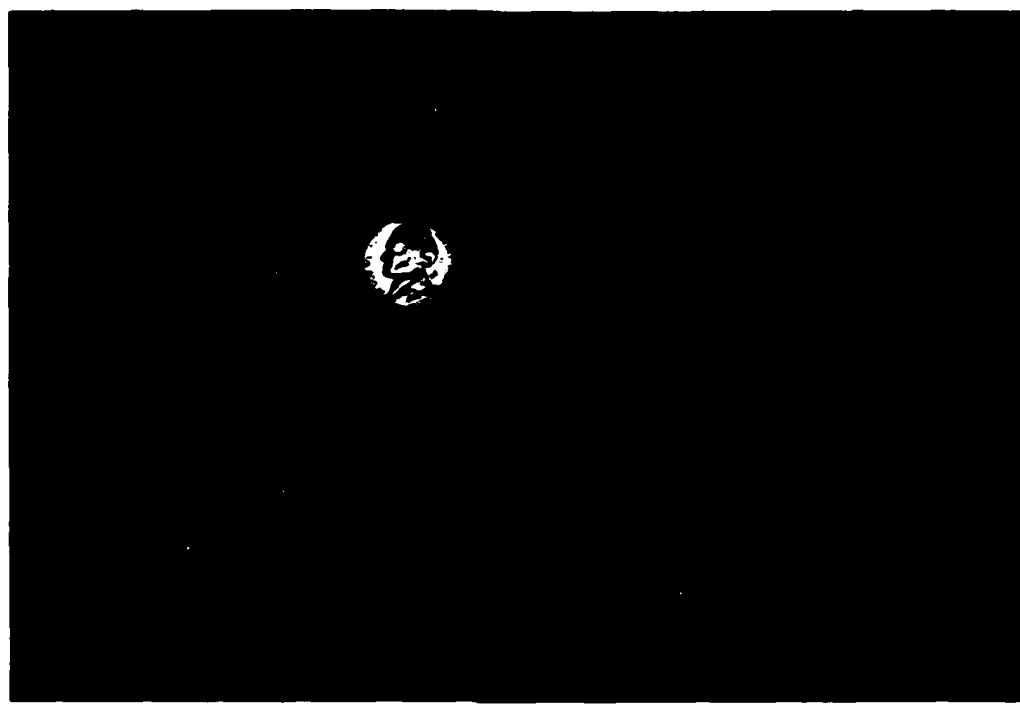


Figure E.1 Light Sources



Figure E.2 Gyro Components

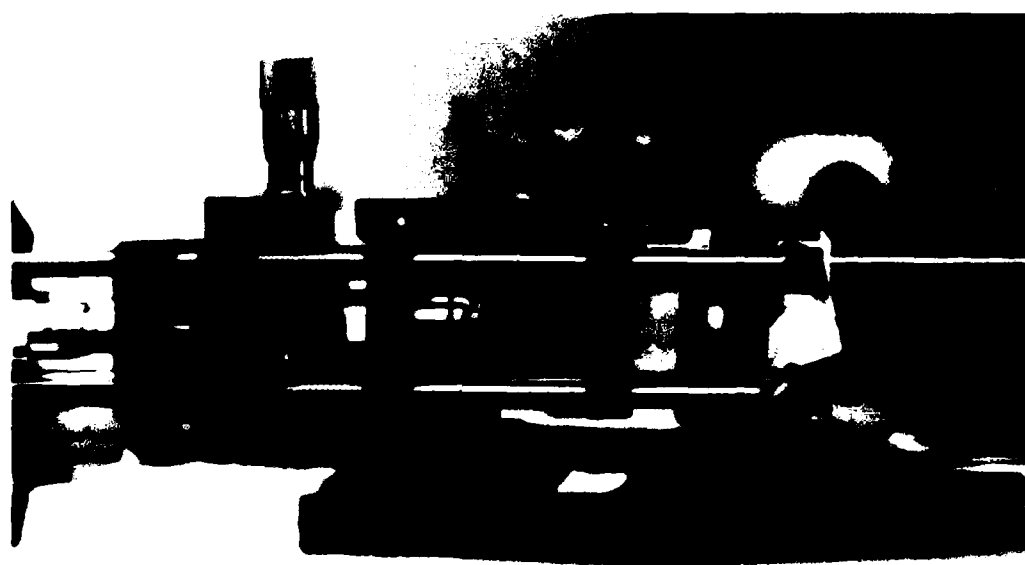


Figure E.3 Laser Diode Mount



Figure E.4 Experimental Set-up

Equipment Listing

LED, Red plastic dome	1
LED, Red fresnel lens	1
LED, Red point source	1
LED, IR XC-880A	1
LED, IR MFOE200	1
Injection Laser, LCW-10	1
Single mode fiber	1 coil
Multimode fiber	1 coil
20X Microscope objective	1
10X Microscope objective	2
Microscope mount	2
Cube beamsplitter	2
Fiber positioner NRC Model FP-1	2
Microbench rail system, Spindler and Hoyer	1 Kit
A/O modulator, Coherent Associates Model 305	1
Digital Voltmeter, Simpson 460	1
Power Supply, HP6236B	1
Power Supply, Powertec 6C3000	1
Signal Generator, AN/USM 323	1
Power Supply, Kepco Model SC32-1.5	1
Wideband RF power amplifier RF Power Labs Model M3058	1
Oscilloscope, Tektronix 565	1

Photodiode PIN 6D	1
Photodiode PIN 10D	1
Adjustable aperture	1
Neutral density filter	2 each
Lens F10, F50	1 each

Appendix F. Detectors

The PIN 6D and PIN 10D photodiodes in this experiment are of the photoconductive type and require a bias voltage for proper operation. Figure F.1 shows a schematic diagram of the amplifier circuit used. This circuit converts the current output of the photodiode to a voltage which is measurable by the oscilloscope. Biasing is provided by a 9V transistor battery.

The load resistor R_L converts the light induced current (i_s) into a voltage (e_o). This voltage is

$$e_o = i_s R_L$$

and

$$i_s = R_d I_L$$

where R_d is the responsitivity of the photodiode and I_L is the incident light in watts. From the detector specifications the minimum R_d is 0.333 amps/watts:

$$e_o = 0.333 I_L R_L$$

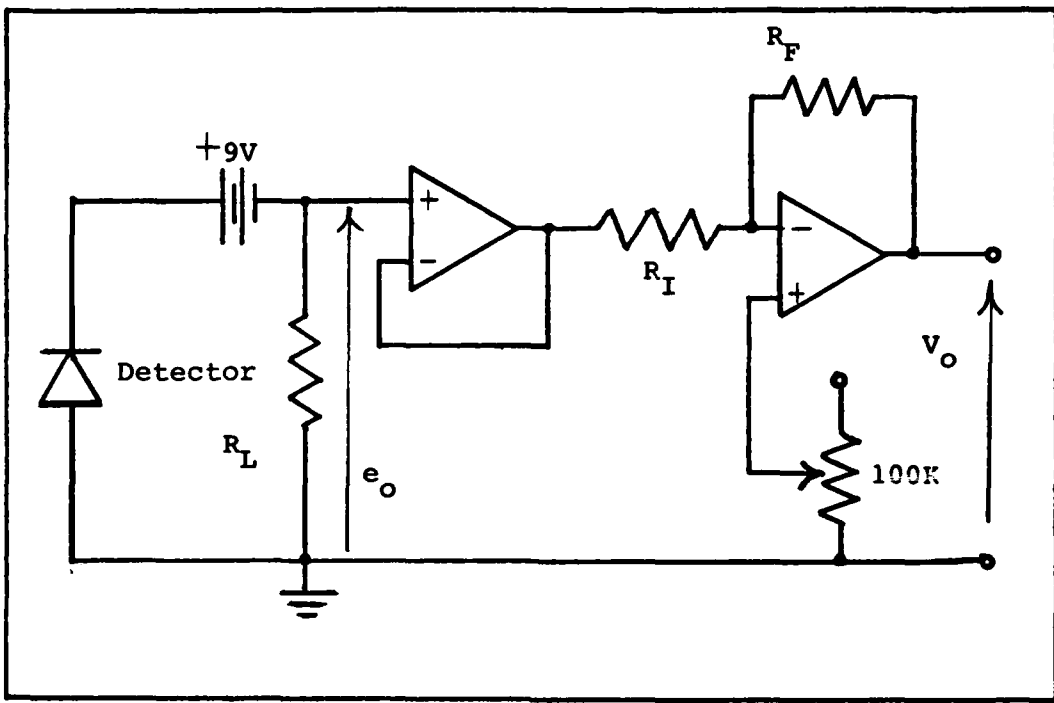


Figure F.1 Detector Amplifier

In this circuit, $R_L = 2K\Omega$, so

$$e_o = (0.333)(2K)I_L$$

The first amplifier is a 741 op amp in the unity gain mode for isolation, its output is e_o . The next 741 op amp is an inverting amplifier of gain $\frac{R_F}{R_I}$. The minimum gain value used was 100 or

$$\frac{R_F}{R_I} = \frac{200K\Omega}{2K\Omega} = 100$$

Thus, the output $V_o = 100(0.333)(2000)I_L$

or

$$I_L = \frac{(3.3)}{100(2000)} V_o = (16.5 \times 10^{-6})V_o$$

or

$$I_L = 16.5 V_o \text{ (microwatts)}$$

The feedback resistor, R_F , can be changed to increase the gain of the output amplifier, for measuring lower light intensities. Each time, the value of R_F is multiplied by 10 and the resulting scale factor is reduced. Table F.1 gives the values of resistors used and the associated gain and scale factor.

R_I	R_F	Output Gain	Scale Factor
2K	200K	100	16.5
2K	2M	1,000	1.65
2K	20M	10,000	.165

Table F.1 Detector Gain

The potentiometer in the non-inverting input of the output amp can be adjusted to null out any undesired bias voltage to yield a zero reading for zero light input.

Vita

Captain Richard L. Ice was born on 20 July 1951 in Atlanta, Georgia. He attended Georgia Institute of Technology for two years before enlisting in the Air Force in 1971. He was assigned to the 753rd Radar Squadron, Sault Ste. Marie, Michigan, where he was responsible for receiver systems maintenance on the AN/FDS-35 radar. He attended Auburn University from 1973 to 1976 as part of the Airman Education and Commissioning Program and was commissioned in September 1976.

Captain Ice was assigned to Ft. Meade, Maryland, from 1976 to 1980 where he worked as a circuit designer and program manager for Large Scale Integrated Circuit technology development. He was then assigned to the Air Force Institute of Technology (AFIT) to work towards a Master of Science degree in Electrical Engineering. He received his regular commission in July 1980 and graduated from AFIT in December 1981. He is currently assigned to the Air Force Electronic Warfare Center, Kelly AFB, Texas.

Captain Ice is married to the former Marian L. Ingram of Forest Park, Georgia. They have two children, Eric and Lauren.

~~UNCLASSIFIED~~

SECURITY CLASSIFICATION

Unclassified

SECURITY CLASSIFICATION OF THIS PAGE (When Data Entered)

REPORT DOCUMENTATION PAGE		READ INSTRUCTIONS BEFORE COMPLETING FORM
1. REPORT NUMBER AFIT/GE/EE/81D-29	2. GOVT ACCESSION NO. AD-A145 477	3. RECIPIENT'S CATALOG NUMBER
4. TITLE (and Subtitle) DESIGN CONSIDERATIONS FOR AN INCOHERENT FIBER OPTIC GYROSCOPE	5. TYPE OF REPORT & PERIOD COVERED	
7. AUTHOR(s) Richard L. Ice Captain USAF	6. PERFORMING ORG. REPORT NUMBER	
9. PERFORMING ORGANIZATION NAME AND ADDRESS Air Force Institute of Technology Wright-Patterson AFB, Ohio 45433	10. PROGRAM ELEMENT, PROJECT, TASK AREA & WORK UNIT NUMBERS	
11. CONTROLLING OFFICE NAME AND ADDRESS	12. REPORT DATE 18 December 1981	
14. MONITORING AGENCY NAME & ADDRESS (if different from Controlling Office)	13. NUMBER OF PAGES 131	
	15. SECURITY CLASS. (of this report) Unclassified	
	15a. DECLASSIFICATION/DOWNGRADING SCHEDULE	
16. DISTRIBUTION STATEMENT (of this Report) Approved for public release; distribution unlimited.		
17. DISTRIBUTION STATEMENT (of the abstract entered in Block 20, if different from Report) 15 APR 1982 Dean for Research and Professional Development Air Force Institute of Technology (ATC) Wright-Patterson AFB, OH 45433 <i>by S. W. [initials]</i>		
18. SUPPLEMENTARY NOTES Approved for public release; IAW AFR 190-17 Frederick C. Lynch, Major, USAF Director of Public Affairs		
19. KEY WORDS (Continue on reverse side if necessary and identify by block number) Fiber optic gyroscope, Injection laser diode, incoherent, Sagnac effect, Acousto-optic frequency modulation, random polarization.		
20. ABSTRACT (Continue on reverse side if necessary and identify by block number) The components required for the construction of an incoherent fiber optic gyroscope are tested. The instrument uses an incoherent light source such as an LED or diode laser operating below threshold. Five LED's and one laser diode were tested. An acousto-optic modulator is investigated as a signal processing element.		

UNCLASSIFIED

SECURITY CLASSIFICATION OF THIS PAGE(When Data Entered)

Equations are developed showing the effects of incoherence on the minimum expected rotation rate that can be observed. A review of optical rotation sensing in general, and the related technology is presented. The polarization properties of the source and fiber are discussed as they relate to gyro stability and minimum rotation rate.

Two possible signal processing techniques are presented which promise to further reduce minimum rotation rate and improve system stability.

The requirements on components for the fabrication of an inertial grade gyro are summarized along with a discussion of component contributions to gyro error.

UNCLASSIFIED

SECURITY CLASSIFICATION OF THIS PAGE(When Data Entered)

ATE
LME